Development of Coupled PROTEUS and SAM Code System for Multiphysics Analysis of Advanced Reactors

by

Gang Yang

A dissertation submitted in partial fulfillment
of the requirements for the degree of
Doctor of Philosophy
(Nuclear Engineering and Radiological Sciences)
in the University of Michigan
2022

Doctoral Committee:

Professor Won Sik Yang, Chair
Professor Krzysztof Fidkowski
Dr. Rui Hu, Argonne National Laboratory
Professor Xiaodong Sun

Gang Yang

ygang@umich.edu

ORCID iD: 0000-0002-6204-4987

© Gang Yang 2022

Dedication

To my family and friends.

Acknowledgements

First of all, I would like to express my sincere gratitude to my advisor Professor Won Sik Yang, for his patient guidance and kind support during my Ph.D. study. From him I learned not only academic knowledge but also how to think and solve problems. What he taught me through these years is a great treasure for my whole life. I would like to thank my committee members, Prof. Xiaodong Sun, Prof. Krzysztof Fidkowski, and Dr. Rui Hu for their valuable suggestions and insightful comments. I appreciate Dr. Acacia Brunett and Dr. Rui Hu for their guidance during my summer internship at Argonne National Laboratory (ANL). I would like to thank the Department of Energy (DOE) and ANL for funding this thesis research under DOE-NE Nuclear Energy Advanced Modeling and Simulation (NEAMS) program.

I would also like to thank my colleagues in Nuclear Reactor Design and Simulation Lab (NRDSL). We collaborate with each other on research and support each other in life. I will never forget the great time with Puran Deng, Albert Hsieh, Dr. Tian Jing, Dr. Ching-Sheng Lin, Dr. Byoung-Kyu Jeon, Dr. Guangchun Zhang, Dr. Hansol Park, and Dr. Yeon Sang Jung. Special thanks go to Dr. Mustafa Jaradat for his advice on this thesis work and companionship during all the hard times.

And thanks to my classmates at Xi'an Jiaotong University, Tianyuan Liu, Xukun He, Yikai Zeng, Lei Gao, Xinye Zhang, Jiangbo Dong, and Xia Yuan. It is their encouragement and support that give the strength to go further. I would like to thank all my friends at Purdue University and

the University of Michigan, specifically Yuting Wu, Zhixiong Zhang, and Yuan Zeng for supporting me during this COVID-19 pandemic. Thanks to Yatong An, Dongli Huang, Zhuoran Dang, Yeni Li, Jia Zhou, and Guanyi Wang for their help on coursework, qualifying exams, and everyday life.

Finally, I would like to express my deepest gratitude to my family for their endless love, understanding, and care. My mother devoted most of her time to raising and educating me since I was born. When I was a child, she planted a seed of pursuing higher education in my heart. Now that seed has grown into a tree. I wish I could pass that seed to more people one day.

Table of Contents

Dedication ii

Acknowledgements iii

List of Tables viii

List of Figures ix

Abstract xiii

Chapter 1 Introduction 1

1.1 Background 2

1.1.1 MSR Designs and Available Analysis Tools 2

1.1.2 Micro-reactor Designs and Available Analysis Tools 5

1.2 Motivation 9

1.3 Dissertation Layout 13

Chapter 2 Theory and Methodology 15

2.1 Multiphysics Problems of MSR and Micro-reactor 16

2.1.1 Multiphysics Problem of MSR 16

2.1.2 Multiphysics Problem of Micro-reactor 18

2.2 Methods for Solving the Coupled Multiphysics Problems 20

2.2.1 Operator-Splitting Method 20

2.2.2 Picard Iteration Method 21

2.2.3 Jacobian-Free Newton-Krylov Method 23

2.3 Summary 25

Chapter 3 Multiphysics Coupling of PROTEUS-NODAL and SAM for MSRs Applications 27

3.1 Coupling of PROTEUS-NODAL with 1-D SAM 27
3.1.1 PROTEUS-NODAL Wrapper TreeFrog 27
3.1.2 Overall Computational Procedure in TreeKangaroo 30
3.2 Coupling of PROTEUS-NODAL with Multi-D SAM 33
3.3 Summary 37
Chapter 4 Verification of Coupled PROTEUS-NODAL and SAM Code System 38
4.1 MSFR Benchmark Problem 38
4.2 Comparison to ANSYS CFX Results for Steady-State Problems 40
4.3 Verification Tests for Transient Problems 46
4.4 Summary 53
Chapter 5 Validation of Coupled PROTEUS-NODAL and SAM Code System with MSRE Experiments 54
5.1 Description of MSRE 54
5.2 Computational Models 58
5.3 Transient Analyses 66
5.3.1 Natural Circulation Test 69
5.4 Summary 71
Chapter 6 Multiphysics Coupling of PROTEUS-MOC and SAM for Micro-reactor Applications 72
6.1 Coupling of PROTEUS-MOC and SAM for Heat Pipe Cooled Micro-reactor Applications 72
6.2 Analysis of the HP-MR Problem with Coupled PROTEUS-MOC and SAM 79
6.2.1 Description of the HP-MR Problem 79
6.2.2 Analysis of the Unit-cell Problem of HP-MR 81
6.2.3 Analysis of the One-sixth Core Problem of HP-MR 96
6.3 Summary 107

Chapter 7 Summary and Future Work 109
7.1 Summary 110
7.2 Conclusion 112
7.3 Future Work 113
Bibliography 115

List of Tables

Table 4.1. Characteristics of Molten Salt Fast Reactor. 39

Table 4.2. Upper Energy Boundaries of 33-Group Structure. 41

Table 4.3. Upper Energy Boundaries of 9-Group Structure. 41

Table 4.4. Computational Times (s) for MSFR Verification Tests. 53

Table 5.1. Molar Composition of Fuel Salts. 55

Table 5.2. Main Characteristics of Molten Salt Reactor Experiment. 58

Table 5.3. Upper Energy Boundaries of 16-Group Structure. 59

Table 5.4 MSRE Heat Exchanger Parameters in SAM Model. 61

Table 5.5. Computational Times (s) for MSRE Validation Tests 67

Table 6.1. The main characteristics of HP-MR 81

Table 6.2. Comparison of eigenvalues for unit-cell problem. 84

Table 6.3. Comparison of isothermal temperature feedback coefficients (pcm/K) for unit-cell problem. 86

Table 6.4. Computational cost (CPU-hour) for the isothermal calculations of unit-cell problem. 88

Table 6.5. Eigenvalues and average temperatures for the multiphysics calculations of unit-cell problem. 89

Table 6.6. Comparison of eigenvalues from Serpent and PROTEUS-MOC for HP-MR problem. 99

List of Figures

Figure 1.1. Share of carbon-free electricity sources in several major economies and worldwide. (Data from International Energy Agency) [1] 1

Figure 1.2. Schematic diagram of the micro-reactor Concept developed at INL [33]. 6

Figure 1.3. Schematic diagram of the conventional heat pipe [34]. 7

Figure 2.1. Multiphysics and their interactions in the MSRs. 15

Figure 2.2. The operator-splitting method in coupled neutronics and thermal-hydraulics. 21

Figure 2.3. Picard iteration method in coupled neutronics and thermal-hydraulics. 23

Figure 3.1. MOOSE MultiApps system [25]. 28

Figure 3.2. Data flow between PROTEUS-NODAL and 1-D SAM under the MOOSE framework. 30

Figure 3.3. Coupling scheme with Picard iteration for steady-state calculations. 31

Figure 3.4. Coupling scheme with operator splitting for transient calculations. 32

Figure 3.5. Data flow and coupling scheme between PROTEUS-NODAL, Multi-D SAM, and 1-D SAM under the MOOSE framework. 34

Figure 3.6. Coupling scheme of PROTEUS-NODAL and Multi-D SAM for steady-state calculations. 35

Figure 3.7. Coupling scheme of PROTEUS-NODAL and Multi-D SAM for transient calculations. 36

Figure 4.1. Schematic representation of the Molten Salt Fast Reactor [8]. 39

Figure 4.2. Meshes utilized in Multi-D SAM (left) and CFX (right) calculations. 40

Figure 4.3. Planar (left) and axial (right) views of the MSFR model in R-Z geometry. 42

Figure 4.4. Axial velocity (left), radial velocity (middle), and temperature (right) fields of fuel salt obtained from CFX. The cylinder axis is on the left edge of the figures. 44

Figure 4.5. Axial velocity (left), radial velocity (middle), and temperature (right) fields of fuel salt obtained from Multi-D SAM. The cylinder axis is on the left edge of the figures. 44

Figure 4.6. Comparison of axial velocity profiles of Multi-D SAM and CFX. 45

Figure 4.7. Comparison of axial velocity profiles of 1-D SAM and CFX. 45

Figure 4.8. Relative deviation (%) in power density of coupled calculation with Multi-D SAM (left) and 1-D SAM (right) from that with CFX. 46

Figure 4.9. 1-D SAM model of MSFR benchmark problem. 47

Figure 4.10. Multi-D SAM model of MSFR benchmark problem. 48

Figure 4.11. Power evolution during UTOP transient. 49

Figure 4.12. Power evolution during ULOF transient. 50

Figure 4.13. Average inlet velocity evolution during ULOF. 51

Figure 4.14. Power evolution during ULOHS. 52

Figure 5.1. Schematic diagram of MSRE reactor vessel [7]. 55

Figure 5.2 Layout of MSRE primary and secondary systems [7]. 56

Figure 5.3. Radial layout of MSRE core (left) and lattice arrangement of fuel channel (right)... 57

Figure 5.4. Lattice arrangement of control rods (up) geometry and composition of the control rod element (bottom) (units in inch) [78]. 57

Figure 5.5 Radial (left) and axial (right) configurations of cross section tally regions [80]. 59

Figure 5.6. PROTEUS-NODAL models of MSRE core in R-θ-Z geometries. 60

Figure 5.7. Primary Loop Model developed for MSRE using SAM. 62

Figure 5.8. Mesh utilized in CFX calculation for fuel channel of MSRE. 64

Figure 5.9. Axial variation of Nusselt number in MSRE fuel channel obtained from CFX. 64

Figure 5.10. Axial temperature distributions of fuel salt in the hottest channel of MSRE. 65

Figure 5.11. Axial temperature distributions of moderator in the hottest channel of MSRE. 66

Figure 5.12. Pump speed and secondary flow rate during start-up test [86]. 67

Figure 5.13. Pump head during protected pump start-up and coast-down transients. 68

Figure 5.14. Compensated reactivity during protected pump start-up and coast-down transients. 69

Figure 5.15. Recorded power and average inlet and outlet temperatures during natural circulation test. 70

Figure 5.16. Comparison of power evolution during natural circulation test. 71

Figure 6.1. Coupling Scheme between PROTEUS-MOC and SAM..... 76

Figure 6.2. Schematic plot of 2D-RZ heat pipe model. 77

Figure 6.3. Schematic plot of 3D-1D heat pipe model [61]..... 77

Figure 6.4. Coupling scheme of PROTEUS-MOC and SAM for steady-state calculations..... 78

Figure 6.5. Coupling scheme of PROTEUS-MOC and SAM for transient calculations..... 79

Figure 6.6. Radial (left) and axial (right) configurations of the HP-MR problem..... 80

Figure 6.7. Radial layout of the fuel assembly of the HP-MR problem. 80

Figure 6.8. Radial (left) and axial (right) configurations of the unit-cell problem. 82

Figure 6.9. Mesh for PROTEUS-MOC (left) and 3D heat conduction calculation of SAM (right). 83

Figure 6.10. Axial power distributions for the unit-cell isothermal calculations at 800 K..... 87

Figure 6.11. Power (W/m^3) and temperature (K) distributions of the unit-cell problem from the coupled PROTEUS-MOC and SAM calculation..... 90

Figure 6.12. Power (W/m^3) and temperature (K) distributions of the unit-cell problem from the coupled Griffin/BISON/Sockeye calculation. 91

Figure 6.13. Axial temperature distributions from the coupled PROTEUS-MOC/SAM and Griffin/BISON/Sockeye calculations..... 91

Figure 6.14. Axial temperature distribution at the wick-vapor interface for the coupled calculations of unit-cell problem. 92

Figure 6.15. Power evolutions for the coupled calculations during the load following power transient..... 92

Figure 6.16. Average fuel pin temperature evolutions for the coupled calculations of the load following power transient. 93

Figure 6.17. Component-wise reactivity evolutions of the coupled PROTEUS and SAM calculation during the load following power transient. 93

Figure 6.18. Power evolutions for the coupled calculations without heat pipe feedback during the load following power transient. 95

Figure 6.19. Average fuel pin temperature evolutions for the coupled calculations without heat pipe feedback during the load following power transient. 95

Figure 6.20. Component-wise reactivity evolutions of the coupled PROTEUS and SAM calculation without heat pipe feedback during the load following power transient. 96

Figure 6.21. The fuel (a), control drum (b), and reflector (c) mesh generated by mesh toolkit. .. 97

Figure 6.22. Generated mesh for 1/6 of the HP-MR problem in PROTEUS-MOC. 97

Figure 6.23. Generated mesh for 1/6 of the HP-MR problem in SAM. 98

Figure 6.24. Axial distributions of power in different pins at 900 K. 100

Figure 6.25. Radial distributions of power density (W/m^3) from PROTEUS isothermal calculation in the plane at 0.25 m. 100

Figure 6.26. Radial distributions of power density (W/m^3) from coupled PROTEUS isothermal calculation in the plane at 1.00 m. 101

Figure 6.27. Temperature distribution from coupled calculations. 102

Figure 6.28. Temperature distribution at the middle plane from coupled calculations. 102

Figure 6.29. Axial distributions of power in different pins from coupled calculations. 103

Figure 6.30. Power (left) and fuel temperature (right) evolutions for the coupled calculations of the load following power transient. 104

Figure 6.31. Power distributions of the middle plane at 0 s (a), 100 s (b), 400 s (c), and 800 s (d) for the coupled calculations of the load following power transient. 105

Figure 6.32. Temperature distributions of the middle plane at 0 s (a), 100 s (b), 400 s (c), and 800 s (d) for the coupled calculations of the load following power transient. 106

Abstract

In order to meet the growing worldwide electricity demand while reducing the environmental impacts from CO_2-emission energy sources, the next-generation nuclear reactor systems are being developed under the goals of sustainability, safety, reliability, economic competitiveness, proliferation resistance, and physical protection. The molten salt reactor (MSR) with liquid fuel is one of these reactors, which is receiving growing interest from the industry worldwide. Various micro-reactor concepts are also being developed to enable flexible siting to support applications for remote areas and integration into micro-grids in populated areas and to provide resilient power for emergency operations related to natural disasters.

The design and safety analyses of these advanced nuclear reactors require multiphysics simulations. In particular, the liquid fuel of MSRs results in a strong coupling of neutronics and thermal-hydraulics. The core reactivity is directly correlated with the velocity of flowing fuel because of the precursor decay outside the core and the large negative reactivity due to the thermal expansion of liquid fuel. Meanwhile, diverse micro-reactor designs in irregular geometries with non-conventional heat removal systems such as heat pipes make the conventional analysis tools based on the diffusion theory inadequate. Therefore, this work aimed to develop coupled neutronics and thermal-hydraulics multiphysics analysis capabilities for advanced reactors, focusing on MSRs and micro-reactors, using the neutronics code PROTEUS and the system analysis code SAM of the U.S. DOE's Nuclear Energy Advanced Modeling and Simulation (NEAMS) program.

For accurate and efficient simulation of the steady-state and transient behaviors of MSRs, the nodal solver of PROTEUS (PROTEUS-NODAL) has been coupled with SAM under the MOOSE framework. The coupling was made by developing a MOOSE wrapper of PROTEUS-NODAL and a master application that controls PROTEUS-NODAL neutronics and SAM thermal-fluidic calculations. The coupled code system was verified and validated with the Molten Salt Fast Reactor (MSFR) benchmark problem and the available experimental data of the Molten Salt Reactor Experiment (MSRE). The solutions for the MSFR problem agreed well with the open literature results. The validation test results for the pump start-up, pump coast-down, and natural circulation tests of MSRE agreed well with the measured values. These results indicate the reliability of the coupled code system of PROTEUS-NODAL and SAM for steady-state and transient analyses of MSRs.

To model diverse micro-reactor designs of irregular geometries, the MOC transport solver of PROTEUS (PROTEUS-MOC), which can solve 3-D heterogeneous problems with complicated geometries, has been coupled with SAM under the MOOSE framework. A MOOSE wrapper of PROTEUS-MOC was developed as the master application to control the simulation process with the sub-application SAM. A unit-cell and one-sixth core problems of a heat-pipe cooled micro-reactor design (HP-MR) were analyzed with the coupled code system to demonstrate the developed capabilities. The results confirm the applicability of the coupled PROTEUS-MOC and SAM code system to steady state and transient analyses of micro-reactors.

Chapter 1 Introduction

Nuclear energy plays an important role in power generation, which is the largest low-carbon energy source in US electricity production and the second largest low-carbon energy source globally, as shown in Fig. 1.1 [1]. In order to meet the growing worldwide electricity demand while reducing the environmental impacts from the utilization of CO_2-emission energy sources, the next-generation nuclear reactor systems are being developed under the goals of sustainability, safety, reliability, economic competitiveness, proliferation resistance, and physical protection [2]. The molten salt reactor (MSR) with liquid fuel is one of these reactors, which is receiving growing interest from the industry worldwide. Various micro-reactor concepts are also being developed to enable flexible siting that can support applications for remote areas and integration into micro-grids in populated areas to provide resilient power for emergency operations related to natural disasters.

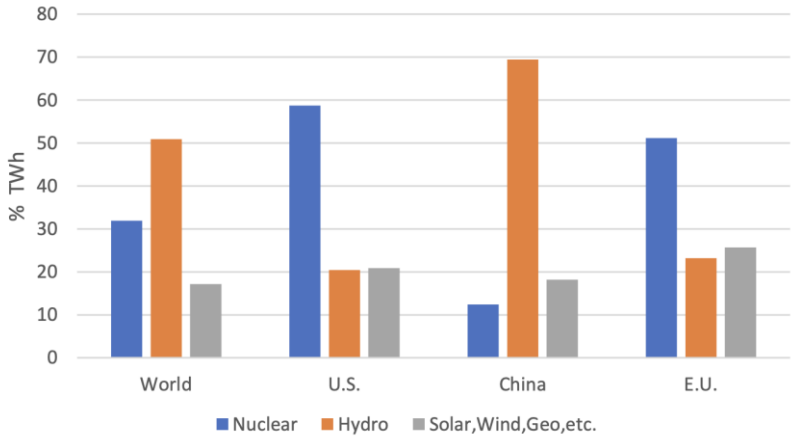


Figure 1.1. Share of carbon-free electricity sources in several major economies and worldwide. (Data from International Energy Agency) [1]

The design and safety analyses of these advanced nuclear reactors require multiphysics simulations. Meanwhile, diverse micro-reactor designs of irregular geometries with non-conventional heat removal systems such as heat pipes make the application of conventional analysis tools based on the diffusion theory inadequate. Therefore, this work aimed to develop a coupled neutronics and thermal-hydraulics code system for multi-physics analysis of advanced reactors, focusing on MSRs and micro-reactors, using the neutronics code PROTEUS [3] and the system analysis code SAM [4] of the U.S. DOE's Nuclear Energy Advanced Modeling and Simulation (NEAMS) program.

In this chapter, the historical review of various MSR and micro-reactor concepts and analysis tools are provided first. Then the motivation for this thesis is presented. The last part gives the overall structure of this thesis and a brief introduction to each chapter.

1.1 Background

1.1.1 MSR Designs and Available Analysis Tools

In the MSRs with flowing fuel, the fuel is dissolved in the molten salt and flows through the core and the intermediary heat exchanger. Compared to solid fuel reactors, liquid fuel MSRs have several advantages including a large negative temperature coefficient of reactivity due to the high thermal expansion coefficient of fuel, possible continuous fission product removal, and better resource utilization by achieving higher fuel burnup [2]. Furthermore, MSRs are operated at low pressure and the fuel in the core can be drained to a decay tank if the fuel temperature reaches a specific limit, making the MSR a potentially safer system.

The concept of MSR with liquid fuel was first proposed by Oak Ridge National Laboratory (ORNL) in the late 1940s. In the 1950s, the Aircraft Reactor Experiment (ARE) was built to demonstrate the MSR concept [5]. After that, a graphite-moderated Molten Salt Reactor

Experiment (MSRE) was designed, built, and operated by ORNL in the 1960s [6] as a test reactor to demonstrate the feasibility of the MSR concept. Based on MSRE, the Molten Salt Breeder Reactor (MSBR) was designed at ORNL but suspended before being built [7]. After the 2000s, there were renewed interests in MSRs worldwide. A fast spectrum MSR design named Molten Salt Fast Reactor (MSFR) was developed in Europe under the EURATOM EVOL (Evaluation and Viability of Liquid Fuel Fast Reactor Systems) Project [8], which utilizes the thorium fuel cycle with mixed lithium fluoride and actinide fluoride salt. A small modular Integral Molten Salt Reactor (IMSR) was designed by the Canadian company Terrestrial Energy [9]. IMSR was based on MSRE with a reconfiguration and scale-up. It utilizes a once-through uranium fuel cycle as the simplest option and the fuel is dissolved in fluoride salt. During the operation lifetime, there is no need to open the reactor vessel. The whole unit inside the vessel will be replaced after around seven years of operation. In the U.S., TerraPower's Molten Chloride Faster Reactor (MCFR) design [10] has received a funding award from the U.S. DOE. The MCFR design utilizes a fast spectrum and a continuous fueling process.

The growing interest in MSRs from the industry has encouraged the development of new coupled code systems for the simulation of MSRs with flowing fuel worldwide. At the Politecnico di Milano (Polimi) and the Technical University of Delft (TUDelft), two coupled neutronics and thermal-hydraulics analyses were performed for the MSFR design [11]. In the Polimi model, the coupled thermal-hydraulic equations, multigroup neutron diffusion equations, and delayed neutron precursor equations were solved by the commercial software COMSOL Multiphysics [12]. The TUDelft model was based on the coupling of neutron transport code DALTON [13] and finite-volume computational fluid dynamics (CFD) code HEAT [14]. At the Paul Scherrer Institute (PSI),

a coupled tool consisting of thermal-hydraulics system code TRACE [15] and three-dimensional neutron diffusion solver PARCS [16] was developed [17].

A coupled transient analysis model for MSFR was developed [18] based on the open-source CFD library OpenFOAM [19]. In this work, one group diffusion approximation was used for the neutronics calculation and the Reynolds-Averaged Navier–Stokes (RANS) equations were solved for the single-phase fluid. Another coupled neutronics and thermal-hydraulics code TANSY was developed based on OpenFOAM for MSR simulations [20], where the multigroup neutron diffusion and fluid equations are discretized with the finite volume method and solved iteratively. Meanwhile, a general multi-physics simulation tool for nuclear reactors named "GeN-Foam" [21, 22] was developed at the EPFL and PSI based on OpenFOAM. For neutronics calculation, multi-group diffusion, SP_3, and S_n solvers were implemented in GeN-Foam. GeN-Foam has been applied to simulate several types of advanced reactors, including MSRs. To study the fuel compressibility effects in the MSFR, a multiphysics code was developed based on the two-phase Euler-Euler model in OpenFOAM [23]. It was found that the incompressible approximation would lead to an underestimation of the power in super-prompt critical reactivity insertion.

An open-source MSR simulation tool Moltres [24], was developed in the context of the Multiphysics Object-Oriented Simulation Environment (MOOSE) finite element framework [25]. In Moltres, neutron diffusion, delayed neutron precursor, and thermal-fluidic equations are solved simultaneously. Moltres was utilized to study the steady-state and transient behavior of MSFR [26]. Recently, multiphysics simulation capabilities for MSRs were added to the Virtual Environment for Reactor Applications (VERA) [27]. A generic species transport capability and a two-phase gas sparging modeling were implemented in the subchannel thermal-hydraulics analysis

code CTF [28]. The coupling scheme in VERA between the neutron transport code MPACT [29, 30] and CTF was modified for MSR simulations.

1.1.2 Micro-reactor Designs and Available Analysis Tools

While there is no clear definition of the micro-reactor, it is usually referred to reactors that produce thermal energy less than 20 MW and show the following three features [31]: (1) They are factory-fabricated and assembled, (2) They are transportable and can be easily shipped to the destination by the trunk, shipping vessel, or railcar, and (3) They are self-adjusting and required a small number of operators due to the utilized passive safety systems. Because of these features, micro-reactors are desirable for producing power for remote areas or the areas affected by natural disasters. During power outages, critical facilities connected to the grid, such as hospitals and water treatment plants, can continue to operate if powered by micro-reactors in microgrids [32]. Because the micro-reactor designs usually have a longer core lifetime without refueling for up to 10 years, it has an advantage over diesel generators for industrial facilities in remote areas. The US advanced reactor industry has proposed several different micro-reactor designs and a demonstration of micro-reactor is expected to be built in 2025. Figure 1.2 shows a demonstration of the micro-reactor being developed at Idaho National Laboratory (INL).

One of the typical micro-reactor designs uses heat pipes to remove the heat from the core. Heat pipe employs working fluid phase change to transfer heat from the evaporator surface to the condenser surface. The configuration of a conventional heat pipe is shown in Fig 1.3 [34]. Usually heat pipe consists of an envelope, a wick structure, and a working fluid. In the evaporator section of the heat pipe, the liquid working fluid absorbs the external heat from the surface and turns into

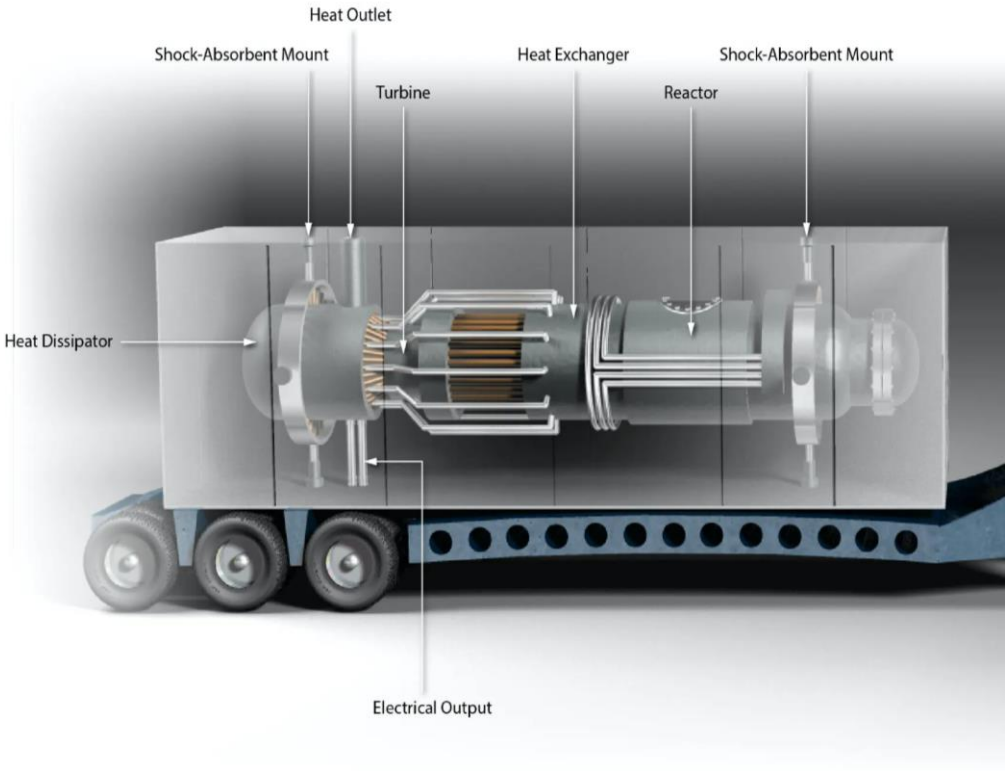


Figure 1.2. Schematic diagram of the micro-reactor Concept developed at INL [33].

vapor. The vapor migrates through the adiabatic section to the cold condenser section, where the vapor condenses back into the liquid and releases the latent heat to the heat sink. Finally, the liquid returns to the evaporator section through capillary force in the wick. Due to the high heat transfer coefficient of boiling and condensation of the working fluid, the heat is transferred from the evaporator region to the condenser section. Another advantage of the heat pipe is that there are no mechanical moving parts or external pumps, which makes it more reliable. The advantage of using a heat pipe cooled design over other conventional cooling methods include exceptional flexibility, simple construction, easy maintenance, and easy control with no external pumping power [35].

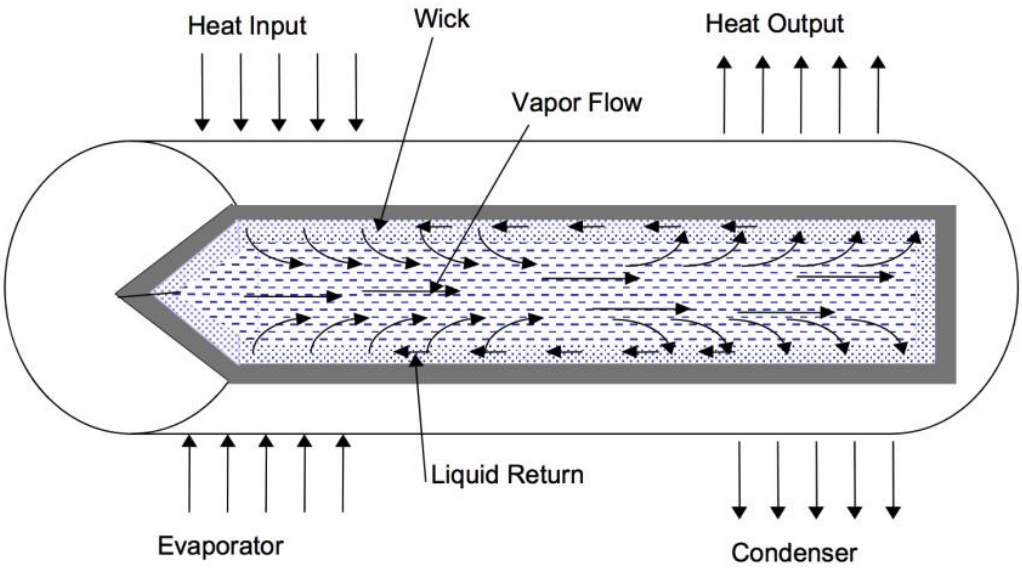


Figure 1.3. Schematic diagram of the conventional heat pipe [34].

In 2015, the Kilopower project was initiated by NASA to demonstrate the small space fission power for space science and human exploration power need [36]. The Kilopower reactors were designed to produce power of 1 to 10 kW using Stirling converters with sodium heat pipes. It is a fully automated nuclear reactor designed to operate continuously for decades on deep-space craft, on the moon, or on Mars. A prototype test facility Kilopower Reactor Using Stirling Technology (KRUSTY), was built and tested during the period of 2015 to 2018. In the KRUSTY experiment, the core was fueled with highly enriched uranium (HEU) to generate 1 kW of electric power. The core was cooled using 230 heat pipes and the electrical power was generated using eight Stirling engines. Several transient experiments were performed to demonstrate the self-regulating characteristics of the Kilopower reactor, including failure of Stirling engines, increasing the stroke on Stirling engines, adjusting the reactivity to increase the peak core temperature, and

turning off all heat removal systems except the radiative heat transfer to the vacuum chamber [36]. The KRUSTY experiments demonstrated the feasibility of the Kilopower design.

The MegaPower reactor [37] is a 5 MWth heat pipe cooled fast spectrum micro-reactor concept designed by Los Alamos National Laboratory (LANL), a scale-up of the Kilopower reactor. The MegaPower uses 19.75 wt. % enriched UO_2 as fuel and B_4C for neutron absorbers. There is a hexagonal volume for two emergency shutdown control rods in the core. The material of the monolith and the side reflector is SS316 and alumina (Al_2O_3), respectively. There are 1224 potassium heat pipes in the core. Because of the large number of heat pipes in the core, it provides redundancy for single heat pipe failure and eliminates the loss-of-forced-cooling severe accident scenarios [38].

Leveraging on the LANL heat pipe technology and MegaPower experience, Westinghouse and LANL are developing the eVinci™ micro-reactor [39], which can generate power from 200 kW to 5 MW. Same as the MegaPower, the B_4C control drum is used for reactivity control. High-Assay Low-Enriched Uranium (HALEU) TRISO (TRi-structural ISOtropic) fuel will be utilized for safety concerns. It is planned to perform a system integral test with nuclear fuel and to demonstrate for commercial deployment in a few years.

The multiphysics coupled code system of PROTEUS/FLUENT/ANLHTP was developed by ANL for the analyses of heat pipe cooled micro-reactor [40]. The coupling of the three codes is controlled by a Python-based driver. PROTEUS [41] was used as the neutronics analysis code. FLUENT [42] was utilized for thermal conduction analysis and ANLHTP [43] was a one-dimensional heat pipe analysis code developed at ANL. The data transfers among the three codes were performed through the driver. The coupled system was qualitatively verified with a 3D unit

assembly problem. Both steady and transient results of the coupled simulations showed reasonable power and temperature distributions.

To support the design and safety analysis of the heat pipe cooled nuclear micro-reactors, DireWolf [44] was developed based on the MOOSE framework under the NEAMS program. DireWolf serves as the driver for the coupled simulation, which utilizes different codes to solve different physics. Griffin [45] is utilized as the neutronics solver within DireWolf. Sockeye [46] is adopted as the heat pipe analysis code, which supports two types of heat pipe model: a one-dimensional, two-phase flow model and a two-dimensional simplified heat conduction model. Bison [47] solves the whole core thermo-mechanics. In the coupled steady state calculation, "pseudo transient" is used to avoid numerical instability, where the transient equations are solved until the steady state is reached.

In addition, the neutronics codes based on the Monte Carlo method were widely utilized in the multiphysics simulation of micro-reactors due to their flexibility in geometrical modeling. A three-dimensional high-fidelity neutronics-thermo-elasticity multiphysics coupling code based on the Monte Carlo transport code OpenMC [48], finite element code Nektar++ [49] and SfePy [50] was developed for steady state and depletion calculations of micro-reactors [51]. The functional expansion tally method was implemented to perform data mapping between OpenMC and Nektar++. The KRUSTY test facility was analyzed with the coupled OpenMC, Nektar++, and SfePy code system.

1.2 Motivation

Multiphysics simulation capabilities are required in the design and safety analyses of MSRs and micro-reactors. In particular, the liquid fuel of MSR results in a strong coupling of neutronics and thermal-hydraulics. The core reactivity is directly correlated with the speed of flowing fuel

because of the precursor decay outside the core and the large negative reactivity due to the thermal expansion of liquid fuel. Additionally, transient multiphysics simulation capabilities are needed to confirm the self-adjusting characters of micro-reactors.

As mentioned in the previous section, there are several multiphysics simulation tools developed for MSRs. However, most of the available simulation tools for MSRs have limitations on applicability. In the coupled TRACE and PARCS code, cylindrical geometry is not supported in PARCS. As a result, cylindrical cores of molten salt fast reactors had to be approximated by hexagonal or Cartesian geometry models. This approximation would affect the neutron leakage of the core and subsequently introduce errors in the eigenvalue [52]. In contrast, the high-fidelity simulation tools, such as finite volume method (FVM) based code GeN-Foam and finite element method (FEM) based code Moltres, have flexible geometric modeling capability. However, high-fidelity simulations increase the computational cost significantly. The coupled CFD and neutron transport codes based on FVM or FEM for the whole core simulation of MSRs usually require to be executed parallel on computer clusters with a large number of processors. Moreover, modeling system components in the primary and secondary loops, such as the heat exchangers, pumps, and pipes, would require additional effort in high-fidelity simulations. Because of these drawbacks, the high-fidelity simulation tools cannot currently be widely applied in the design and safety analyses of MSRs.

Since the micro-reactor designs vary in power, neutron spectrum, and fuel type and can be in irregular geometries, the conventional analysis tools based on the diffusion theory are inadequate to simulate the micro-reactors. High-fidelity multiphysics simulation codes are being developed based on the transport theory. However, most of these codes cannot be applied to the whole core transient calculations currently. Due to the lack of acceleration schemes, the Griffin S_n

transport solver requires a high computational cost, which makes it cannot be applied to the whole core multiphysics simulation of micro-reactors [53]. Instead, the Griffin diffusion calculation with super-homogenization (SPH) factor is applied in the multiphysics simulations. Nevertheless, generating the SPH factors for complex geometry requires significant effort. Similarly, the multiphysics simulation tools with Monte Carlo transport calculations cannot be applied to the transient whole core analyses of micro-reactors due to computational inefficiency.

Motivated by the need for a fast-running and accurate multiphysics simulation tool for the design and analyses of MSRs and a neutron transport based multiphysics tool with transient simulation capability for micro-reactors, it is aimed to develop a coupled neutronics and thermal-hydraulics multiphysics analysis capabilities for MSRs and micro-reactors in this work, using the neutronics code PROTEUS and the system analysis code SAM. The PROTEUS was selected as the neutronics solver, which included a nodal solver (PROTEUS-NODAL) [54, 55] and a MOC solver (PROTEUS-MOC). PROTEUS-NODAL is a three-dimensional (3D) neutronics code based on the homogeneous assembly model. It was extended to model the drift of delayed neutron precursors in MSRs [56] by solving the delayed neutron precursor equations that include a convection term with the neutron flux equations. In addition, to model the cylindrical cores more accurately, the variational nodal P_1 solver for cylindrical geometries (R-Z and R-θ-Z) was developed [57]. PROTEUS-NODAL can be utilized for both steady state and transient neutronics modeling of the MSR accurately and efficiently.

PROTEUS-MOC combines the unstructured finite element based MOC method for the radial plane with the discontinuous Galerkin finite element method in the axial direction to efficiently solve axially extruded 3-D problems. Due to the use of unstructured finite element mesh, it can handle 3-D heterogeneous problems with complicated geometries, including the

internal void region and rotating control drum in micro-reactors. It is accelerated with the unstructured CMFD (uCMFD) [58] and quasi-static methods [59] and thus it can be applied to the transient multiphysics simulation of micro-reactors.

SAM [4] was selected as the thermal-hydraulics solver, which is a modern system analysis code being developed at Argonne National Laboratory. SAM has a fast-running and whole-plant transient analyses capability with improved fidelity for advanced reactors. A set of system components, such as heat exchangers, pumps, and pipes, have been implemented as the built-in components in SAM for friendly user interactions [4]. It has been developed under the MOOSE framework to leverage the available advanced software environments and numerical methods. SAM was initially developed to model the one-dimensional single-phase flow. Recently, a multi-dimensional (Multi-D) capability was added to the SAM code [60]. PROTEUS-NODAL was coupled with both 1-D and Multi-D SAM solvers for MSR applications. For multiphysics simulations of MSRs with the parallel-channel flows in moderator blocks, 1-D SAM was utilized and MSRs with the flows in cylindrical tanks were modeled with Multi-D SAM. Even in the latter case, the outer loop components were modeled with 1-D SAM. In this case, the resulting coupling was among three codes: PROTEUS-NODAL, Multi-D SAM, and 1-D SAM.

Meanwhile, SAM has the capability to simulate the 3-D heat conduction in the core and the conventional heat pipe. The heat transfer inside the heat pipe can be modeled with 2-D RZ heat conduction based on the assumption that the heat pipe vapor core can be modeled as a superconductor of extremely high thermal conductivity [61]. To overcome the difficulties of the current multiphysics analysis tools for micro-reactors, PROTEUS-MOC and SAM are coupled for the multiphysics simulation of micro-reactors.

Because SAM was developed under the MOOSE framework, the PROTEUS and SAM were coupled based on MOOSE framework. The MOOSE framework is an open-source, parallel finite element framework for the development of multiphysics solvers based on Jacobian-free Newton-Krylov (JFNK) methods [62, 63]. MOOSE provides a MOOSE-Wrapping process for coupling external codes that are not originally developed based on the MOOSE framework to MOOSE applications. Since PROTEUS was developed externally under MOOSE framework, a MOOSE wrapper for PROTEUS was developed for coupling to SAM.

1.3 Dissertation Layout

This dissertation is structured in seven chapters. Following the introduction, the theories for the multiphysics simulations of MSR and micro-reactor are discussed in Chapter 2. The systems of nonlinear equations for the coupled multiphysics simulations of MSR and micro-rector in this work are given first. Then the methods for solving the coupled multiphysics problems are presented, including the operator-splitting, Picard iteration, and Jacobian-free Newton-Krylov methods.

In Chapter 3, the coupling schemes of PROTEUS-NODAL and SAM for MSR applications are discussed. The coupling scheme of PROTEUS-NODAL and 1-D SAM is described first. The MOOSE wrapper of PROTEUS-NODAL named TreeFrog is presented. In addition, a master application called TreeKangaroo to control the coupling procedure between PROTEUS-NODAL and 1-D SAM under the MOOSE framework is discussed. At last, the coupling scheme of PROTEUS-NODAL with Multi-D SAM is shown. Chapter 4 presents the verification results of the coupled PROTEUS-NODAL and SAM code system. The analysis results of the steady state and transient problems of the MSFR benchmark problem are discussed. The steady state results of the coupled code system were compared with those of the manually coupled calculation of

PROTEUS-NODAL and the ANSYS CFX. The transient problems include unprotected transient over-power (UTOP), unprotected loss of flow (ULOF), and unprotected loss of heat sink (ULOHS) scenarios. The results were compared to two open literature solutions of other organizations obtained with different code systems.

Chapter 5 provides the validation test results of the coupled PROTEUS-NODAL and SAM code system with the available experimental data of the MSRE problem. First, the MSRE problem is briefly described, and the developed computational models of PROTEUS-NODAL and SAM are discussed. Then, the coupled code system results are compared with the experimental data for the protected pump start-up and pump coast down at zero power, and the natural convection test of MSRE.

Chapter 6 discusses the coupling of PROTEUS-MOC and SAM for micro-reactor simulations. First the MOOSE wrapper of PROTEUS-MOC is presented. Then the coupling scheme of PROTEUS-MOC and SAM is discussed. A unit-cell and one-sixth core problems of a micro-reactor are analyzed to demonstrate the simulation capability of the coupled code system for the heat pipe cooled micro-reactor in both steady state and transient. Finally, Chapter 7 gives the summary of this thesis and potential future work.

Chapter 2 Theory and Methodology

In the nuclear reactor systems, many different physics are involved and interacting with each other, including neutronics, thermal-hydraulics, structural mechanics, chemical reactions, etc. Figure 2.1 shows different physics and their interactions in MSRs. Among these different physics, neutronics and thermal-hydraulics are the primary domains of physics in determining reactor operation and safety. In this work, these two physics are included in the coupled code system for the analysis of MSRs and micro-reactors.

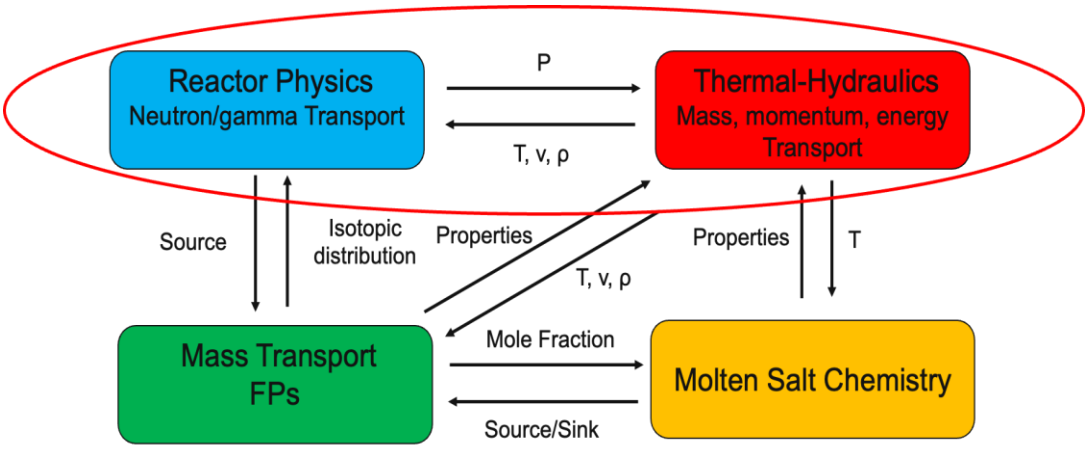


Figure 2.1. Multiphysics and their interactions in the MSRs.

To perform the multiphysics simulations, the coupled system of nonlinear equations needs to be solved. In this chapter, first the coupled systems of equations for MSR and micro-reactor are presented. Then different coupling methods to solve the coupled system of nonlinear equations are discussed.

2.1 Multiphysics Problems of MSR and Micro-reactor

2.1.1 Multiphysics Problem of MSR

In the coupled neutronics and thermal-hydraulics calculations of MSRs, the multigroup neutron diffusion equations, delayed neutron precursor equations, and mass, momentum, and energy conservation equations for single-phase flow are solved. The multigroup neutron diffusion equation and the delayed neutron precursor concentration equation can be written as

$$\begin{aligned}\frac{1}{v_g}\frac{\partial}{\partial t}\phi_g(\vec{r},t)-\nabla\cdot D_g(\vec{r},t)\nabla\phi_g(\vec{r},t)+\Sigma_{tg}(\vec{r},t)\phi_g(\vec{r},t)=\sum_{g'=1}^{G}\Sigma_{sg'g}(\vec{r},t)\phi_{g'}(\vec{r},t)\\ +\chi_{pg}(\vec{r},t)\sum_{g'=1}^{G}\nu_p\Sigma_{fg'}(\vec{r},t)\phi_{g'}(\vec{r},t)+\sum_{k=1}^{K}\chi_{dkg}(\vec{r},t)\lambda_k C_k(\vec{r},t),\quad g=1,2,\cdots,G,\end{aligned} \tag{2.1}$$

$$\frac{\partial}{\partial t}C_k(\vec{r},t)+\nabla\cdot[\mathbf{V}(\vec{r},t)C_k(\vec{r},t)]+\lambda_k C_k(\vec{r},t)=\lambda\sum_{g'=1}^{G}\nu_{dk}\Sigma_{fg'}(\vec{r},t)\phi_{g'}(\vec{r},t),\quad k=1,2,\cdots,K\ , \tag{2.2}$$

where

$\vec{r}$	=	position vector.
t	=	time variable.
g	=	neutron energy group index, $g=1,2,\cdots,G$.
v_g	=	neutron velocity.
ϕ_g	=	neutron scalar flux.
Σ_{tg}	=	macroscopic total cross section.
Σ_{fg}	=	macroscopic fission cross section.
$\Sigma_{sg'g}$	=	macroscopic scattering cross section from group g' to group g.
k	=	delayed neutron precursor family index, $k=1,2,\cdots,K$.
C_k	=	concentration of delayed neutron precursor of family k.
λ_k	=	decay constant of precursor family k.
$\mathbf{V}$	=	velocity vector.
χ_{pg}	=	fraction of prompt neutrons emitted into the energy group g.
χ_{dkg}	=	fraction of delayed neutrons emitted into the energy group g from the precursor family k.
ν_p	=	number of prompt neutrons per fission.
ν_{dk}	=	number of delayed neutrons of precursor group k per fission.

$\lambda = 1/k_{eff}$ = eigenvalue of the problem.

For MSRs with flowing fuels, the delayed neutron precursor equations are different from those for the stationary fuel because of the motion of the fuel salt. The delayed neutron precursor equation for flowing fuel, Eq. (2.2) contains a precursor drift term $\nabla \cdot [\mathbf{V}(\vec{r},t)C_k(\vec{r},t)]$. The mass, momentum, and energy conservation equations for fluid are

$$\frac{\partial \rho}{\partial t} + \nabla \cdot (\rho \mathbf{V}) = 0, \tag{2.3}$$

$$\rho \frac{\partial \mathbf{V}}{\partial t} + \rho(\mathbf{V} \cdot \nabla)\mathbf{V} + \nabla p - \rho \mathbf{g} - \nabla \cdot \boldsymbol{\tau} = 0, \tag{2.4}$$

$$\rho C_p \frac{\partial T}{\partial t} + \rho C_p \mathbf{V} \cdot \nabla T - \nabla \cdot (k \nabla T) - q''' = 0, \tag{2.5}$$

where $\mathbf{V} = [V_x, V_y, V_z]^T$ is the velocity vector, $\boldsymbol{\tau}$ is the viscous tensor, ρ, h, and p are the density, velocity, enthalpy, and pressure of the fluid, respectively, q''' is the volumetric heat source, and g is the gravitational acceleration. If assuming the flow is not in high compressible conditions, the viscous tensor $\boldsymbol{\tau}$ can be calculated as

$$\nabla \cdot \boldsymbol{\tau} = \mu \nabla^2 \mathbf{V}, \tag{2.6}$$

where μ is the molecular viscosity. Substitute Eq. (2.6) into Eq. (2.4), the momentum equation can be obtained as

$$\rho \frac{\partial \mathbf{V}}{\partial t} + \rho(\mathbf{V} \cdot \nabla)\mathbf{V} + \nabla p - \rho \mathbf{g} - \mu \nabla^2 \mathbf{V} = 0. \tag{2.7}$$

To consider the turbulence effects, the molecular viscosity μ is replaced with the effective viscosity μ_{eff}

$$\rho \frac{\partial \mathbf{V}}{\partial t} + \rho(\mathbf{V} \cdot \nabla)\mathbf{V} + \nabla p - \rho \mathbf{g} - \mu_{eff} \nabla^2 \mathbf{V} = 0, \tag{2.8}$$

$$\mu_{eff} = \mu + \mu_t \,, \tag{2.9}$$

where μ_t is the turbulent viscosity. If only one-dimensional flow is considered, the mass, momentum, and energy conservation equations for fluid can be written as

$$\frac{\partial \rho}{\partial t} + \frac{\partial (\rho u)}{\partial z} = 0 \,, \tag{2.10}$$

$$\frac{\partial (\rho u)}{\partial t} + \frac{\partial (\rho u u + p)}{\partial z} = -\rho \mathbf{g} - \frac{f}{D_e} \frac{\rho u |u|}{2} \,, \tag{2.11}$$

$$\frac{\partial (\rho h)}{\partial t} + \frac{\partial (\rho u h)}{\partial z} = q''' \,. \tag{2.12}$$

The multigroup neutron diffusion equations, delayed neutron precursor equation, and mass, momentum, and energy conservation equations for fluid are coupled and result in a system of nonlinear equations. The cross sections at neutronics equations (2.1) and (2.2) are dependent on the temperature and density, which are solutions from the thermal-hydraulics equations (2.3), (2.4) , and (2.5). Meanwhile, the volumetric heat source q''' in Eq. (2.5) is from the solution of neutronics equations (2.1) and (2.2).

2.1.2 Multiphysics Problem of Micro-reactor

In the coupled neutronics and thermal-hydraulics calculations of micro-reactor, the multigroup neutron transport equations, delayed neutron precursor equations, and heat conduction equations are solved. The time-dependent neutron transport equations or Boltzmann equations with the delayed neutron precursor equations solved are described as

$$\frac{1}{v_g}\frac{\partial \psi_g\left(\vec{\mathbf{r}},\vec{\mathbf{\Omega}},t\right)}{\partial\, t}+\left[\vec{\mathbf{\Omega}}\cdot\nabla+\Sigma_{t,g}\left(\vec{\mathbf{r}},t\right)\right]\psi_g\left(\vec{\mathbf{r}},\vec{\mathbf{\Omega}},t\right)$$

$$=\sum_{g'=1}^{G}\int_{4\pi}\Sigma_{s,g'\to g}\left(\vec{\mathbf{r}},\vec{\mathbf{\Omega}}\cdot\vec{\mathbf{\Omega}}'\right)\psi_{g'}(\vec{\mathbf{r}},\vec{\mathbf{\Omega}}')d\Omega' \quad , \tag{2.13}$$

$$+\frac{\chi_{p,g}\left(\vec{\mathbf{r}}\right)}{4\pi}\sum_{g'=1}^{G}\nu\Sigma_{f,g'}\left(\vec{\mathbf{r}}\right)\phi_{g'}\left(\vec{\mathbf{r}}\right)+\frac{1}{4\pi}\sum_{k=1}^{K}\chi_{dk,g}\left(\vec{\mathbf{r}}\right)\lambda_k C_k\left(\vec{\mathbf{r}},t\right)$$

$$\frac{\partial C_k\left(\vec{\mathbf{r}},t\right)}{\partial t}=-\lambda_k C_k\left(\vec{\mathbf{r}},t\right)+\sum_{g'=1}^{G}\nu_{dk}\Sigma_{f,g'}\left(\vec{\mathbf{r}}\right)\phi_{g'}\left(\vec{\mathbf{r}}\right), \tag{2.14}$$

where ψ is the neutron angular flux and Ω is the angular direction. For the heat conduction calculations, the governing equation is:

$$\rho C_p\frac{\partial T}{\partial t}-\nabla\cdot(k\nabla T)=q''', \tag{2.15}$$

where T is the solid temperature, ρ is the density, C_p is the specific heat, k is the thermal conductivity, q''' is the volumetric heat source. The one-dimensional, two-dimensional, and three-dimensional heat conduction calculations are utilized in the micro-reactor simulations. The one-dimensional and two-dimensional heat conduction are utilized to calculate the temperature distributions in the heat exchanger tubes, pipe walls, and heat pipes. The three-dimensional heat conduction is utilized to calculate the core temperature distributions in micro-reactor.

The equations (2.13), (2.14), and (2.15) form a system of nonlinear equations. The cross sections at neutronics equations depend on the solutions of thermal-hydraulics equations and the power density distributions in the thermal-hydraulics equations are from the solution of neutronics equations. Assuming the solutions from thermal-hydraulics equations are known, the Eq. (2.13) can be solved efficiently utilizing the 2D/3D MOC scheme [59] with coarse mesh finite difference (CMFD) acceleration. For the micro-reactor problems, the unstructured CMFD (uCMFD) scheme was developed [58].

2.2 Methods for Solving the Coupled Multiphysics Problems

The approaches for solving the coupled systems of nonlinear equations in multiphysics simulations can be divided into two methods [64]. In the first approach, all the equations involved in different physics are solved together, which is known as the "fully-coupled" approach. JFNK Method is one of the "fully-coupled" approaches. In the other approach, different physics are solved in different codes, and these codes are coupled with certain data passing interfaces. To use already developed and optimized codes for a given physics, i.e., PROTEUS for neutronics analysis, the second approach is more appropriate than the "fully-coupled" approach. Picard iteration and operator-splitting schemes both belong to the second coupling approach and these two methods are utilized in this work. In the Picard iteration scheme, different physics are solved iteratively within a time step in transient until all the physics are converged. While in the operator-splitting scheme, each physics is solved sequentially and only once in each time step.

2.2.1 Operator-Splitting Method

In the nuclear reactor research community, many codes have been developed and verified for solving specific physics during the past several decades. The operator-splitting method is widely used to solve the multiphysics problem while utilizing the developed single physics codes. In the operator-splitting method, each physics is solved with the solutions from other physics. The other physics codes work as "black-box" for certain codes. There is no iteration between different codes within one time step. The modifications of existing codes to couple with different codes using the operator-splitting method are minimal compared to other methods. The overall accuracy for the coupling method is first order $O(\Delta t)$, although higher order time integration schemes are used for individual physics [65]. To obtain an accurate solution and avoid instability issues, a small time step size is usually required in the coupled simulation with the operator-splitting method.

Assuming the neutronics equations are solved first at each time step, the operator-splitting method for the coupled neutronics and thermal-hydraulics simulation can be described as below:

$$\mathbf{F}(\mathbf{x}^{n+1}, \mathbf{y}^{n}) = \mathbf{0}\,, \tag{2.16}$$

$$\mathbf{G}(\mathbf{y}^{n+1}, \mathbf{x}^{n+1}) = \mathbf{0}\,, \tag{2.17}$$

where **F** is the non-linear operator representing the neutronics equations, **G** is the non-linear operator representing the thermal-hydraulics equations, **x** is the solution vector for neutronics equations, and **y** is the solution vector for the thermal-hydraulics equations, the superscript n represents the time step n.

At time step n+1, the neutronics equations are solved first with the solution of thermal-hydraulics equations from time step n, then the solution of neutronics equations at time step n+1 is transferred to the thermal-hydraulics solver. The thermal-hydraulics equations are solved with the solution of neutronics equations at time step n+1. At the end of the time step, the thermal-hydraulics variables are transferred to the neutronics solver to be used in the next time step. This process is shown in Fig. 2.2.

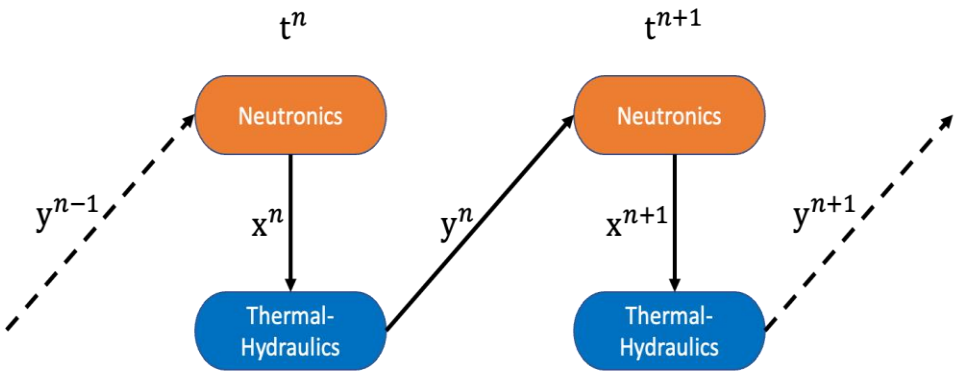


Figure 2.2. The operator-splitting method in coupled neutronics and thermal-hydraulics.

2.2.2 Picard Iteration Method

In the Picard iteration method, each physics is solved by treating other physics as "black-box", which is similar to the operator-splitting method. Thus, the existing codes for single physics can be utilized with modifications for the implementation of the Picard iteration method in multiphysics problems. The difference between the Picard iteration and the operator-splitting methods is that there are iterations between different codes in the Picard iteration. Each single physics code is executed in one time step, and the updated solutions are transferred to other codes several times until the changes between two succeeded iterations are small enough. Based on the order of executing the single physics code, the Picard iteration can be divided into two types [66]: the first type is named "block Jacobi," in which each physics is solved then the coupling parameters are calculated and transferred. The second type is called "block Gauss-Seidel," in which each physics is solved sequentially and data are transferred to other physics once it is obtained. It is expected that the block Gauss-Seidel converges faster than the block Jacobi. The Picard iteration used in this work is based on the block Gauss-Seidel method. The block Gauss-Seidel Picard iteration can be described below

$$\mathbf{F}(\mathbf{x}_{i+1}^{n+1}, \mathbf{y}_{i}^{n+1}) = \mathbf{0}, \tag{2.18}$$

$$\mathbf{G}(\mathbf{y}_{i+1}^{n+1}, \mathbf{x}_{i+1}^{n+1}) = \mathbf{0}, \tag{2.19}$$

where the subscript i means the i^{th} Picard iteration, the solution vectors with the Picard iteration number 0 are the solutions from the last time step

$$\mathbf{x}_{0}^{n+1} = \mathbf{x}^{n}, \tag{2.20}$$

$$\mathbf{y}_{0}^{n+1} = \mathbf{y}^{n}. \tag{2.21}$$

At the i+1$^{\text{st}}$ Picard iteration of the time step n+1, the neutronics equations are solved first with the solution of the thermal-hydraulics equations from the last Picard iteration i, $\mathbf{y}_{i}^{n+1}$. The updated solution of neutronics equations at iteration i+1 is transferred to the thermal-hydraulics solve and

the thermal-hydraulics equations are solved with the latest neutronics solution. This process is repeated until convergence is achieved. The overall process is shown in Fig. 2.3.

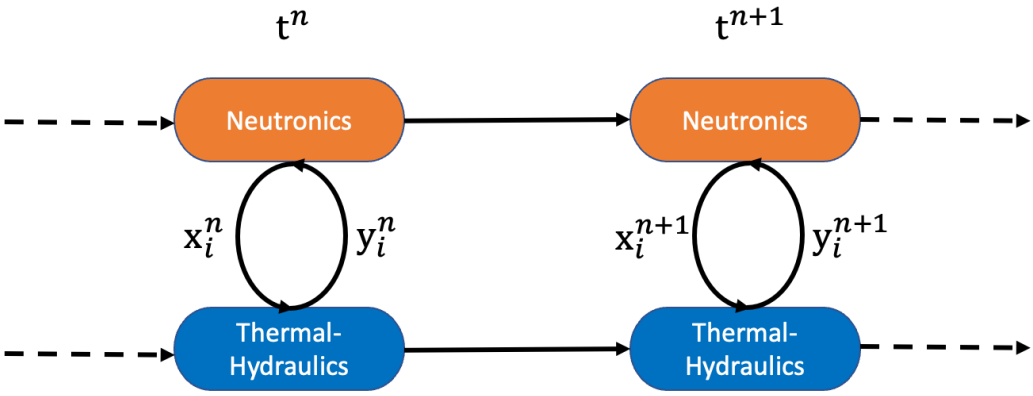


Figure 2.3. Picard iteration method in coupled neutronics and thermal-hydraulics.

2.2.3 Jacobian-Free Newton-Krylov Method

The JFNK methods are synergistic combinations of Newton-type methods for nonlinear iteration and Krylov subspace methods for solving the linear equations [63, 67]. As mentioned before, the JFNK method belongs to the "fully-coupled" approach. Different from the operator-splitting and Picard iteration method, in which individual physics are solved separately, all the physics are solved simultaneously through forming a large nonlinear algebraic system in the JFNK method. Because the Newton method is utilized for nonlinear iterations, the JFNK method can achieve a better convergence rate than the Picard iteration. Another advantage of the JFNK method is that the Jacobian matrix is not formed explicitly, which saves time for computing the Jacobian matrix and the memory to store the Jacobian matrix.

The discretized nonlinear system for a multi-physics problem can be expressed as:

$$\mathbf{F}(\mathbf{x}) = \mathbf{0}\,, \tag{2.22}$$

where **F** represents the non-linear operator of the discretized equations for the multi-physics problem, and **x** is the solution vector for the equations. The Jacobian of this system is defined as

$$\mathbf{J(x)} = \frac{\partial \mathbf{F(x)}}{\partial \mathbf{x}}, \tag{2.23}$$

In the Newton method, the Eq. (2.22) is solved iteratively

$$\begin{aligned} &\mathbf{J}(\mathbf{x}^k)\delta\mathbf{x}^k = -\mathbf{F}(\mathbf{x}^k) \\ &\mathbf{x}^{k+1} = \mathbf{x}^k + \delta\mathbf{x}^k, k = 0,1,\ldots \end{aligned}. \tag{2.24}$$

To solve Eq. (2.24) with a Krylov method, such as the generalized minimum residual algorithms (GMRES) [68], the Jacobian matrix itself is not required but the Jacobian matrix times a vector is calculated. This matrix-vector product $\mathbf{J}(\mathbf{x}^k)\mathbf{v}$ can be approximated by the finite difference method as

$$\mathbf{J}(\mathbf{x}^k)\mathbf{v} \approx \frac{\mathbf{F}(\mathbf{x}^k + \varepsilon\mathbf{v}) - \mathbf{F}(\mathbf{x}^k)}{\varepsilon}, \tag{2.25}$$

where ε is a small perturbation, and $\mathbf{v}$ is the Krylov vector. By utilizing Eq. (2.25) in the Krylov method, Eq. (2.24) can be solved in a Jacobian-free way. To solve Eq. (2.24) efficiently with the JFNK method, a proper preconditioner is needed. The right preconditioning of Eq. (2.24) is written as

$$\mathbf{J}(\mathbf{x}^k)\mathbf{P}^{-1}(\mathbf{P}\delta\mathbf{x}^k) = -\mathbf{F}(\mathbf{x}^k), \tag{2.26}$$

where $\mathbf{P}$ is the preconditioning matrix. In each iteration, first solve

$$(\mathbf{J}(\mathbf{x}^k)\mathbf{P}^{-1})\mathbf{v} = -\mathbf{F}(\mathbf{x}^k), \tag{2.27}$$

for $\mathbf{v}$. Then solve

$$\delta\mathbf{x}^k = \mathbf{P}^{-1}\mathbf{v}, \tag{2.28}$$

for $\delta\mathbf{x}^k$.

However, the JFNK method needs to access the solution vector and its residual. Many existing codes for single physics are working as black-box and this information is not accessible, or even residual might not be computed inside. It requires significant modifications of existing codes to couple with the JFNK method. Thus in this work, the JFNK method is not utilized for the multiphysics coupling of PROTEUS and SAM. While SAM, built on the MOOSE framework, uses the JFNK method internally to solve the discretized governing equations.

2.3 Summary

This chapter provided the theoretical foundations of the coupled multiphysics calculations of MSR and micro-reactor. The systems of the nonlinear equations for the coupled neutronics and thermal-hydraulics calculations of MSR with flowing fuel were presented first. The system of the multigroup neutron diffusion equations, delayed neutron precursor equations, and mass, momentum, and energy conservation equations for single-phase flow was solved in the coupled calculations of MSR. The delayed neutron precursor equations for MSR with flowing fuel include an additional precursor drift term compared to those for the stationary fuel. In the coupled multiphysics simulations of micro-reactor, the coupled system of the multigroup neutron transport equations, delayed neutron precursor equations, and heat conduction equation was solved.

To solve the coupled equations in the multiphysics simulations of MSR and micro-reactor, the operator-splitting and Picard iteration methods were applied in this work. In the operator-splitting and Picard iteration methods, different physics are solved in different codes, and these codes are coupled with certain data passing interfaces. Thus, the existing codes for single physics can be utilized with modifications in solving the multiphysics problems with the operator-splitting and Picard iteration methods. In contrast, all the physics are solved simultaneously by forming a large nonlinear algebraic system in the JFNK method. Because significant modifications of

existing codes are required in the JFNK method, it is not utilized in the multiphysics coupling of PROTEUS and SAM in this work.

Chapter 3 Multiphysics Coupling of PROTEUS-NODAL and SAM for MSRs Applications

In this chapter, the coupling schemes of PROTEUS-NODAL and SAM for MSR applications are presented. The coupled code system was initially developed between 1-D SAM and PROTEUS-NODAL. Recently, a multi-dimensional capability was added to the SAM code [69]. Thus the coupled code system was extended to include the Multi-D SAM solvers. For parallel-channel flow within moderator blocks, 1-D SAM is used. On the other hand, the flows in cylindrical tanks of non-negligible lateral flow are modeled with Multi-D SAM. Even in the latter case, the outer loop components are modeled with 1-D SAM, thus Multi-D SAM and 1-D SAM are coupled at the fluid-fluid interfaces at the bottom and top of the core. In this case, the resulting coupling is among three codes: PROTEUS-NODAL, Multi-D SAM, and 1-D SAM.

Since PROTEUS-NODAL is not an application of the MOOSE framework, a MOOSE wrapper named TreeFrog was developed to couple PROTEUS-NODAL with other MOOSE applications. In addition, a master application named TreeKangaroo was developed to control the coupling procedure between PROTEUS-NODAL and 1-D SAM under the MOOSE framework.

3.1 Coupling of PROTEUS-NODAL with 1-D SAM

3.1.1 PROTEUS-NODAL Wrapper TreeFrog

In the MOOSE framework, packages for solving different physics are referred to as “applications” since they are not standalone, and their executions need the MOOSE framework. These applications share common software design and library dependencies, so they are highly

"cohesive" [70]. Due to the benefit of cohesiveness, loose coupling between different MOOSE applications can be performed relatively easily through MOOSE MultiApps and Transfers systems. In the MultiApps system, multiple independent applications can be defined in a tree-like, multi-level structure shown in Fig. 3.1. A master application controls its sub-applications. The Transfer system provides the functions to transfer the solution data between applications in the MultiApps system.

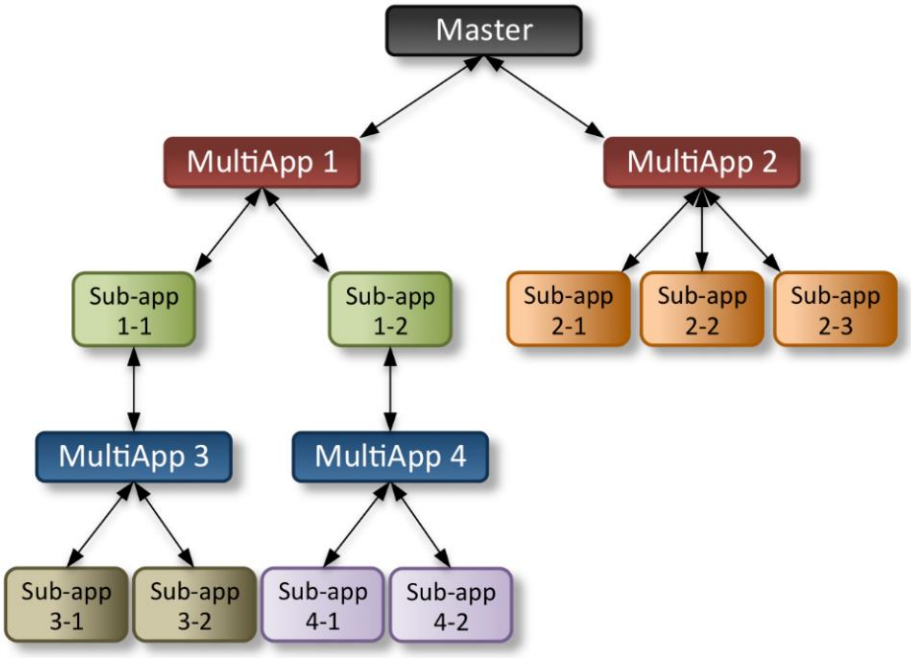


Figure 3.1. MOOSE MultiApps system [25].

For coupling of external codes that are not originally developed based on the MOOSE framework to MOOSE applications in a "cohesive-like" manner to utilize the MOOSE MultiApps and Transfers systems, MOOSE provides a method called "MOOSE-Wrapped Apps." In the MOOSE-Wrapping process, two main objects need to be defined for a wrapped application: "ExternelMesh" and "ExternalProblem." The ExternelMesh object is the native MOOSE format mesh that holds the geometry and solution information of the external code to be wrapped. The

ExternalProblem object contains the interface functions for executing the external code and transferring data between the ExternelMesh and the external code. Through this MOOSE-Wrapping process, the external code can be coupled to other MOOSE-based applications by utilizing MOOSE MultiApps and Transfers systems in a two-way, in-memory style.

PROTEUS-NODAL is wrapped inside a MOOSE application called TreeFrog. In TreeFrog, an ExternalProblem object for PROTEUS-NODAL is defined with three main functions: one for the execution of PROTEUS-NODAL solver and the other two for data transfer to and from PROTEUS-NODAL. A MOOSE-based TreeFrog mesh is defined to store data to be passed from and to PROTEUS-NODAL such as power density, fuel salt temperature, density, and velocity. TreeFrog communicates with PROTEUS-NODAL before and after running PROTEUS-NODAL at each time step to ensure that the data are up to date. PROTEUS-NODAL is compiled as a dynamic library such that the subroutines of PROTEUS-NODAL can be accessed from TreeFrog. At the beginning of the calculations, TreeFrog calls the subroutines that read the PROTEUS-NODAL input files and initialize the relevant variables. Then the executioner runs PROTEUS-NODAL at each time step in the transient simulation or each Picard iteration in the steady-state simulation.

When coupled to 1-D SAM, the axial mesh size of TreeFrog is set to be equal to that of the SAM channel to facilitate the data transfer between TreeFrog and 1-D SAM. The variables in TreeFrog meshes and those in the nodes of PROTEUS-NODAL are transferred with appropriate interpolation and integration. The power densities in TreeFrog meshes are obtained by interpolating the intra-nodal flux of the corresponding node of PROTEUS-NODAL along the axial direction. The average fuel density in a PROTEUS-NODAL node is evaluated by integrating the fuel densities in the corresponding TreeFrog meshes based on the piece-wise linear interpolation.

The average fuel temperature and velocity in a PROTEUS-NODAL node are obtained with density-weighted integration of each variable based on the piece-wise linear interpolation.

3.1.2 Overall Computational Procedure in TreeKangaroo

A master application named TreeKangaroo was developed to control TreeFrog and 1-D SAM as independent sub-applications. Figure 3.2 shows the data flow between PROTEUS-NODAL and 1-D SAM using TreeKangaroo as the master application. Data are transferred between TreeFrog and TreeKangaroo using the MOOSE function "MultiAppCopyTransfer," which supports the transfer of all kinds of variables between the two applications when the meshes are identical. Two MOOSE functions "MultiAppVPPTransfer" and "MultiAppPowerTransfer" are added to TreeKangaroo to transfer data between TreeKangaroo and 1-D SAM.

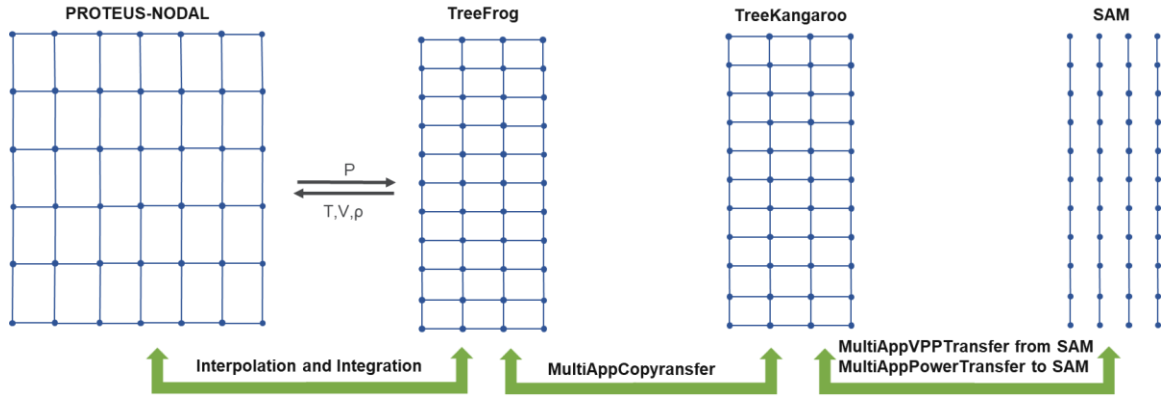


Figure 3.2. Data flow between PROTEUS-NODAL and 1-D SAM under the MOOSE framework.

For steady-state calculations, the Picard iteration is utilized as shown in Fig. 3.3. Within each iteration, TreeFrog and SAM are executed sequentially. At the beginning of the PROTEUS-NODAL calculation, the cross sections are updated using the temperature and density distributions of SAM result from the previous iteration. With the velocity field from SAM and updated cross sections, the neutronics calculation is performed and the power density distribution is updated.

With the new power density transferred from TreeFrog, SAM calculation is performed once again. The convergence is checked by comparing the maximum relative errors in power and temperature between two successive Picard iterations. The Picard iteration is continued until the convergence criteria are met.

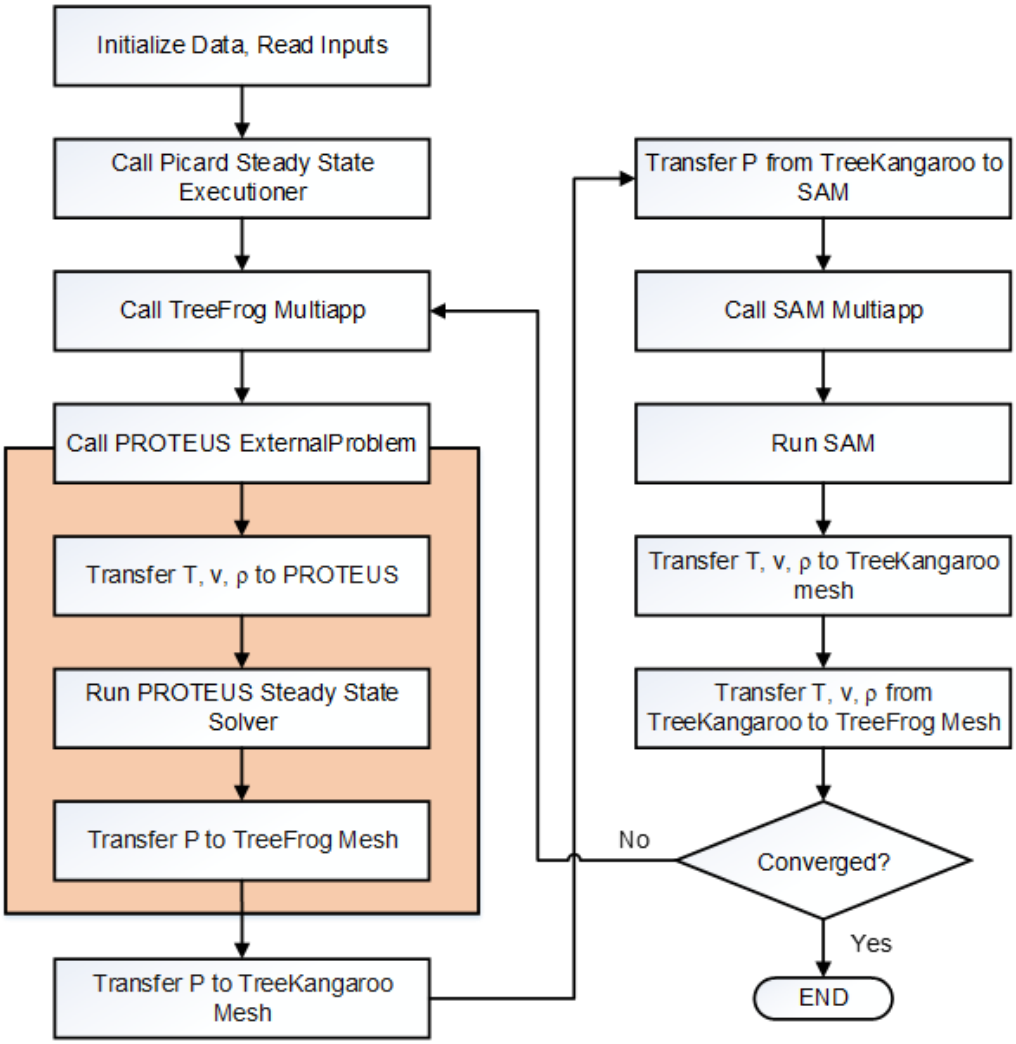


Figure 3.3. Coupling scheme with Picard iteration for steady-state calculations.

For transient calculations, the conventional operator splitting technique is used instead of the Picard iteration, as shown in Fig. 3.4. Transient calculations are performed after 1-D SAM and PROTEUS-NODAL read their restart files containing the steady-state solutions. To allow different

time step sizes between PROTEUS-NODAL and 1-D SAM, the “sub-cycling” option defined in the transient executioner of the MOOSE framework is activated. With the sub-cycling option, sub-applications can take multiple time steps during a single time step of the master application. Thus, the time step size of TreeKangaroo is selected as the larger one of those specified in the PROTEUS-NODAL and 1-D SAM inputs. Within each time step of TreeKangaroo, the sub-application with the larger time step size will be executed once, and the other with the smaller time step size is executed multiple times until the time reaches the time of TreeKangaroo.

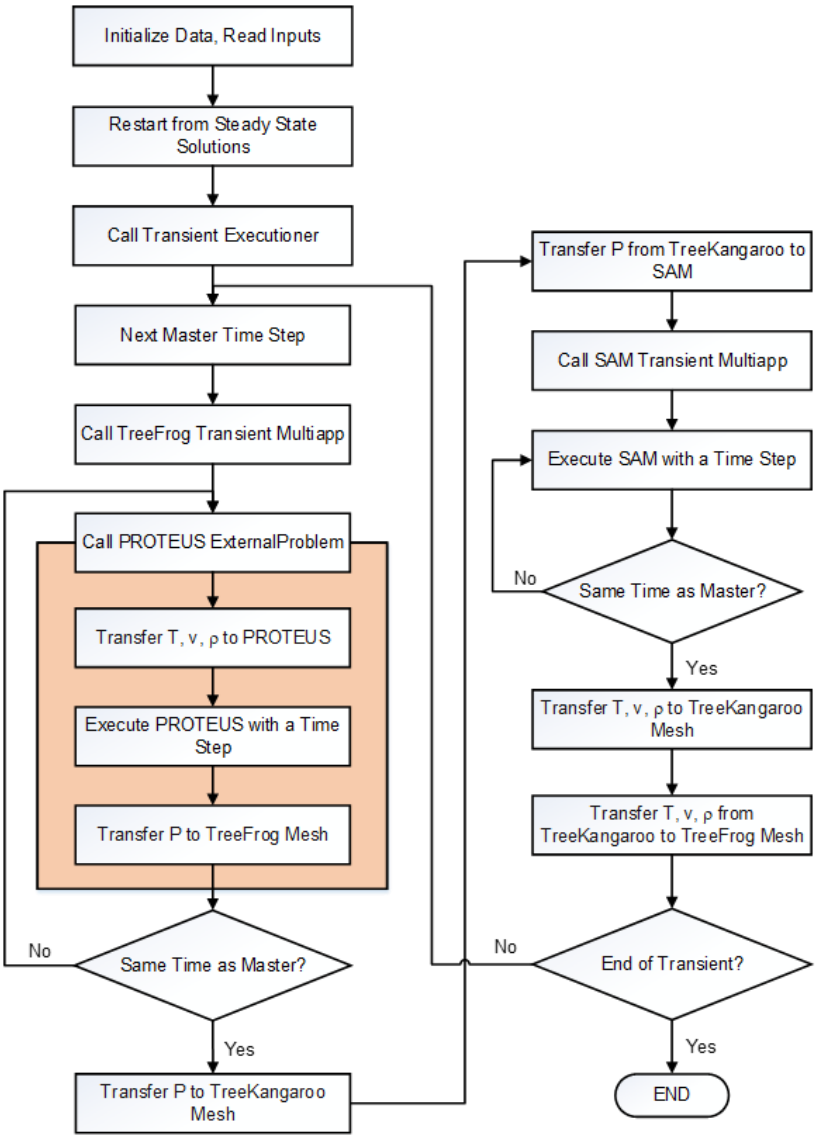


Figure 3.4. Coupling scheme with operator splitting for transient calculations.

3.2 Coupling of PROTEUS-NODAL with Multi-D SAM

For coupling of PROTEUS-NODAL with Multi-D SAM, TreeFrog is utilized as the wrapper for the PROTEUS-NODAL as in the case of coupling with 1-D SAM. Multi-D SAM is served as the master application that controls the execution of two sub-applications: TreeFrog and 1-D SAM. In this part, the data transfer between Multi-D SAM and PROTEUS-NODAL is based on the field mapping. Meanwhile, the data transfer between Multi-D SAM and 1-D SAM is performed using the post-processed scalar values at the fluid-fluid coupling interfaces.

As described in Section 3.1, in the coupling of PROTEUS-NODAL with 1-D SAM, the axial mesh size of TreeFrog is set equal to that of the SAM channel. However, in the coupling of PROTEUS-NODAL with Multi-D SAM, the axial and radial mesh numbers of TreeFrog are the same as those of PROTEUS-NODAL. The variables in TreeFrog meshes and those in the PROTEUS-NODAL nodes are transferred by a direct copy. Figure 3.5 illustrates the data transfer between different codes in this coupling scheme. Data are transferred between the TreeFrog mesh and the Multi-D SAM mesh using the MOOSE projection function. In the coupling of Multi-D SAM and 1-D SAM, the required information to be transferred between the two applications arises from the fluid-fluid interfaces. In this coupled scheme, the inlet velocity and outlet pressure boundary conditions are applied in both Multi-D SAM and 1-D SAM. At the inlet boundary of Multi-D SAM, the uniform temperature and velocity are transferred to Multi-D SAM, and the pressure value is sent to 1-D SAM. At the outlet boundary of Multi-D SAM, Multi-D SAM receives the pressure value and sends out the average temperature and velocity to 1-D SAM.

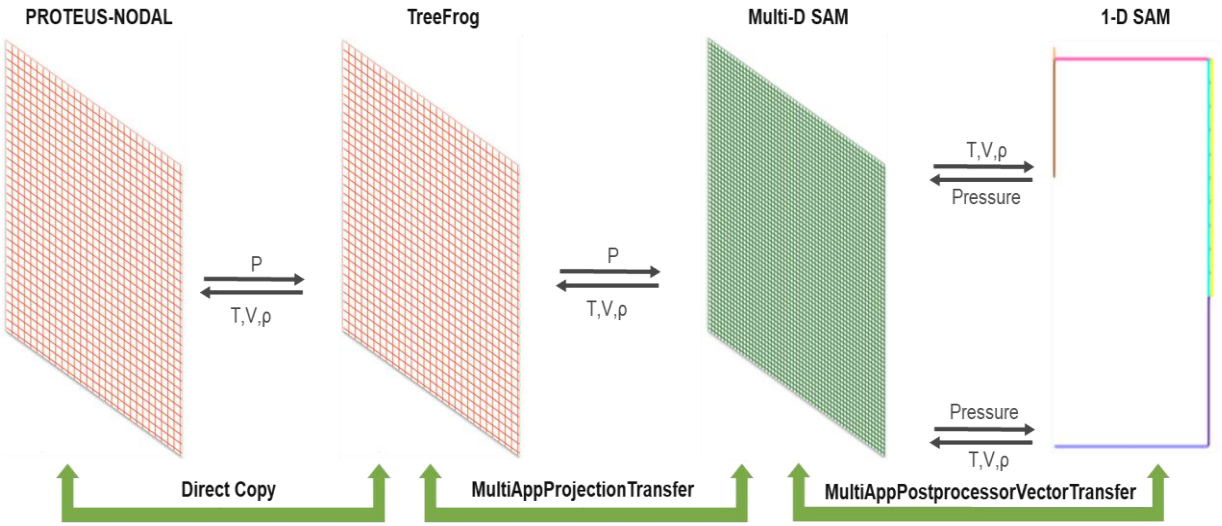


Figure 3.5. Data flow and coupling scheme between PROTEUS-NODAL, Multi-D SAM, and 1-D SAM under the MOOSE framework.

Figure 3.6 shows the computational flow for steady-state calculations. The coupled calculation for the steady-state problem is performed as a null transient. At each time step of Multi-D SAM, the steady state solver of PROTEUS-NODAL is called first using the temperature, velocity, and density information of Multi-D SAM obtained at the previous time step, and then the transient solver of Multi-D SAM is executed using the updated power from PROTEUS-NODAL. At the end of a time step, 1-D SAM is called with the updated boundary conditions from Multi-D SAM. The calculation is terminated once the steady-state is reached. The steady-state convergence criterion is reached if two successive iterative solutions satisfy the following condition:

$$\frac{\left\| u^{n+1} - u^{n} \right\|_2}{\Delta t} < \tau \left\| u \right\|_2^{n+1}, \tag{3.1}$$

where u is the field variables, n is the iteration index, Δt is the time step size, τ is the user specified tolerance limit, and $\left\| \bullet \right\|_2$ denotes the l_2 norm.

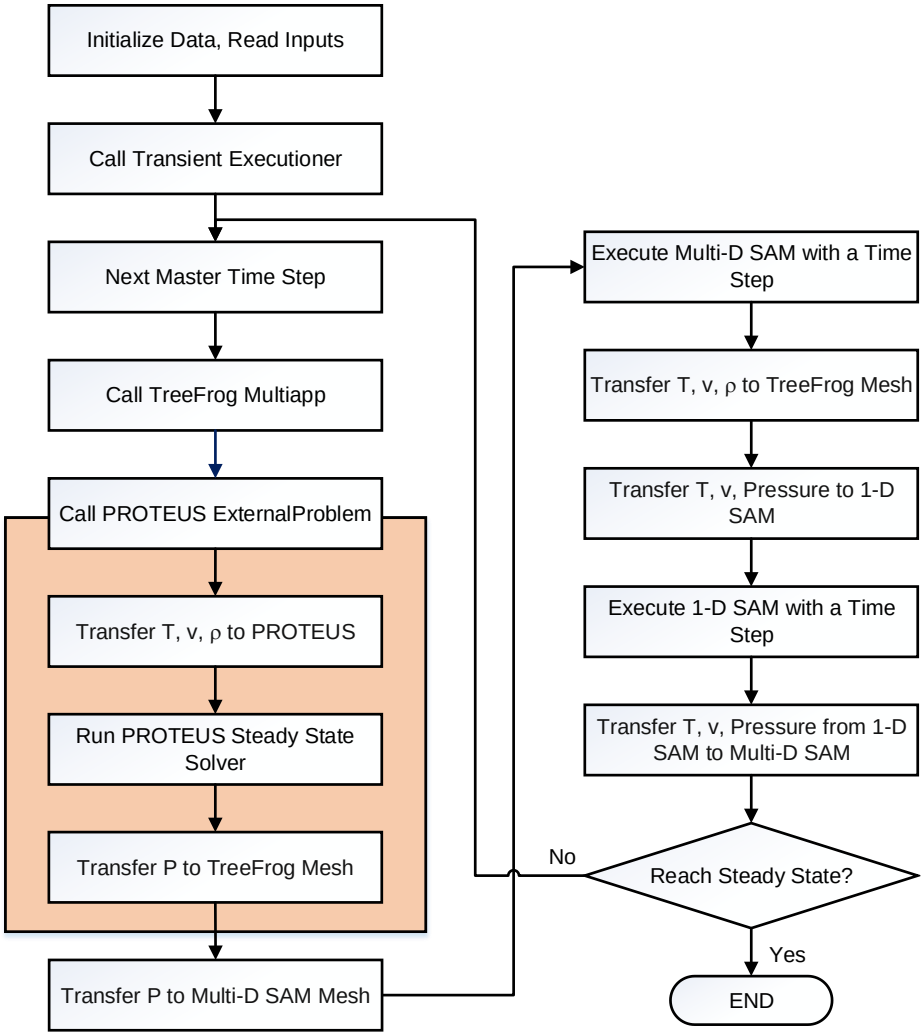


Figure 3.6. Coupling scheme of PROTEUS-NODAL and Multi-D SAM for steady-state calculations.

For transient calculations, the operator splitting technique is used as shown in Fig. 3.7. Transient calculations are performed after Multi-D SAM, and 1-D SAM and PROTEUS-NODAL read the initial conditions from their restart files that contain the steady-state solutions. As the time step size of the SAM calculation does not need to be as small as that of the PROTEUS-NODAL calculation, the sub-cycling option defined in the transient executioner of the MOOSE framework is utilized to allow different time step sizes between PROTEUS-NODAL and SAM.

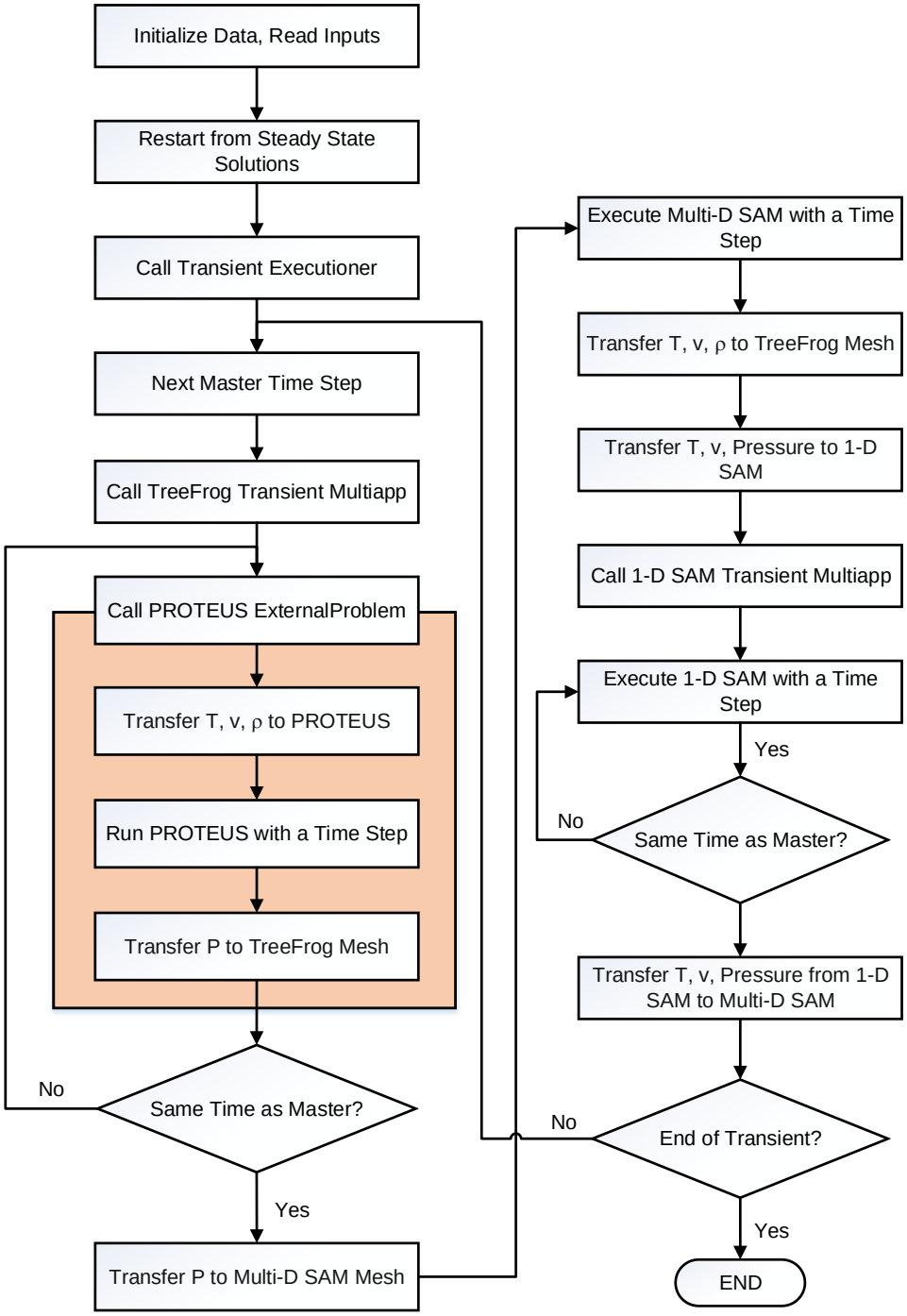


Figure 3.7. Coupling scheme of PROTEUS-NODAL and Multi-D SAM for transient calculations.

3.3 Summary

This chapter discussed the coupling schemes of PROTEUS-NODAL and SAM for MSR applications. For MSR with the parallel-channel flow in moderator blocks, coupled PROTEUS-NODAL and 1-D SAM was utilized. While for MSR with the flow in a cylindrical tank, coupled PROTEUS-NODAL and Multi-D SAM was used. The coupled PROTEUS-NDOAL and SAM code system was developed under MOOSE framework. Since PROTEUS-NODAL was not an application of the MOOSE framework, a MOOSE wrapper named TreeFrog was developed to couple PROTEUS-NODAL with SAM. In addition, a master application named TreeKangaroo was developed to control the coupling procedure between PROTEUS-NODAL and 1-D SAM under the MOOSE framework.

The Picard iteration was utilized in coupled steady-state calculations, and the operator-splitting method was used in coupled transient calculations. In the coupling of PROTEUS-NODAL and Multi-D SAM, Multi-D SAM is served as the master application which controls the execution of TreeFrog and 1-D SAM. The verification tests are presented in the following chapter with the MSFR benchmark problem. The validation tests are provided in Chapter 4 with the MSRE experiments.

Chapter 4 Verification of Coupled PROTEUS-NODAL and SAM Code System

To verify the coupled system of PROTEUS-NODAL and SAM, the steady-state and transient problems of the MSFR benchmark problem [8] were analyzed. The performance of SAM is first examined by comparing the steady-state solutions of PROTEUS-NODAL and SAM with those of manually coupled calculation of PROTEUS-NODAL and the commercial CFD software, ANSYS CFX [71]. In this comparison, the outer loop was not modeled, and the same inlet and outlet boundary conditions were applied in all 1-D SAM, Multi-D SAM, and ANSYS CFX. Then, the transient problems of the MSFR benchmark were solved with the coupled system of PROTEUS-NODAL and 1-D SAM as well as the coupled system of PROTEUS-NODAL and Multi-D SAM, including the external loop modeled in 1-D SAM. The results were compared with the other solutions from the open literature.

4.1 MSFR Benchmark Problem

The MSFR benchmark problem was developed under the EURATOM EVOL project [8]. It is a 3000 MWth fast spectrum reactor design with the thorium fuel cycle. The initial fuel salt can be composed of LiF-ThF_4-$^{233}UF_4$ or LiF-ThF_4-$(TRU)F_3$. A schematic representation of the MSFR core is shown in Fig. 4.1. The fuel salt is circulated in the cylindrical core and 16 external loops. The total fuel salt volume is 18 m^3, half of which is in the active core. The thick reflectors made of nickel-based alloys are designed to be located above and below the core. In the radial direction, a fertile blanket composed of LiF-ThF_4 salt surrounds the core to increase the breeding ratio and shield the external components. A B_4C layer is placed outside the blanket for shielding

purposes. The designed core inlet and outlet temperatures are 650 °C and 750 °C, respectively. The pump provides a flow rate of about 0.28 m^3/s to maintain the temperature rise in the core. Each heat exchanger has the capability of extracting 187 MW during normal operation. The MSFR design includes an intermediate circuit that is used to separate the radioactive fuel salt from the energy conversion system that uses FLiNaK as a coolant with a temperature of 550 °C. Table 4.1 provides the main thermal properties of fuel salt in the MSFR core from reference [72].

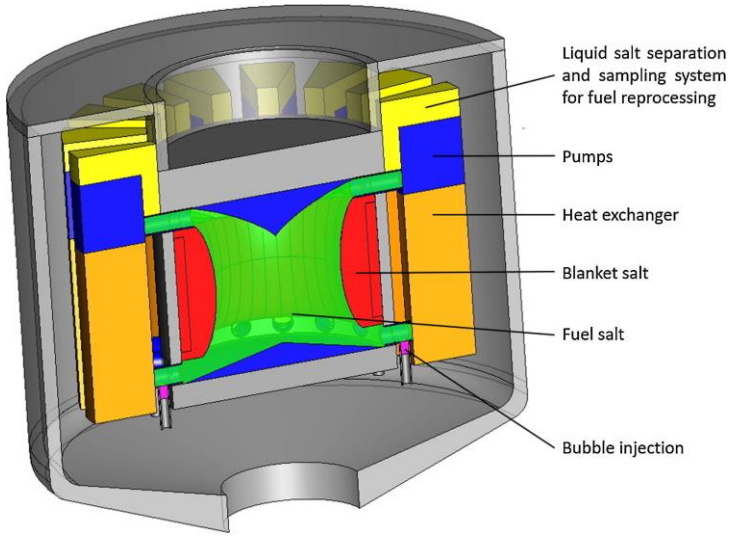


Figure 4.1. Schematic representation of the Molten Salt Fast Reactor [8].

Table 4.1. Characteristics of Molten Salt Fast Reactor.

Thermal/Electric Power	3,000 MWth/1,300 MWe
Fuel Composition	LiF-ThF_4-$^{233}UF_4$, LiF-ThF_4-$(TRU)F_3$
Fuel Inlet/Outlet Temperature	650 ºC/750 ºC
Core Height/Core Radius	2.255 m/1.1275 m
Fuel Salt Volume	18 m^3
Total Fuel Salt Transit Time	4.0 s
Flow Rate	4.5 m^3/s
Density [kg/m^3]	$\rho = 4094 - 0.882 \times (T - 1008)$
Kinematic Viscosity [m^2/s]	$\nu = 5.54 \times 10^{-8} e^{3689/T}$
Dynamic Viscosity [Pa·s]	$\mu = \left[2.268 - 4.886 \times 10^{-4} (T[\mathrm{K}] - 1008)\right] \times 10^{-4} e^{3689/T}$
Thermal Conductivity [W/m·K]	$k = 0.928 + 8.397 \times 10^{-5} T$
Specific Heat [J/kg·K]	$c_p = -1111 + 2.78T$

*T is the temperature in K.

4.2 Comparison to ANSYS CFX Results for Steady-State Problems

The coupled calculation results of PROTEUS-NODAL and SAM were compared with those of the manually coupled calculation of PROTEUS-NODAL and CFX. For consistent comparison, the outer loop was not included in both 1-D and Multi-D SAM models. The inlet velocity and temperature and outlet pressure were given as boundary conditions in all the calculations. In the 1-D SAM calculation, the core was modeled with six parallel 1-D channels, neglecting the radial crossflow of the fuel salt. On the other hand, in Multi-D SAM and CFX models, the core was modeled in R-Z geometry, so the axial and radial velocity fields are considered. Prandtl's mixing length model [69] and the k-ε model [71] were used in Multi-D SAM and CFX, respectively. The meshes utilized in the Multi-D and CFX calculations are shown in Fig. 4.2.

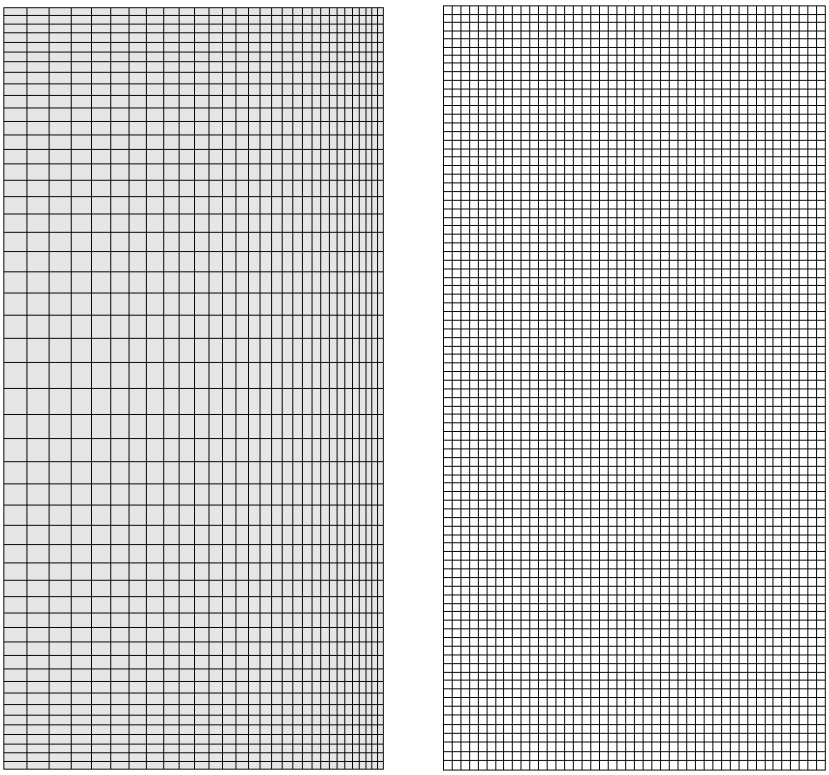


Figure 4.2. Meshes utilized in Multi-D SAM (left) and CFX (right) calculations.

The region-dependent multigroup cross sections were generated using the MC^2-3 code [73] with the ENDF/B-VII.0 data [74] in 9 and 33 group structures. Self-shielded 2082-group cross sections were prepared for each composition and collapsed into 9 and 33 groups using the region-wise spectra obtained from a 2082-group whole-core transport calculation in R-Z geometry. In the steady state calculation, a 33-group cross section was used. While in the transient calculations, the 9-group cross section was used to reduce the computational time without a significant loss of solution accuracy. The upper energy boundaries for the 33-group structure and 9 group structure are listed in Table 4.2 and Table 4.3, respectively. The detailed cross section generation process was described in the reference [56]. For the PROTEUS-NODAL calculations, the P_1 solver in R-Z geometry was used in all calculations in this section. The active core was divided into twenty axial regions and six radial rings. The simplified R-Z geometry of the MSFR used in PROTEUS-NODAL is shown in Fig. 4.3.

Table 4.2. Upper Energy Boundaries of 33-Group Structure.

Group	Energy (eV)	Group	Energy (eV)	Group	Energy (eV)	Group	Energy (eV)
1	1.419E+07	10	1.832E+05	19	2.035E+03	28	2.260E+01
2	1.000E+07	11	1.111E+05	20	1.234E+03	29	1.371E+01
3	6.065E+06	12	6.738E+04	21	7.485E+02	30	8.315E+00
4	3.679E+06	13	4.087E+04	22	4.540E+02	31	3.928E+00
5	2.231E+06	14	2.479E+04	23	2.754E+02	32	5.316E-01
6	1.353E+06	15	1.503E+04	24	1.670E+02	33	4.175E-01
7	8.209E+05	16	9.119E+03	25	1.013E+02		
8	4.979E+05	17	5.531E+03	26	6.144E+01		
9	3.020E+05	18	3.355E+03	27	3.727E+01		

Table 4.3. Upper Energy Boundaries of 9-Group Structure.

Group	Energy (eV)	Group	Energy (eV)	Group	Energy (eV)	Group	Energy (eV)
1	1.419E+07	4	1.832E+05	6	9.119E+03	8	4.540E+02
2	2.231E+06	5	4.087E+04	7	2.035E+03	9	5.044E+00
3	8.209E+05						

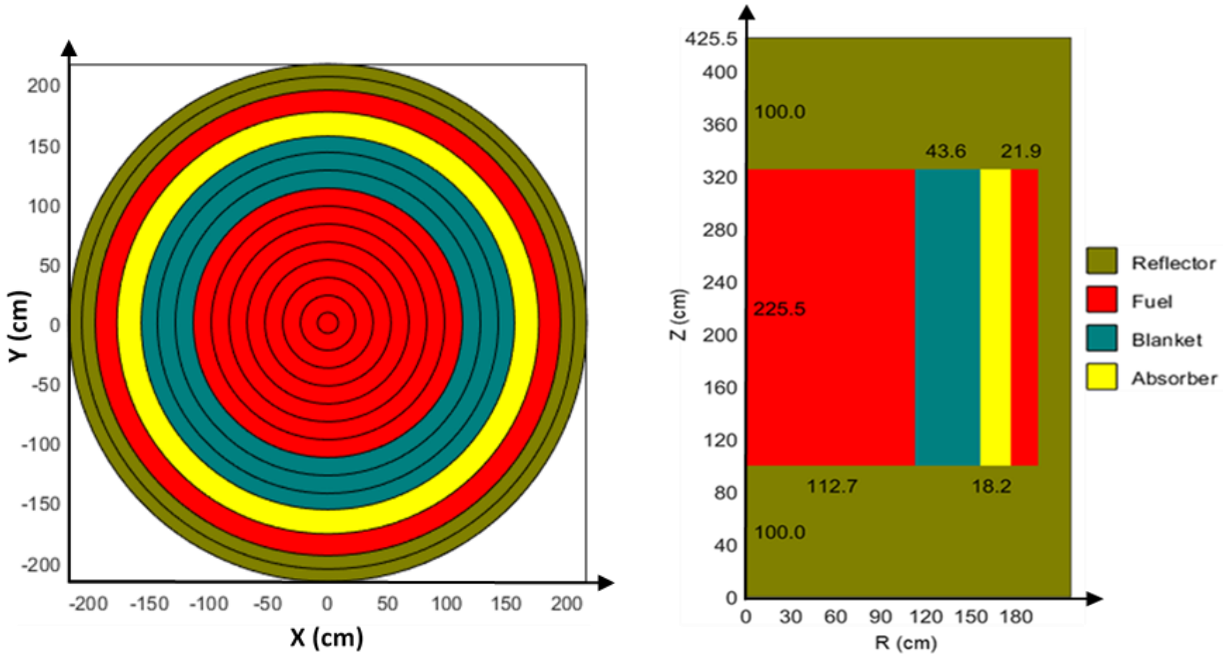


Figure 4.3. Planar (left) and axial (right) views of the MSFR model in R-Z geometry.

In the manually coupled calculations with CFX, the power densities of two successive Picard iterations were used to determine the convergence with a tolerance limit of 10^{-4}. Three iterations were needed for convergence. The initial power distribution was obtained from the coupled calculation of PROTEUS-NODAL and Multi-D SAM. The power density in each CFX mesh was evaluated from the node average power density of PROTEUS-NODAL with the built-in interpolation function of CFX. Using this power distribution, the CFD simulation was performed to determine the flow fields of the fuel salt. Despite the different thermal-hydraulics models, the resulting temperature and density fields are similar. Thus, the multiplication factors of the three coupled calculations agreed very well due to similar thermal feedback. The multiplication factor was 0.98117 for CFX, 0.98110 for Multi-D SAM, and 0.98115 for 1-D SAM.

Figure 4.4 shows the converged axial velocity, radial velocity, and temperature fields obtained from the coupled calculation of PROTEUS-NODAL and CFX. Figure 4.5 shows the

results obtained from the coupled calculation of PROTEUS-NODAL and Multi-D SAM. The velocity and temperature fields from Multi-D SAM match well with those from CFX. To compare the axial velocities from Multi-D SAM and CFX with those from 1-D SAM, channel-wise average axial velocities were calculated for the Multi-D SAM and CFX results. The first channel was at the core center, and the sixth channel was at the core periphery. Figures 4.6 and 4.7 compare the channel-wise axial velocity profiles of Multi-D SAM and 1-D SAM with those of CFX. The difference in the axial velocity fields between Multi-D SAM and CFX was mainly due to the different turbulence models. As mentioned before, the two-equation k-ε model was used in the CFX calculation. On the other hand, the zero-equation Prandtl's mixing length model is used in Multi-D SAM uses with a user-specified mixing length [69]. In this calculation, the mixing length was simply estimated by

$$L_{mix} = (V_D^{1/3}) / 7 , \tag{4.1}$$

where V_D is the fluid domain volume [71]. An improved mixing length based on experiment data or higher fidelity reference solutions would improve the solution, but no attempt was made to refine the mixing length. The axial velocity fields from 1-D SAM and CFX were quite different due to neglecting the radial velocity field in the 1-D SAM calculation. This observed difference in velocity fields affects the power distribution. As shown in Fig. 4.8, the relative difference in power distribution of the coupled calculation with Multi-D SAM from the coupled calculation with CFX is within ±0.07%, while that of the coupled calculation with 1-D SAM is within ±0.4%.

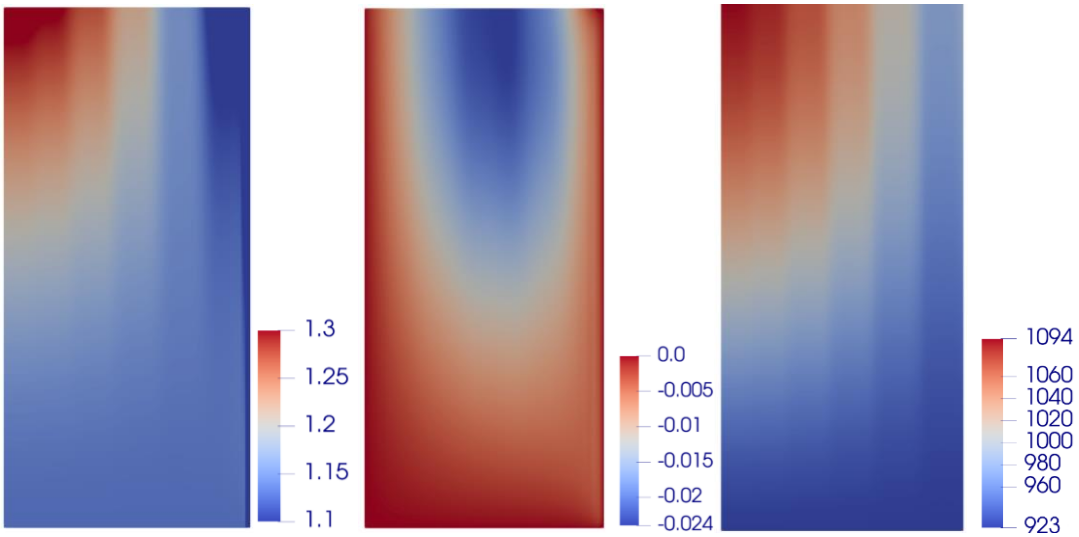


Figure 4.4. Axial velocity (left), radial velocity (middle), and temperature (right) fields of fuel salt obtained from CFX. The cylinder axis is on the left edge of the figures.

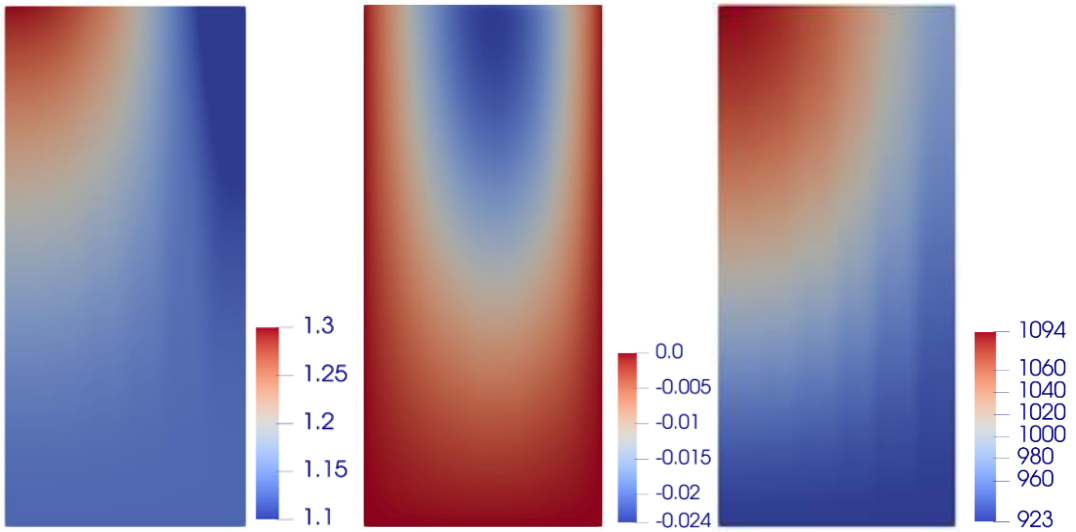


Figure 4.5. Axial velocity (left), radial velocity (middle), and temperature (right) fields of fuel salt obtained from Multi-D SAM. The cylinder axis is on the left edge of the figures.

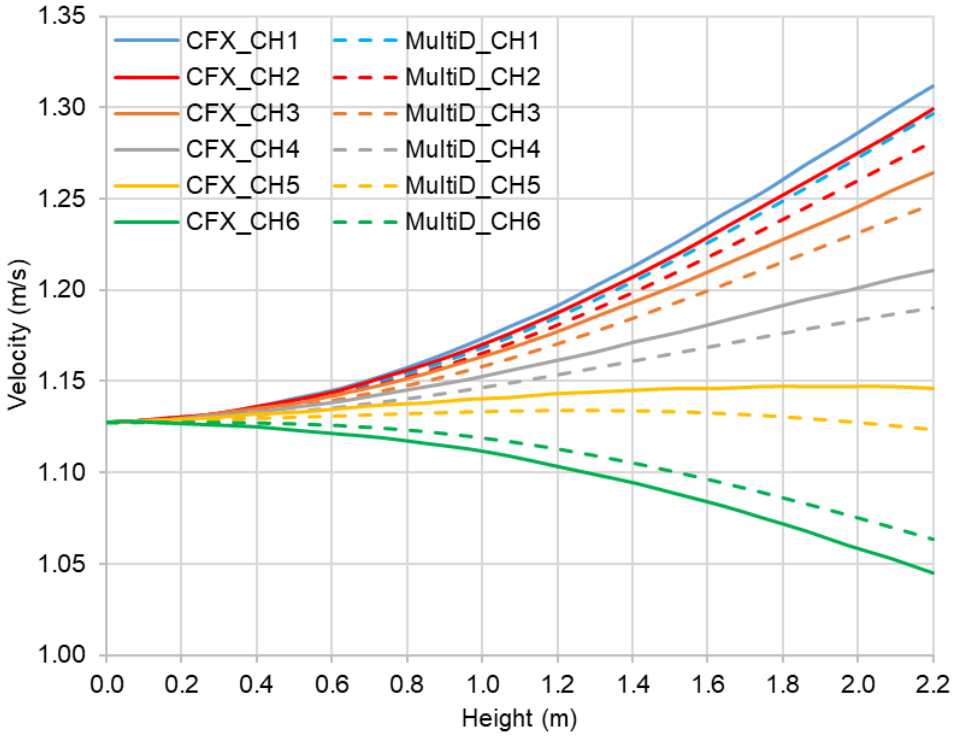


Figure 4.6. Comparison of axial velocity profiles of Multi-D SAM and CFX.

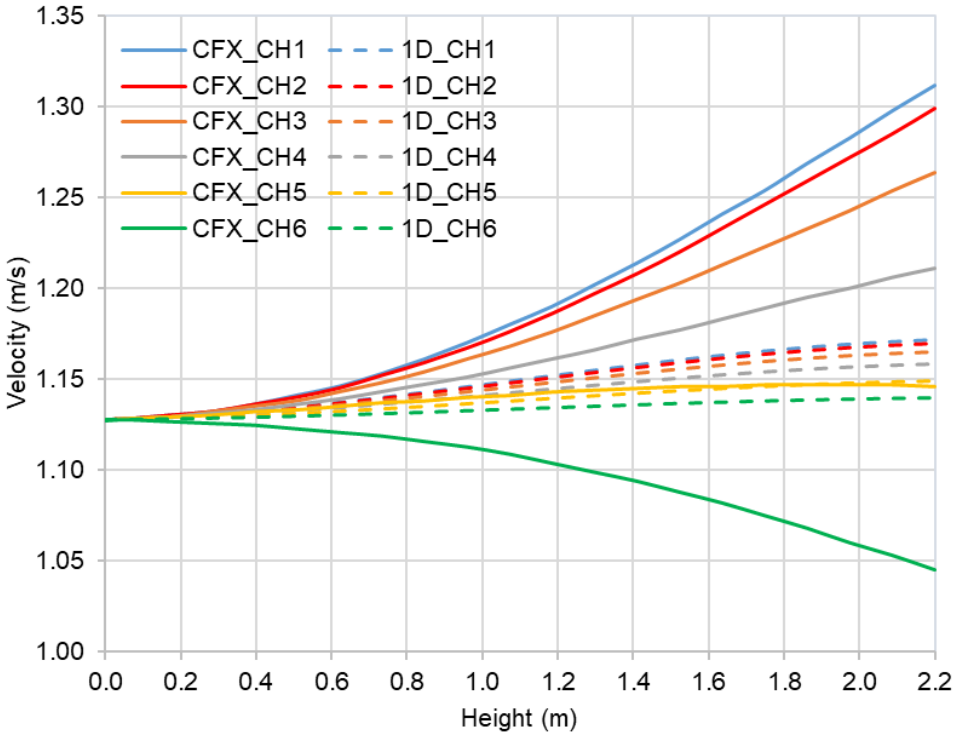


Figure 4.7. Comparison of axial velocity profiles of 1-D SAM and CFX.

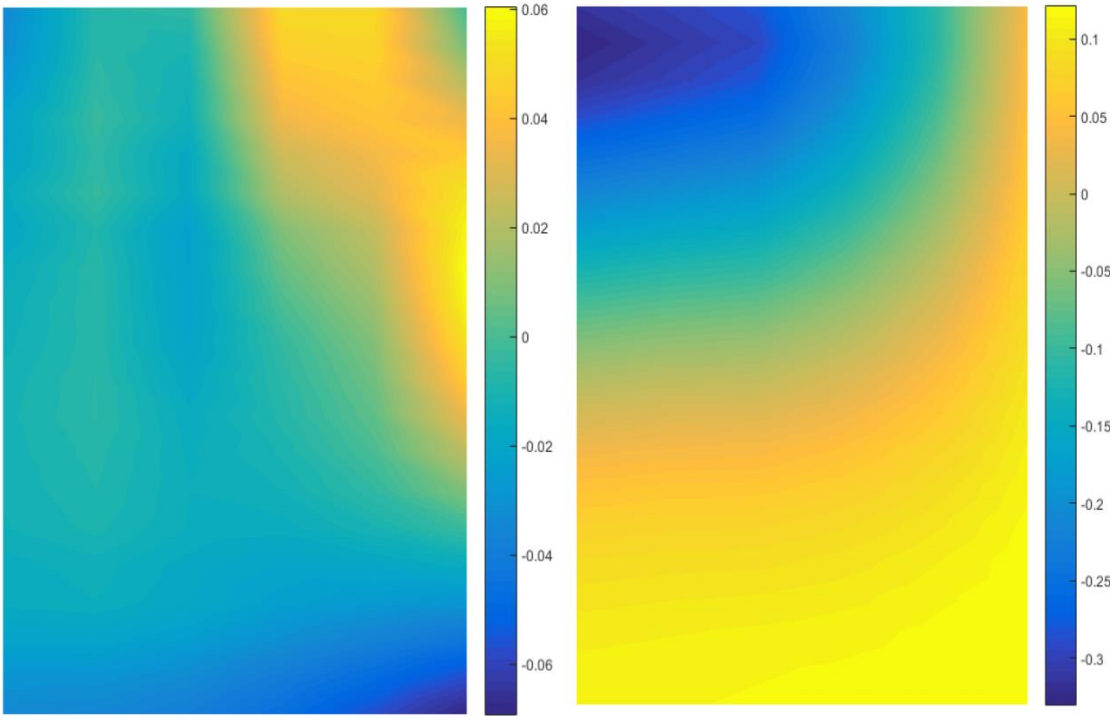


Figure 4.8. Relative deviation (%) in power density of coupled calculation with Multi-D SAM (left) and 1-D SAM (right) from that with CFX.

4.3 Verification Tests for Transient Problems

Three transient scenarios of the MSFR benchmark problem were analyzed with the coupled system of PROTEUS-NODAL and 1-D SAM as well as the coupled system of PROTEUS-NODAL and Multi-D SAM: unprotected transient over-power (UTOP), unprotected loss of flow (ULOF), and unprotected loss of heat sink (ULOHS) scenarios. The results were compared to two open literature solutions of other organizations obtained with different code systems. One is the solution of the coupled calculation of the nodal neutronics code PARCS and the system analysis code TRACE conducted at the Paul Scherrer Institute (PSI) [17]. The other is the solution of the coupled calculation with the neutronics code DALTON and the CFD code HEAT conducted at the Delft University of Technology [11].

The developed thermal-hydraulics models of the MSFR using 1-D SAM and Multi-D SAM (the outer loop is modeled with 1-D SAM) are shown in Fig. 4.9 and Fig. 4.10. To have a more realistic heat exchanger design, a printed circuit heat exchanger (PCHE) was adopted from [75]. The same data of the thermos-physical properties of the fuel salt used in the steady-state calculations were also used for the transient calculations.

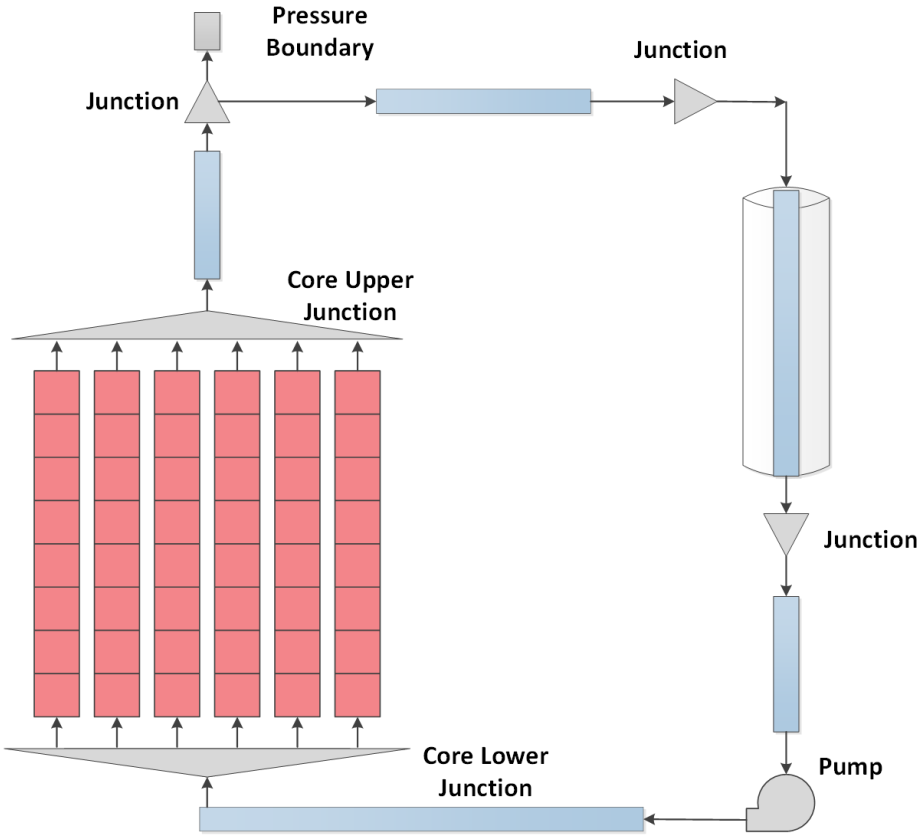


Figure 4.9. 1-D SAM model of MSFR benchmark problem.

The UTOP transient was simulated by inserting a 50 pcm step reactivity at the beginning of the transient. This reactivity insertion was achieved by increasing the mole fraction of U-233 in the fuel salt from 2.515% to 2.517%, which in total added 2.33 kg of U-233 to the core. For this slight change, the thermos-physical properties of fuel salt remain the same as in Table 4.1. Figure

4.11 compares the power evolutions obtained from PROTEUS-NODAL and Multi-D SAM, PROTEUS-NODAL and 1-D SAM, and the calculation performed at TUDelft. In the results from

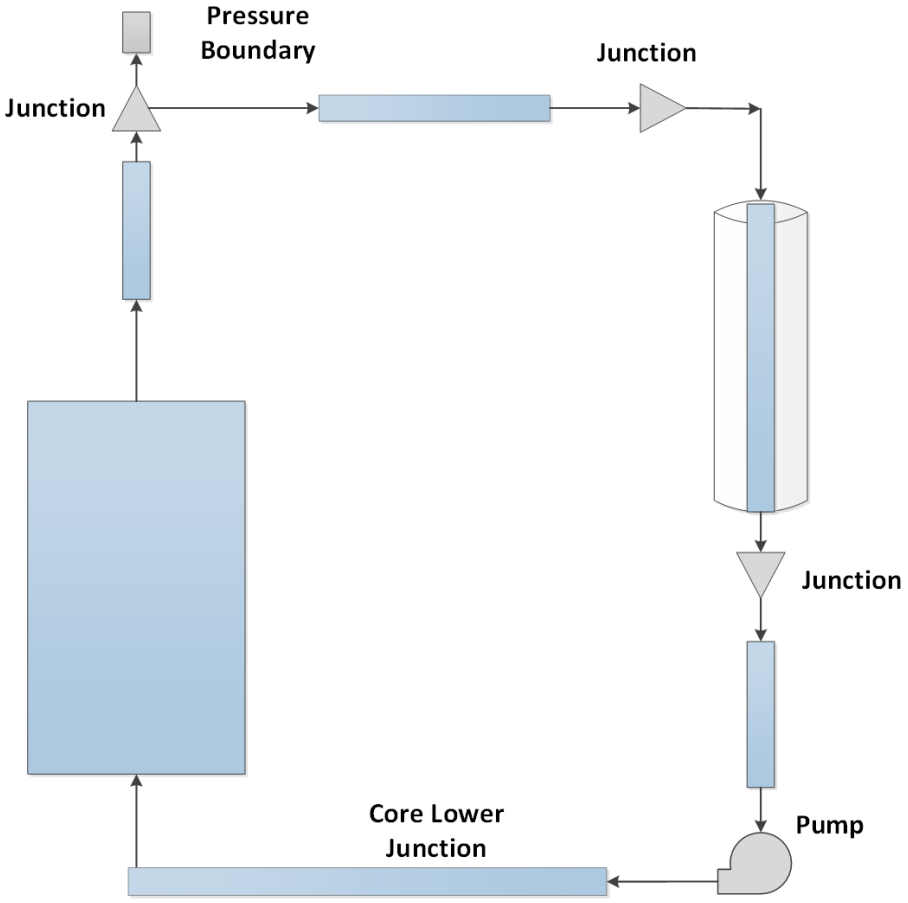


Figure 4.10. Multi-D SAM model of MSFR benchmark problem.

from PROTEUS-NODAL and SAM, the power increases at the beginning of the transient and reaches a maximum value of about 156% of the nominal power at 5.0 ms. The increased core temperature introduces negative reactivity feedback due to the Doppler effect and the reduced fuel salt density. Thus, the power decreases after 5.0 ms. It can be seen that the power obtained from PROTEUS-NODAL and Multi-D SAM agrees well with that obtained from PROTEUS-NODAL and 1-D SAM. The peak power predicted by PROTEUS-NODAL is slightly lower than the TUDelft result. This can be attributed to the different temperature feedback coefficients between

PROTEUS-NODAL (-7.68 pcm/K [56]) and TUDelft (-6.79 pcm/K [8]) due to the use of different multigroup cross section libraries.

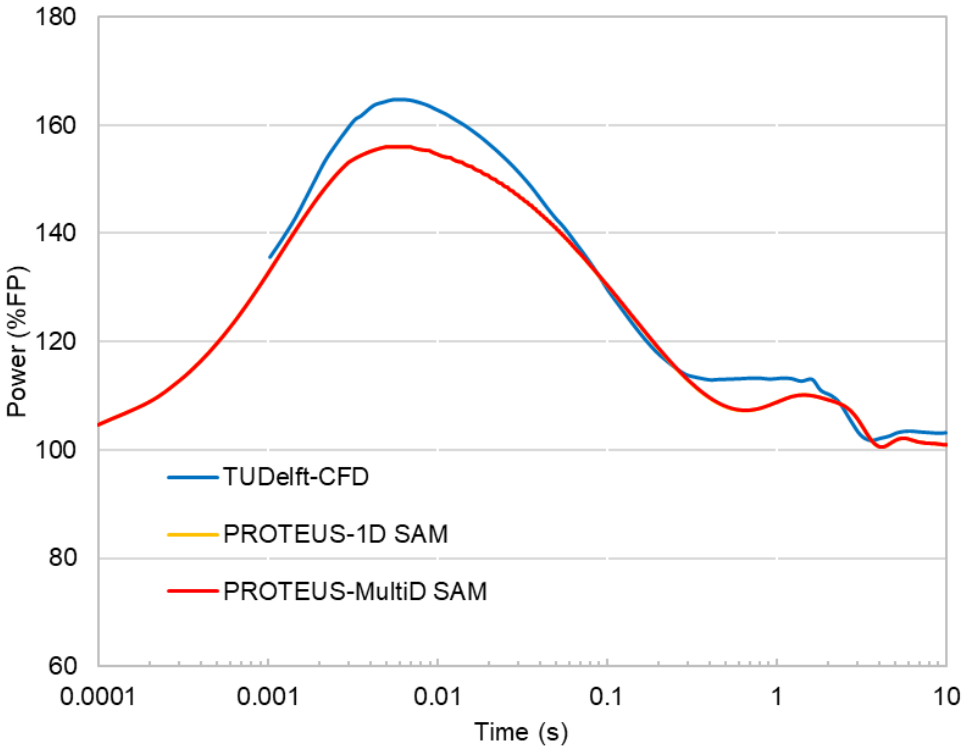


Figure 4.11. Power evolution during UTOP transient.

The ULOF transient is initiated by pump failure. The primary pump head is decreased exponentially with a time constant of 5.0 s. Figure 4.12 compares the power evolutions obtained from PROTEUS-NODAL and Multi-D SAM, PROTEUS-NODAL and 1-D SAM, PARCS-TRACE, and TUDelft calculation with CFD. The decreased pump head causes the decrease of flow rate in the primary loop. The decreased flow velocity reduces the number of delayed neutrons lost in the outer loop and thus introduces a positive reactivity. On the other hand, the reduced flow rate increases the core average temperature and thus induces negative feedback from the Doppler effect and the reduced fuel salt density. The negative feedback is larger than the positive feedback and thus the power decreases. The results of PROTEUS-NODAL and Multi-D SAM as well as the

results from PROTEUS-NODAL and 1-D SAM agree well with the TUDelft-CFD result. The power decreases monotonically and reaches about 18% of the nominal full power at 30.0 s in the TUDelft calculation and the coupled calculation of PROTEUS-NODAL and 1-D SAM. After 30.0 s, the power of these two calculations remains at about 18% of the nominal full power due to the natural circulation buildup. The power obtained from PROTEUS-NODAL and Multi-D SAM remains at about 21% of the nominal full power. On the other hand, the PARCS-TRACE solution decreases more rapidly without reaching an asymptotic power level since the inlet fuel salt velocity instead of the pump head was set to decrease exponentially with a time constant of 5.0 s, which leads to a more rapid decrease of the average inlet velocity and no natural circulation buildup.

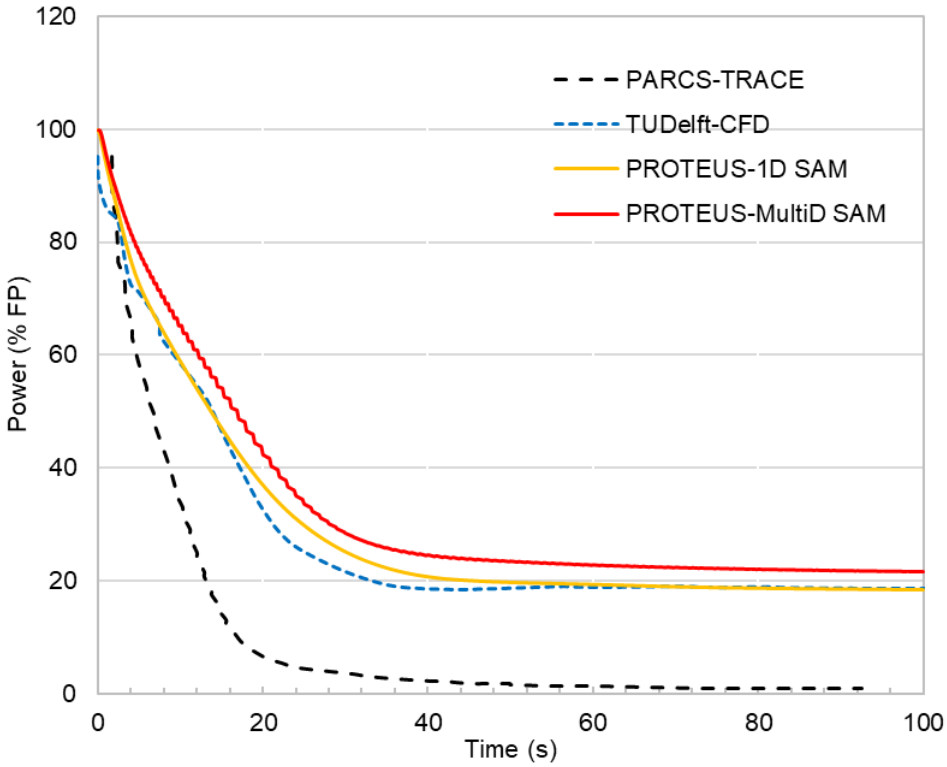


Figure 4.12. Power evolution during ULOF transient.

Figure 4.13 compares the inlet velocities obtained from PROTEUS-NODAL and Multi-D SAM, and PROTEUS-NODAL and 1-D SAM. The natural circulation flow rate from Multi-D

SAM is about 9% of the nominal value. On the other hand, the natural circulation flow rate from 1-D SAM is about 6.5% of the nominal value, which is closer to the TUDelft CFD calculation result (5.6% of the nominal flow rate). Thus, the power from PROTEUS-NODAL and 1-D SAM matches better the TUDelft solution after 30.0 s. The difference in the natural circulation flow rate between Multi-D SAM and 1-D SAM is mainly due to the difference in the pressure drop calculation model. In 1-D SAM, the pressure drop across the core is calculated with wall friction models. The wall friction factors for the turbulent regime are determined using the McAdams correlation [69]. In Multi-D SAM, the pressure field in the core is determined by solving the multi-D mass, momentum, and energy equations. However, Prandtl's mixing length turbulence model used to calculate the turbulent viscosity and a single mixing length estimated with Eq. (4.1) do not represent the turbulence effects accurately in this natural circulation condition. The resulting pressure drop from Multi-D SAM deviates more from the CFD result than that determined with the wall friction model.

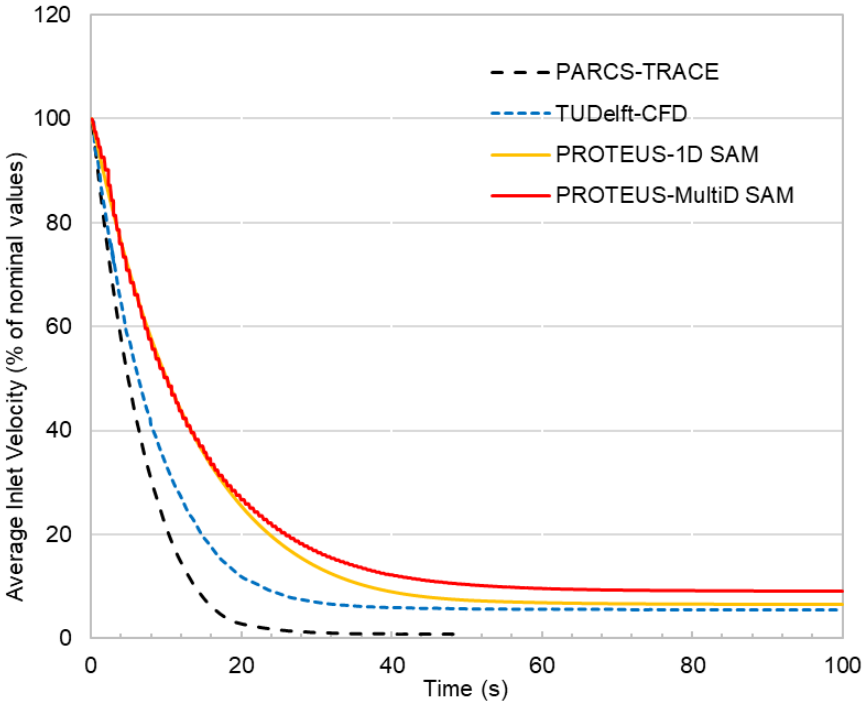


Figure 4.13. Average inlet velocity evolution during ULOF.

The ULOHS transient is simulated in PROTEUS-NODAL and SAM calculations by the exponential decrease of the inlet flow rate of the secondary side in the heat exchanger with a time constant of 1.0 s. The loss of cooling capabilities of the intermediate heat exchangers leads to the increase of the fuel salt temperature at the core inlet, which causes the increase of the core-averaged fuel temperature. This results in negative feedback from the Doppler effect and the reduced fuel salt density. Figure 4.14 compares the power evolution during ULOHS from when the uncooled fuel salt flows into the core inlet. Coupled PROTEUS and SAM calculations yield a similar power reduction as PARCS-TRACE and TUDelft solutions although the time evolution of power is different. The difference in power evolution is mainly due to the different models used for the loss of heat sink. In PARCS-TRACE and TUDelft-CFD calculations, the heat removal rate of the heat exchanger was exponentially reduced with a time constant of 1.0 s while the secondary flow rate was reduced in SAM models. The exponential decay of the heat removal rate yields more rapid decreases in power than the exponential decay of the flow rate.

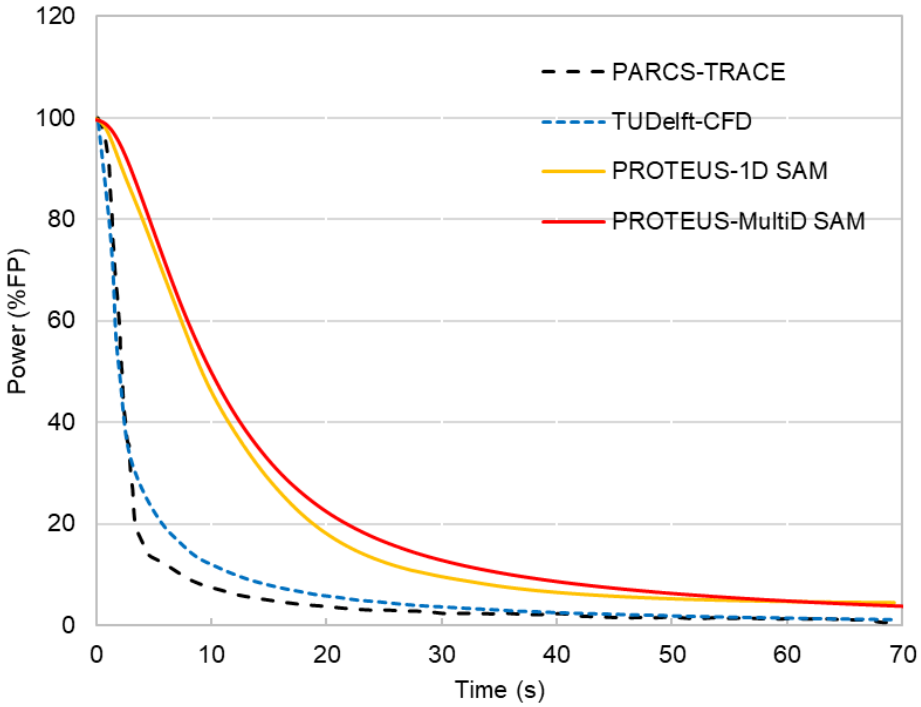


Figure 4.14. Power evolution during ULOHS.

Table 4.4 compares the computational times of PROTEUS-NODAL and 1-D SAM vs. PROTEUS-NODAL and Multi-D SAM calculations for steady-state and three transient calculations of MSFR. All the calculations were performed serially on a Linux Workstation with the Intel Xeon CPU X5690, which has a 3.47 GHz frequency. Compared to 1-D SAM, Multi-D SAM takes 31 times more for the steady state problem and 6 to 13 times more for transient problems.

Table 4.4. Computational Times (s) for MSFR Verification Tests.

Test Problem	Steady State	UTOP	ULOF	ULOHS
PROTEUS/1-D SAM	13	892	2005	2161
PROTEUS/Multi-D SAM	402	7688	26819	13674

4.4 Summary

The coupled PROTEUS-NODAL and SAM code system for MSR applications were verified using the MSFR benchmark in this chapter. For the steady state verification tests, the results of PROTEUS-NODAL and Multi-D SAM and the results of PROTEUS-NODAL and 1-D SAM were compared with those of PROTEUS-NODAL and the commercial CFD software ANSYS CFX. The power distributions from those three calculations agreed well with each other. The velocity and temperature fields matched well between the Multi-D SAM and CFX solutions. However, the axial velocity field of 1-D SAM was quite different from that of CFX due to the neglected lateral flow. In addition, the UTOP, ULOF, and ULOHS transient scenarios were analyzed with the coupled code system. The results were compared with solutions obtained from the PARCS-TRACE calculation and the coupled calculation of a diffusion theory based neutronics code and a CFD code performed at TUDelft. In general, the power evolutions of the coupled calculations of PROTEUS-NODAL and SAM agreed well with those solutions.

Chapter 5 Validation of Coupled PROTEUS-NODAL and SAM Code System with MSRE Experiments

This Chapter presents the validation results of the coupled PROTEUS-NODAL and SAM code system with experimental data of the MSRE problem available in the design and operation reports of ORNL. First, the MSRE problem is briefly described, and the developed computational models of PROTEUS-NODAL and 1-D SAM are discussed. Then, validation test results of the coupled code system are presented and compared with the experimental data for the protected pump start-up and coast-down at zero power, and the natural convection test of MSRE.

5.1 Description of MSRE

MSRE is a thermal spectrum MSR with flowing fuel. The fuel salt flows through channels made of solid graphite moderator. It was designed to be a 10 MWth reactor but was discovered in the final stages that the heat extraction in the secondary system was smaller than expected and the maximum power level was restricted to 8.0 MWth as measured from heat balances. The MSRE fuel was composed of UF_4 in the carrier salt of LiF-BeF_2-ZrF_4 [76]. In the beginning, it was fuel with ^{235}U with 33% enriched. In 1968, the fuel was replaced with 91% enriched ^{233}U. The isotropic concentrations of the two MSRE fuel salts are given in Table 5.1.

The fuel salt was contained in pipes and vessel that were made of nickel-alloy for resistance of corrosion by molten salt, especially in high temperature environments. The MSRE reactor vessel has an inner diameter of 147.32 cm with a wall thickness of 2.54 cm. The core container is inside the vessel and has an inner diameter of 140.97 cm and a thickness of 0.635 cm. Figure 5.1 and 5.2

shows a schematic representation of the MSRE reactor vessel and the primary and secondary system of the MSRE, respectively.

Table 5.1. Molar Composition of Fuel Salts.

	^{235}U Core	^{233}U Core
Molar composition	$LiF-BeF_2-ZrF_4-UF_4$ (65.0%-29.17%-5.0%-0.83%)	$LiF-BeF_2-ZrF_4-UF_4$ (64.5%-30.18%-5.19%-0.13%)
Enrichment	33%	91.5%
Isotope	Atom Fraction (%)	Atom Fraction (%)
Li	2.62E-01	2.62E-01
Be	1.19E-01	1.23E-01
Zr	2.06E-02	2.11E-02
F	5.95E-01	5.94E-01
^{233}U		4.98E-04
^{234}U		3.12E-05
^{235}U	1.09E-03	3.78E-06
^{238}U	2.22E-03	1.07E-06

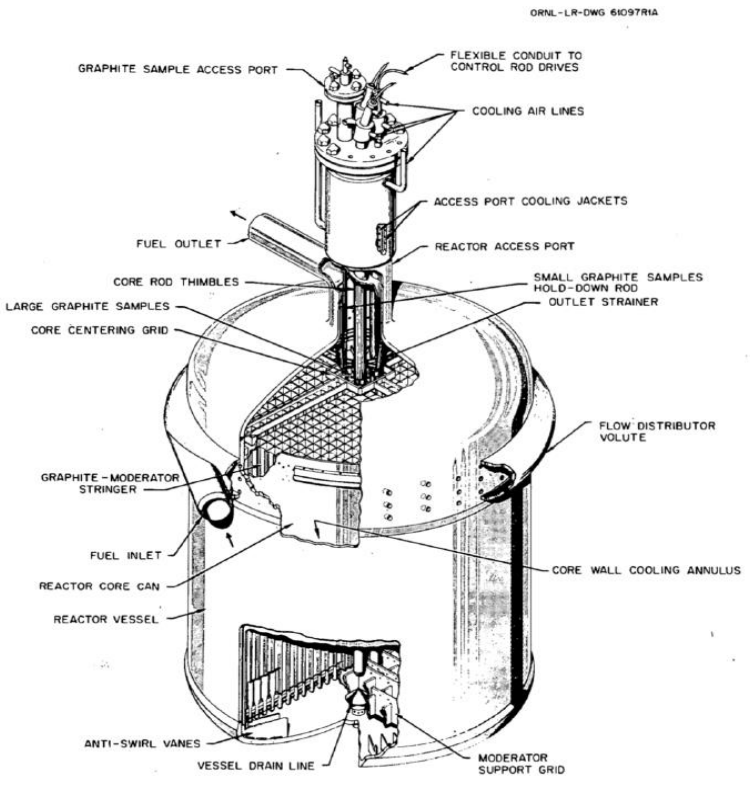


Figure 5.1. Schematic diagram of MSRE reactor vessel [7].

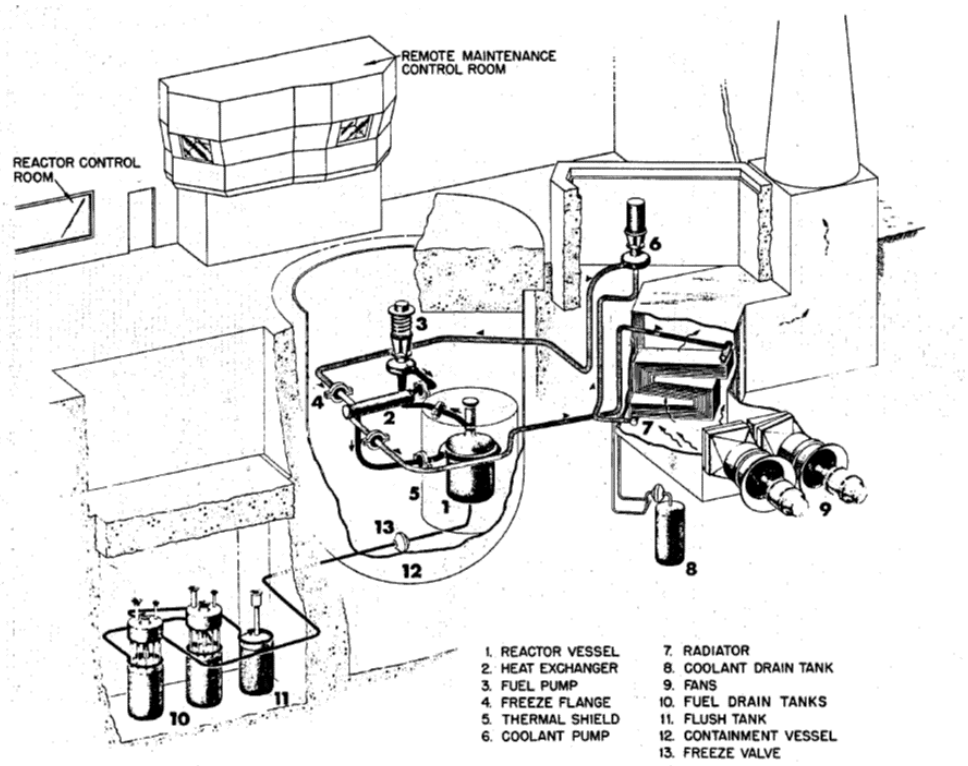


Figure 5.2 Layout of MSRE primary and secondary systems [7].

The heated fuel salt from the core outlet was cooled through a shell-and-tube heat exchanger and recirculated by a centrifugal pump [77]. In the heat exchanger, primary fuel salt flows through the shell side and secondary coolant salt flows through the tube side. The coolant salt for the secondary was molten LiF-BeF_2 salt. The heat from the primary loop was removed to the secondary loop through the heat exchanger and then to the atmosphere through a radiator. The MSRE core consists of 513 graphite stringers with 1140 fuel channels [7]. Figure 5.3 shows the configuration of the MSRE core and fuel channels. There are three control rods made from gadolinium in the MSRE core. Each control rod consists of 38 elements and the height of the element is 3.96748 cm. Figure 5.4 shows the lattice arrangement of control rods and element geometry. Table 5.2 summarizes the main characteristics of the MSRE core and the thermo-physical properties for the fuel salt and graphite as obtained from [77] and [78].

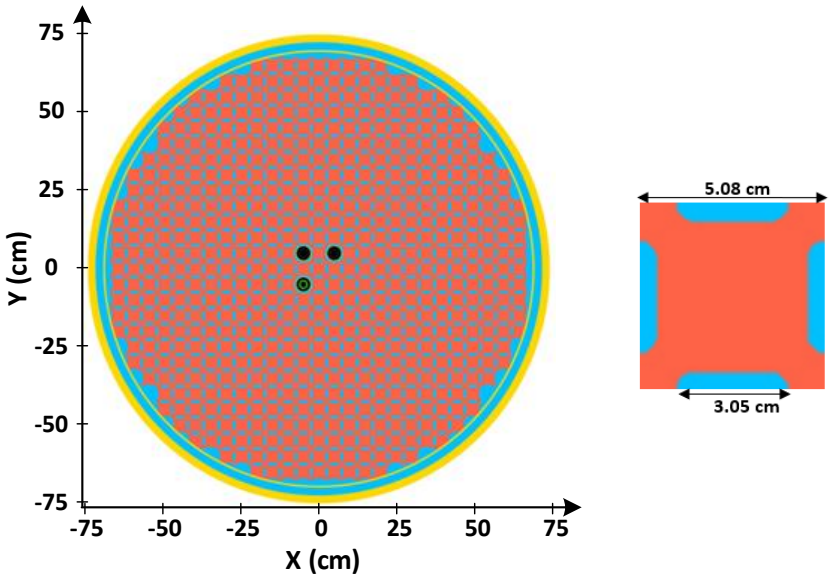


Figure 5.3. Radial layout of MSRE core (left) and lattice arrangement of fuel channel (right).

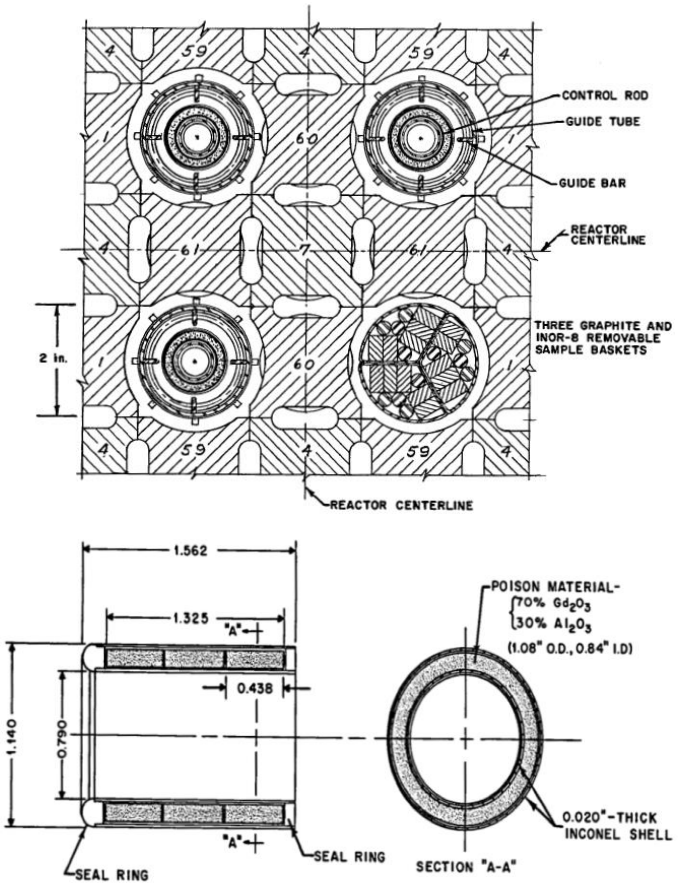


Figure 5.4. Lattice arrangement of control rods (up) geometry and composition of the control rod element (bottom) (units in inch) [78].

Table 5.2. Main Characteristics of Molten Salt Reactor Experiment.

Thermal Power	8 MWth
Fuel Composition	$LiF\text{-}BeF_2\text{-}ZrF_4\text{-}UF_4$ ^{235}U Core (65.0%-29.17%-5.0%-0.83%) ^{233}U Core (64.5%-30.18%-5.19%-0.13%)
Fuel Inlet/Outlet Temperature	908 K/936 K
Core Height/Core Radius	1.66 m/0.762 m
Total Fuel Salt Transit Time	25.2 s
Fuel Salt Density [kg/m^3]	$\rho = 2322.7 - 0.502 \times (T[K] - 922)$
Fuel Salt Dynamic Viscosity [Pa·s]	$\mu = 0.00785$
Fuel Salt Thermal Conductivity [W/m·K]	$k = 1.44$
Fuel Salt Specific Heat [J/kg·K]	$c_p = 1967.8$
Graphite Density [kg/m^3]	$\rho_g = 1874.16$
Graphite Thermal Conductivity [W/m·K]	$k_g = 39.8$
Graphite Specific Heat [J/kg·K]	$c_{p,g} = 1758.5$

5.2 Computational Models

The PROTEUS-NODAL model for the MSRE was developed in R-θ-Z geometries considering only the regions in the reactor vessel. The region-dependent multigroup cross sections were generated with the Monte Carlo code OpenMC [48] with the ENDF/B-VII.1 data [79] in a 16-group structure. The upper energy boundaries for the 16-group neutron energy structure are listed in Table 5.3. The control rods and the core outside regions (i.e., gap, insulator, and thermal shield) were modeled explicitly in the OpenMC model to yield an accurate solution. As shown in Fig. 5.5, this model was divided into several radial and axial regions for the region-dependent cross sections tally. The fraction of the heat generated in the graphite moderator of MSRE was also determined to be 5.5% from a coupled neutron and gamma transport calculation with OpenMC. A detailed description of the cross section generation process for MSRE was given in [80].

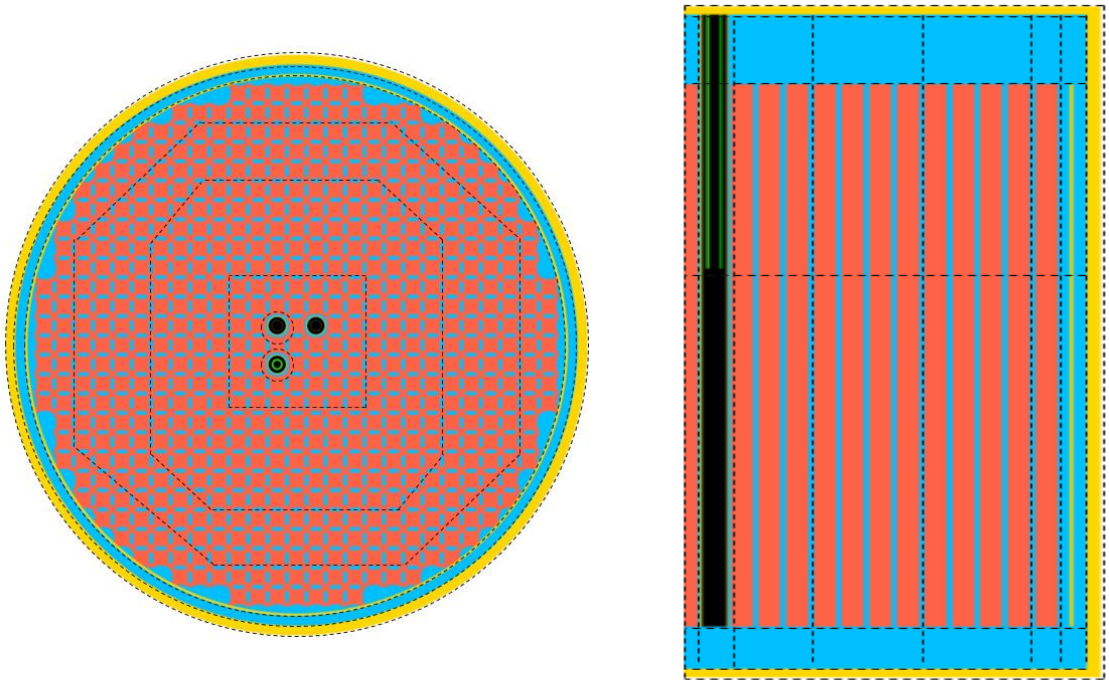


Figure 5.5 Radial (left) and axial (right) configurations of cross section tally regions [80].

Table 5.3. Upper Energy Boundaries of 16-Group Structure.

Group	Energy (eV)	Group	Energy (eV)	Group	Energy (eV)	Group	Energy (eV)
1	2.000E+07	5	6.734E+04	9	1.300E+00	13	1.800E-01
2	3.679E+06	6	9.118E+03	10	6.250E-01	14	1.400E-01
3	1.353E+06	7	1.487E+02	11	4.000E-01	15	8.000E-02
4	5.000E+05	8	4.000E+00	12	2.500E-01	16	4.200E-02

Due to the limitation of the PROTEUS-NODAL, the air gap between the reactor vessel and the thermal field cannot be modeled explicitly. Figure 5.6 shows the R-θ-Z geometry model of the MSRE core in PROTEUS-NODAL. The PROTEUS-NODEL model only consists of the regions inside the reactor vessel. However, there is a large fraction of neutrons leaking out of the reactor vessel. To account for the effect of regions beyond the reactor vessel on thermalizing and reflecting neutrons leaked from the reactor vessel, multigroup albedo boundary conditions were applied for

the outer surfaces of the reactor vessel [57]. The multigroup albedo boundary with the albedo response matrix in PROTEUS-NODAL is defined as

$$\begin{bmatrix} J_1^- \\ \vdots \\ J_g^- \\ \vdots \\ J_G^- \end{bmatrix} = \begin{bmatrix} \beta_{11} & \cdots & \beta_{g1} & \cdots & \beta_{G1} \\ \vdots & \ddots & \vdots & & \vdots \\ \beta_{1g} & & \beta_{gg} & & \beta_{Gg} \\ \vdots & & \vdots & \ddots & \vdots \\ \beta_{1G} & \cdots & \beta_{gG} & \cdots & \beta_{GG} \end{bmatrix} \begin{bmatrix} J_1^+ \\ \vdots \\ J_g^+ \\ \vdots \\ J_G^+ \end{bmatrix} \tag{5.1}$$

where J_g^- is the incoming partial currents, J_g^+ is the outgoing partial currents, $\beta_{gg'}$ is the element of the albedo response matrix depending on the composition and the geometry of the outer region. The albedo matrix was generated from 2-D OpenMC calculations, as described in [57]. With the multigroup albedo boundary, the multiplication factors from PROTEUS-NODAL match well with the OpenMC results. The multiplication factor for ^{235}U core is 1.04818 from PROTEUS-NODAL, which is 8.3 pcm lower than that from the OpenMC. The multiplication factor for ^{233}U core is 1.07208 from PROTEUS-NODAL, which is 104.6 pcm higher than that from the OpenMC.

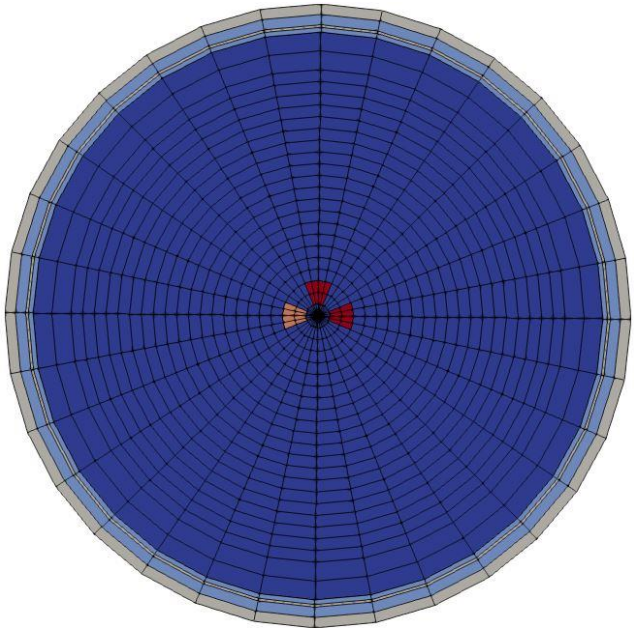


Figure 5.6. PROTEUS-NODAL models of MSRE core in R-θ-Z geometries.

The thermal-hydraulics model of the primary loop of the MSRE was developed with 1-D SAM as shown in Fig. 5.7. The core was divided into twelve 1-D vertical channels and each channel was divided into twenty axial nodes. The temperatures of solid graphite and fuel salt were solved together with the conjugate heat transfer capability in SAM. The heat exchanger and the pump were connected by pipes. The secondary side of the heat exchanger was simply represented through a given flow rate and temperature boundary in the SAM model. The design parameters for each component were obtained from [81]. The hydraulic diameter for each coolant channel in the core is 0.0159 m and the cross-sectional area of pipe in the primary system is 0.0127 m^2 with a hydraulic diameter of 0.127 m. The downcomer is a complicated 3D annulus, but it was simplified into a 1-D pipe with a flow area of 0.116 m^2 in the SAM model. The cross-sectional area of the fuel pump is set to 0.0127 m^2, which is the same as the connecting pipes. The main design parameters used in the SAM model are shown in Table 5.4.

Table 5.4 MSRE Heat Exchanger Parameters in SAM Model.

Primary side area	0.0412 m^2
Secondary side area	0.0279 m^2
Primary side hydraulic diameter	0.0130 m
Secondary side hydraulic diameter	0.0209 m
Primary heat transfer surface area density	308 m^{-1}
Secondary heat transfer surface area density	378 m^{-1}

To obtain accurate fuel and moderator temperature profiles, it is important to use the correct convection heat transfer coefficient between the fuel salt and the solid moderator. The Reynolds number for the fuel flow in the channel is around 1000, which indicates that the fuel flow is in the laminar regime. The conventional theoretical solution of the Nusselt number for the laminar tube flow with uniform heat flux is 4.36 [82]. However, it is assumed that there is no internal heat source in the fluid in the derivation. To derive the Nusselt number with an internal heat source, the

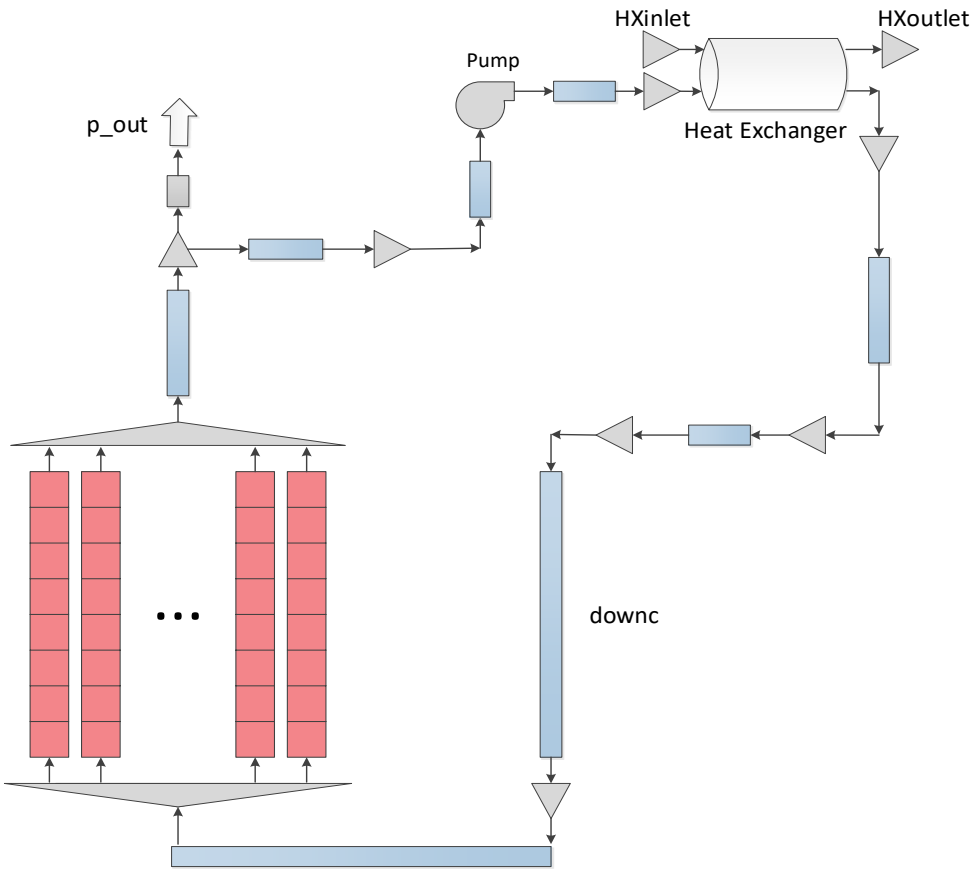


Figure 5.7. Primary Loop Model developed for MSRE using SAM.

Poppendiek effect should be considered as in [83]. The Poppendiek effect states that the fluid temperature near the wall is higher than the average temperature due to the internal heat source. The resulting relations between wall temperature and average temperature for the cylindrical tube are:

$$T_w - T_m = \frac{q''' R^2}{2k}\left(\frac{11F - 8}{24}\right), \tag{5.2}$$

$$F = 1 - \frac{2q''_w}{Rq'''}, \tag{5.3}$$

where T_w and T_m are wall temperature and mean temperature, respectively. q''' is the internal heat source density, R is the tube radius, k is the thermal conductivity, and q''_w is the heat flux through the wall. As a result, the Nusselt number with an internal heat source can be determined as

$$Nu = \frac{hD}{k} = \frac{48(F-1)}{11F-8}. \tag{5.4}$$

Using a value of 5.5% for the fractional heat deposit in the moderator of the total heat generated in the fuel and the moderator, the resulting Nusselt number is 0.767. However, this derivation assumes a fully developed flow. For this MSRE core channel, the hydraulic entrance length L_e and thermal entrance length L_t can be estimated as

$$\begin{aligned} L_e &\approx 0.06\,\mathrm{Re}\,D = 1.25\,m, \\ L_t &\approx 0.05\,\mathrm{Re}\,\mathrm{Pr}\,D = 11.20\,m. \end{aligned} \tag{5.5}$$

Since the length of the core channel is only 1.6637m, it is not appropriate to assume that the flow is fully developed. Therefore, the position-dependent Nusselt number and heat transfer coefficient was developed from separate CFD calculations using the ANSYS CFX code. The mesh used in the calculation was generated with CUBIT [84], as shown in Fig. 5.8. The derived Nusselt number from the CFX solution is shown in Fig. 5.9. The Nusselt number decreases along the axial position from the entrance region as expected. The maximum Nusselt number is 5.89 at the inlet, and the minimum value is 0.83 at the outlet.

Using the coupled system of PROTEUS-NODAL and 1-D SAM, the axial temperature distributions of the fuel salt and the graphite in the hottest channel (~17 cm from the core center) were calculated and compared with the ORNL results calculated with the Poppendiek method [85]. Figures 5.10 and 5.11 compare the fuel salt and graphite temperature distributions, respectively.

The fuel temperature profiles agree well with each other. However, the graphite temperature profiles show noticeable differences. The temperature profile of SAM obtained with

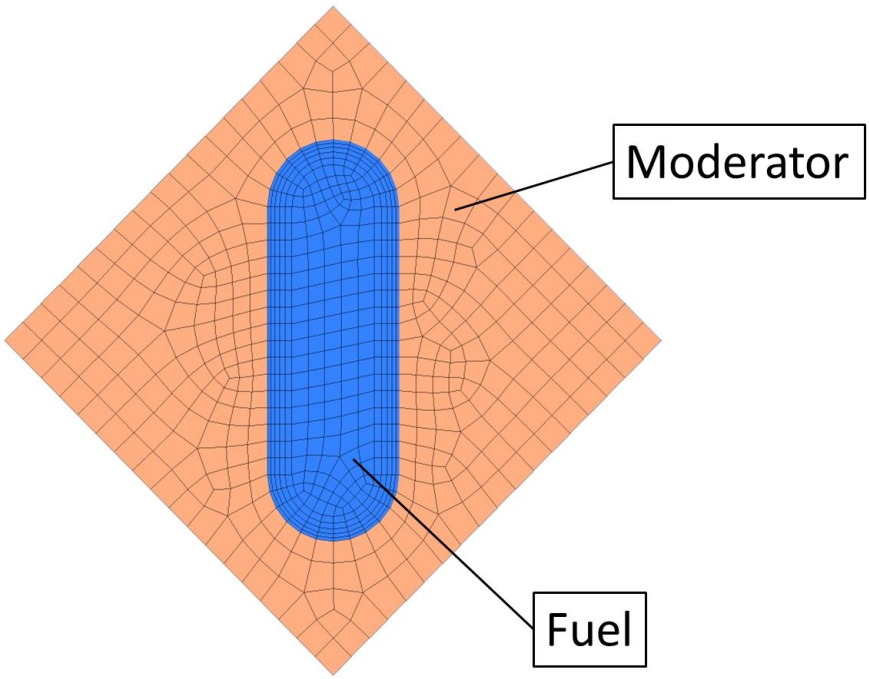


Figure 5.8. Mesh utilized in CFX calculation for fuel channel of MSRE.

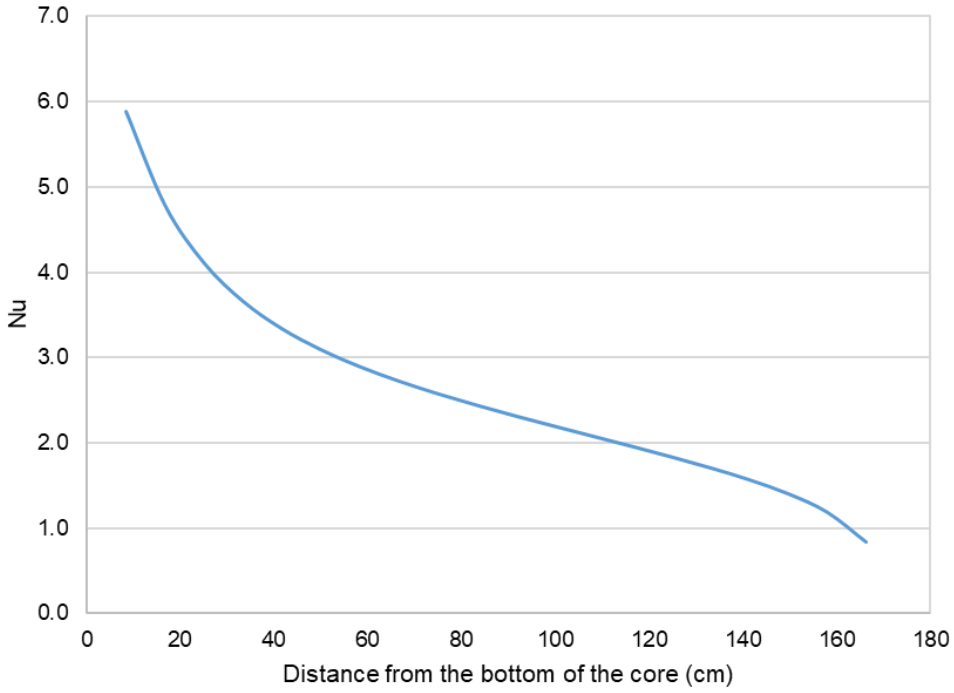


Figure 5.9. Axial variation of Nusselt number in MSRE fuel channel obtained from CFX.

the position-dependent Nusselt number matches well the CFX result. The temperature profile of SAM obtained with a Nusselt number of 4.36 is generally lower than the CFX result because the Poppendiek effect was neglected. The temperature profile of SAM with a Nusselt number of 0.767 is higher than the CFX result because this Nusselt number was obtained with the assumption of a fully developed flow. The Nusselt number for the fully developed region is smaller than the entrance region, and thus the heat transfer coefficient was underestimated when the Nusselt number of 0.767 was used. Unexpectedly, the moderator temperature of SAM with a Nusselt number of 0.767 was quite different from the ORNL result although the Poppendiek effect was considered in both analyses. It was found that the fuel thermal conductivity utilized in the ORNL calculation was 4.76 W/mK, which was significantly higher than the correct value of 1.44 W/mK [86]. Because of this higher thermal conductivity, the ORNL result was much lower than the SAM result with a Nusselt number of 0.767.

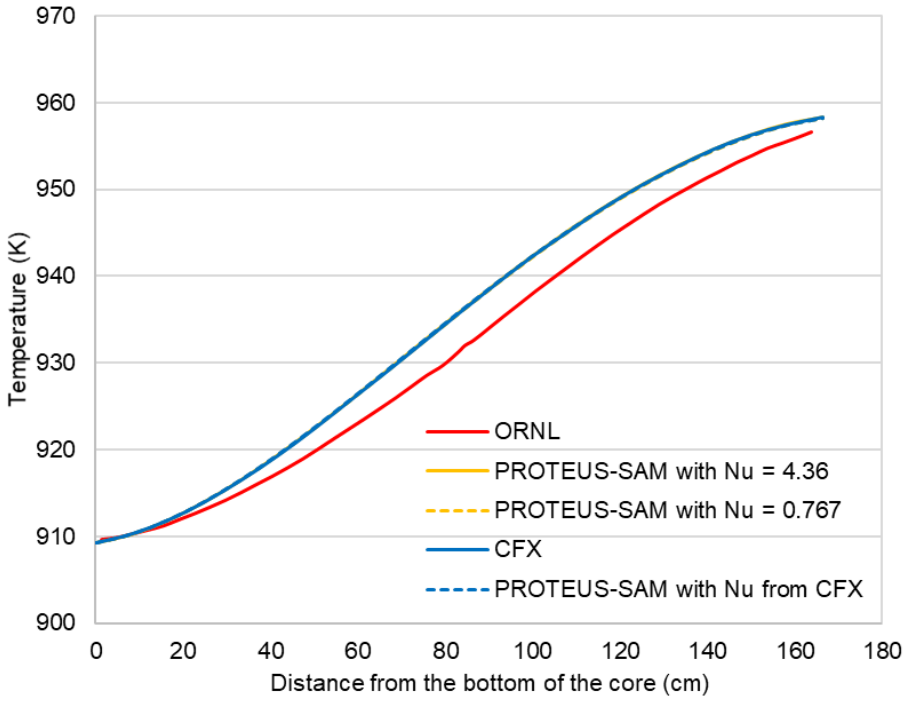


Figure 5.10. Axial temperature distributions of fuel salt in the hottest channel of MSRE.

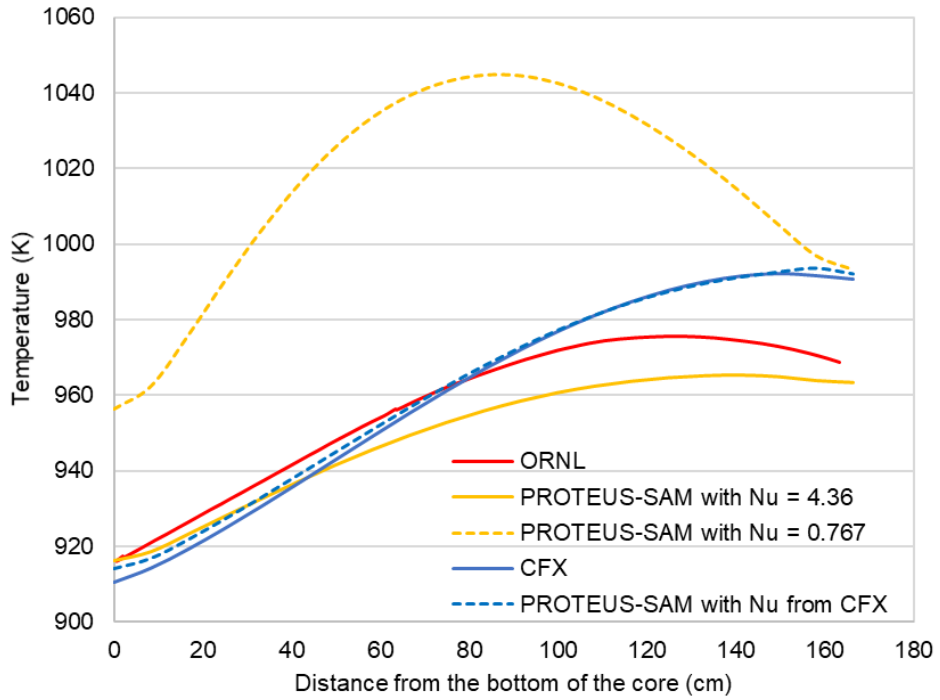


Figure 5.11. Axial temperature distributions of moderator in the hottest channel of MSRE.

5.3 Transient Analyses

The protected pump start-up and coast-down tests at low power (~10 W) and the natural circulation test of the MSRE were analyzed using the coupled PROTEUS-NODAL and SAM code system. The computational times for these analyses with the coupled PROTEUS-NODAL and 1-D SAM code system are shown in Table 5.5. In the protected pump transients, the pump speed was changed to adjust the fuel mass flow rate. Due to the increase or decrease of the fuel mass flow rate, the ratio of delayed neutron precursors out of the core and in the core was increased or decreased accordingly, which in turn caused reactivity loss or gain. Meanwhile, the control rods were adjusted to maintain the core criticality. The control rod positions were converted into the reactivity insertion with the control rod worth of MSRE in [77].

In the coupled PROTEUS-NODAL and SAM calculations, the pump head was increased from zero to its nominal value in the pump start-up test. However, no pump head data was available for the transients. As shown in Fig. 5.12 for the start-up test, the experimental data were available only for the pump speed and secondary coolant flow rate. Therefore, the coolant pump head during transient was first determined to yield the measured coolant flow rates in this calculation. By assuming that the relations between the pump head and the pump speed were the same for the fuel and the coolant pumps, the fuel pump head during the start-up transient was obtained. In the coast-down test, the pump was decreased from full speed to zero. The fuel pump head during coast-down transient was obtained from [87]. The fuel pump head during the start-up and coast-down tests utilized in the coupled calculations are shown in Fig. 5.13.

Table 5.5. Computational Times (s) for MSRE Validation Tests.

Test Problem	Steady State	Start-Up	Coast-Down	Natural Circulation
PROTEUS-1D SAM	118	4073	3387	40796

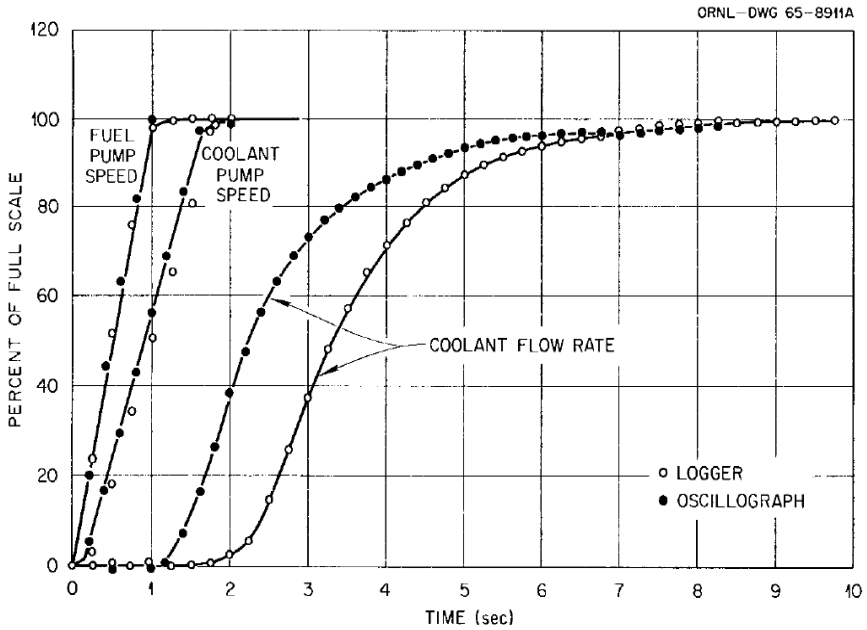


Figure 5.12. Pump speed and secondary flow rate during start-up test [86].

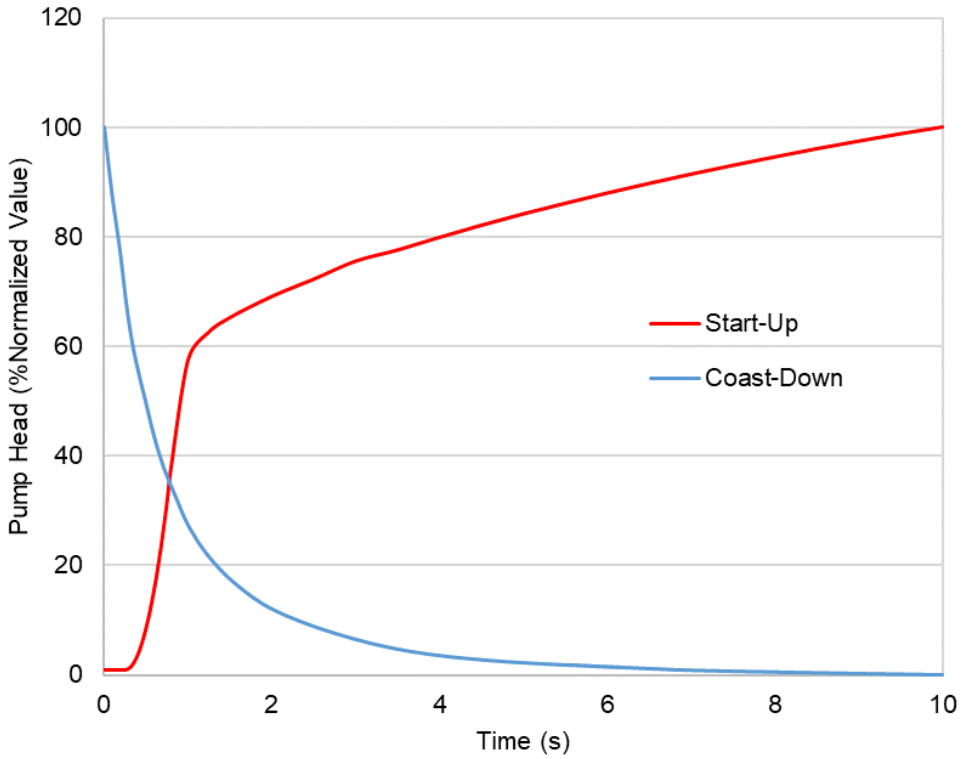


Figure 5.13. Pump head during protected pump start-up and coast-down transients.

Figure 5.14 presents a comparison of the coupled PROTEUS-NODAL and SAM calculation results with the measurement values for the protected pump start-up and pump coast-down. The reactivity loss was calculated by taking the difference between the effective delayed neutron fractions of stationary and flowing fuel at each time step. In the protected pump start-up transient, the flow velocity increases with time and more delayed neutron precursors decay outside of the core. The resulting reactivity loss increases as the fuel salt velocity increases. At around 15s, the reactivity loss starts to decrease and shows an oscillatory behavior later due to the recirculated precursors. During the pump coast-down transient, the flow velocity decreases and less delayed neutron precursors decay outside of the core. Thus, the reactivity loss relative to the stationary fuel decreases as the flow velocity decreases. The results of the coupled PROTEUS-NODAL and SAM calculations generally match the trend of the measured data. The difference between the calculated

reactivity loss of coupled calculations and the measurement can be attributed to the difference between the derived pump head and the real experimental pump head during transients and the difference in the delayed neutron data.

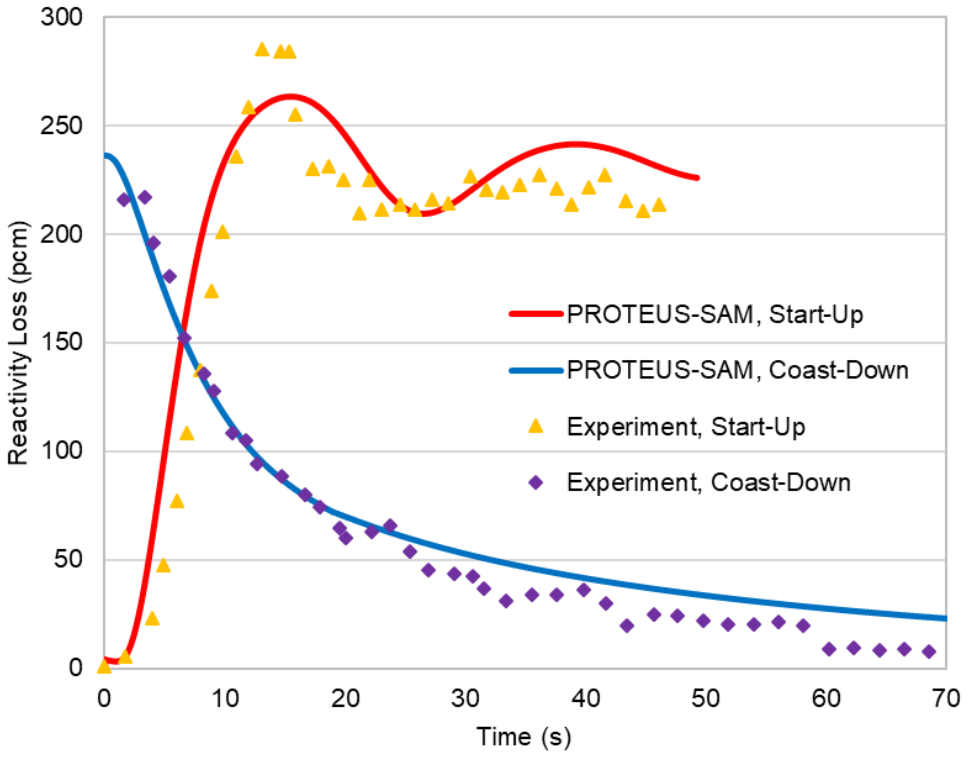


Figure 5.14. Compensated reactivity during protected pump start-up and coast-down transients.

5.3.1 Natural Circulation Test

A natural circulation test was conducted with U-233 fuel to determine the heat removal from the MSRE fuel system by the natural-convection flow of the fuel salt [88]. Before the transient, the reactor was operated at low power (about 4.1 kW) with a limited fuel flow rate. After that, the heat removal rate at the radiator was increased and thus the core inlet temperature was decreased. During the transient, there was no control rod movement. The reactor power, inlet and outlet temperatures at the primary and secondary sides of the heat exchanger are provided in [88].

However, there is no data available for the heat removal rate of the radiator during the transient. Thus, the outer loop was removed from the SAM model and only the core part was modeled with parallel channels. The inlet mass flow rate and temperature of the fuel salt were deduced from the recorded data in Fig. 5.15, and they were utilized as the inlet boundary conditions in the SAM model. Figure 5.16 compares the power evolution of the coupled PROTEUS-NODAL and SAM calculation with the measured data. The calculated power matches well the experimental data. At the beginning of the transient, the calculated and measured results show different trends. This is likely due to the experiment not starting from an equilibrium condition [89]. Since the power change during the natural circulation test was controlled by inherent thermal feedback of the system, this result indicates that the coupled PROTEUS-NODAL and SAM code system is able to predict the power evolution due to thermal feedback during transients.

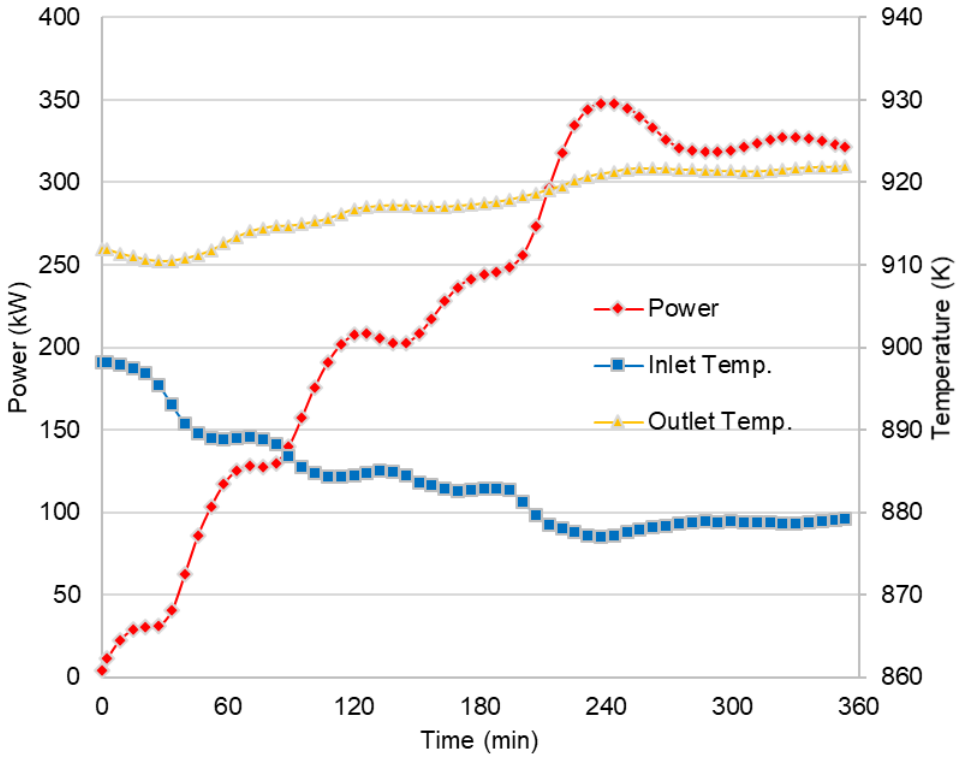


Figure 5.15. Recorded power and average inlet and outlet temperatures during natural circulation test.

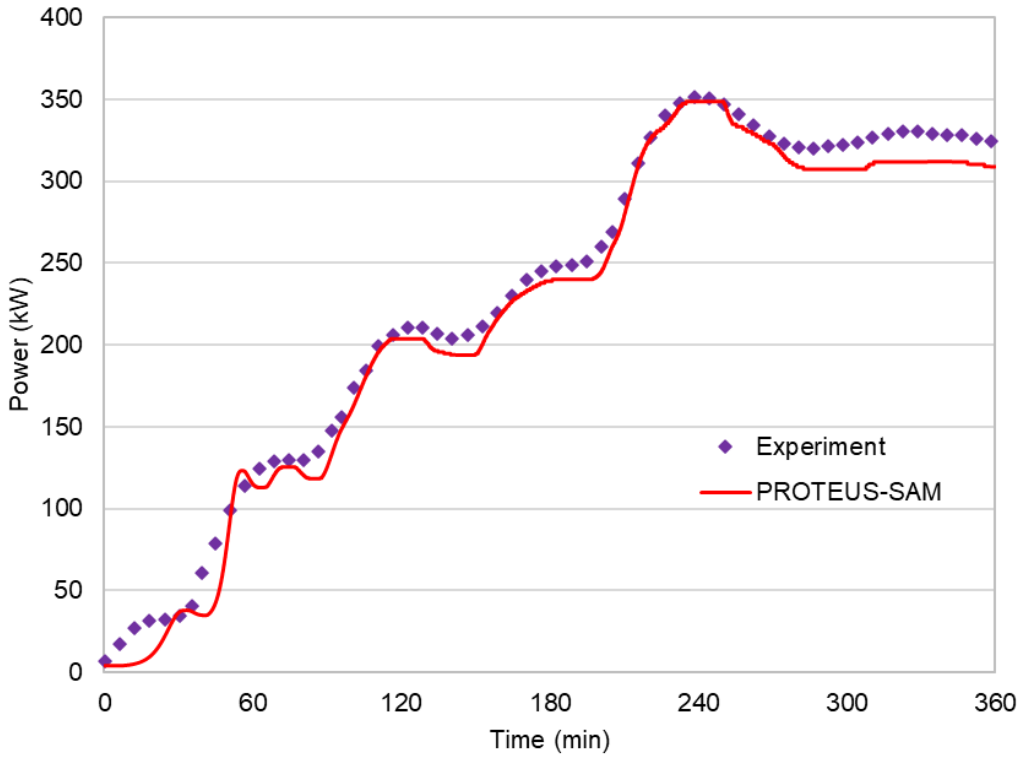


Figure 5.16. Comparison of power evolution during natural circulation test.

5.4 Summary

The coupled PROTEUS-NODAL and SAM code system was validated with available experimental data of the MSRE experiments in this chapter. The R-θ-Z model of PROTEUS-NODAL and the multiple parallel channel model of 1-D SAM were developed for MSRE. To obtain accurate temperature profiles, position-dependent Nusselt numbers were derived from CFD calculations. The protected pump transients at zero power were analyzed with the coupled code system of PROTEUS-NODAL and SAM. The predicted reactivity losses due to delayed neutron precursor drift in the core agreed well with the measured values during the transients. The analysis of the natural circulation test of MSRE showed that the coupled PROTEUS-NODAL and SAM code system could reproduce the measured power evolution due to thermal feedback.

Chapter 6 Multiphysics Coupling of PROTEUS-MOC and SAM for Micro-reactor Applications

In this chapter, the coupling of PROTEUS-MOC and SAM for micro-reactor applications is discussed. Similar to the coupling of PROTEUS-NODAL and SAM, a MOOSE wrapper of PROTEUS-MOC was developed to facilitate the coupling with SAM. In the coupled calculation, PROTEUS-MOC wrapper serves as the master application to control the simulation process and SAM is the sub-application. Inside the first level SAM sub-application for 3D heat conduction calculation of the core, there is a second level SAM sub-application modeling each heat pipe separately. The heat transfer inside the heat pipe is modeled with 2D-RZ heat conduction in SAM. The heat pipe and core heat conduction calculation are coupled through boundary heat flux and temperature.

This chapter is structured as follows: first the MOOSE wrapper of PROTEUS-MOC is introduced. Then the coupling scheme of PROTEUS-MOC and SAM is discussed. The analysis results of a unit-cell and one-sixth core problems of the TRISO-fueled heat pipe micro-reactor (HP-MR) with the coupled code system are presented at the end to demonstrate the developed capabilities.

6.1 Coupling of PROTEUS-MOC and SAM for Heat Pipe Cooled Micro-reactor Applications

To wrap PROTEUS-MOC into the MOOSE framework, two main objects, “ExternalProblem” and “ExternalMesh” need to be implemented. A “ProteusMOCProblem”

object is extended from “ExternalProblem” to execute PROTEUS-MOC and transfer data between the wrapper and PROTEUS-MOC within the MOOSE framework. In the “ProteusMOCProblem”, the functions to execute the PROTEUS-MOC and perform data transfer between PROTEUS-MOC and its MOOSE wrapper are defined. The data transfer functions are called before and after running PROTEUS-MOC solver at each time step. The “ExternalMesh” object of the PROTEUS-MOC wrapper is defined to store the geometry and solution information of PROTEUS-MOC, which is the MOOSE-native format mesh. To facilitate the syncing information, the elements in the wrapper mesh and elements in the PROTEUS-MOC mesh are one-to-one identical. In this way, the solution data can be transferred with a direct copy. For this, the “ProteusMeshTransfer” function is defined to convert the PROTEUS ASCII format mesh [90] to MOOSE-native format mesh. Considering that PROTEUS-MOC and MOOSE employ different domain decomposition schemes in parallel computing, a mapping scheme was added to connect each element in PROTEUS-MOC and MOOSE wrapper for parallel data transfer.

To support the Picard iteration and the other advanced execution functionalities in the MOOSE framework, two methods “backup” and “restore” need to be implemented in the PROTEUS-MOC wrapper. In the backup method, a “Backup” object is returned to store all the data which are needed to restore to this state. The data in the Backup object is saved into the disk as “checkpoint” files in the MOOSE framework and a separate file holds for the data in each thread in parallel simulations. The restore method is used to read the backup data and reconstruct the state. In the Picard iteration, each application is solved multiple times to a converged solution. After one Picard iteration, if the coupled solution is not converged, each application needs to restore to the state of the last time step using the backup data in the checkpoint files.

In the coupled PROTEUS-MOC and SAM code system for micro-reactor simulation, the PROTEUS-MOC wrapper is the master application, which calls PROTEUS-MOC solver to calculate the power distribution and transfers it to 3D heat conduction calculation in SAM. 3D heat conduction calculation of SAM is the level 1 sub-application calculating the core temperature distribution and transferring it back to the master application. The data transfer is performed through the MOOSE function "MultiAppProjectionTransfer". Inside the SAM calculation, heat pipes are modeled separately as the level 2 sub-applications. The heat pipe surface temperature is transferred from the SAM 3D heat conduction calculation to the corresponding heat pipe sub-application. Meanwhile, the surface heat flux is transferred from the heat pipe sub-application to SAM 3D heat conduction calculation. The overall structure of the coupled PROTEUS-MOC and SAM is shown in Fig. 6.1.

In the PROTEUS-MOC, the multigroup cross sections are functionalized in terms of temperatures for thermal feedback calculation. The microscopic cross sections of fuel isotopes are represented a linear function of $T^{1/2}$. For the non-fuel component, the temperature dependency is represented as a linear function of T. After SAM calculation, the temperature distributions are transferred to PROTEUS-MOC, and the macroscopic cross sections are updated as:

$$\Sigma(T) = N_i[\varepsilon_l \sigma_i(T_l) + \varepsilon_h \sigma_i(T_h)], \tag{6.1}$$

where T_l and T_h are two fuel salt temperatures for which cross sections are prepared, and

$$\varepsilon_l = (T_h^{1/2} - T^{1/2}) / (T_h^{1/2} - T_l^{1/2}), \varepsilon_h = 1 - \varepsilon_l \text{ for fuel,} \tag{6.2}$$

$$\varepsilon_l = (T_h - T) / (T_h - T_l), \varepsilon_h = 1 - \varepsilon_l \text{ for non-fuel.} \tag{6.3}$$

The heat pipe can be modeled as axisymmetric 2D-RZ geometry or 3D-1D coupling between heat structure and vapor core in SAM [61]. In the axisymmetric 2D-RZ geometry, the heat pipe is divided into three blocks: heat pipe wall, heat pipe wick, and heat pipe vapor core.

Figure 6.2 shows the 2D-RZ model for the heat pipe. The vapor core is modeled as a solid material with large thermal conductivity in SAM. The heat pipe model with 3D-1D coupling between heat structure and vapor core is shown in Fig. 6.3. In this model, the vapor core is modeled separately as a 1D heat structure, while the wall and wick are modeled as 3D heat structures. The 3D heat structure and 1D vapor core are coupled through the convective heat transfer at the boundary. Both heat pipe models in SAM were verified with the thermal resistance model [61]. The 2D-RZ model is utilized in this work because of the reduced computational cost of this model. The ability to remove heat for a heat pipe is limited by various phenomena, including capillary, entrainment, boiling, viscous, and sonic limits [46]. However, these operation limits are not modeled in SAM due to the vapor is modeled as solid material.

Figure 6.4 shows the computational flow of the coupled steady state calculations for micro-reactors. There are two levels of Picard iteration in the coupled steady state calculation. The first level Picard iteration is between PROTEUS-MOC and 3D heat conduction calculation in SAM. One PROTEUS-MOC steady state calculation is performed first with the cross sections updated utilizing the temperature distribution from initial conditions or previous iteration solutions of SAM. Then the power distribution is transferred from PROTEUS-MOC to 3D heat conduction calculation in SAM. The second level Picard iteration is between 3D heat conduction and heat pipe calculations in SAM. With the updated power density, core temperature is calculated utilizing the heat pipe surface temperature from initial conditions or the heat pipe sub-applications of the previous level 2 iteration. The heat flux at the heat pipe surface is transferred from the 3D heat conduction calculation to the heat pipe sub-applications. Then the heat pipe sub-applications are executed separately for each heat pipe and the heat pipe surface temperatures are transferred back to the 3D heat conduction calculation. The level 2 Picard iteration is continued until the

convergence criteria are met. After that, the temperature distribution in the core is transferred to PROTEUS-MOC and the level 1 Picard iteration is continued until converge.

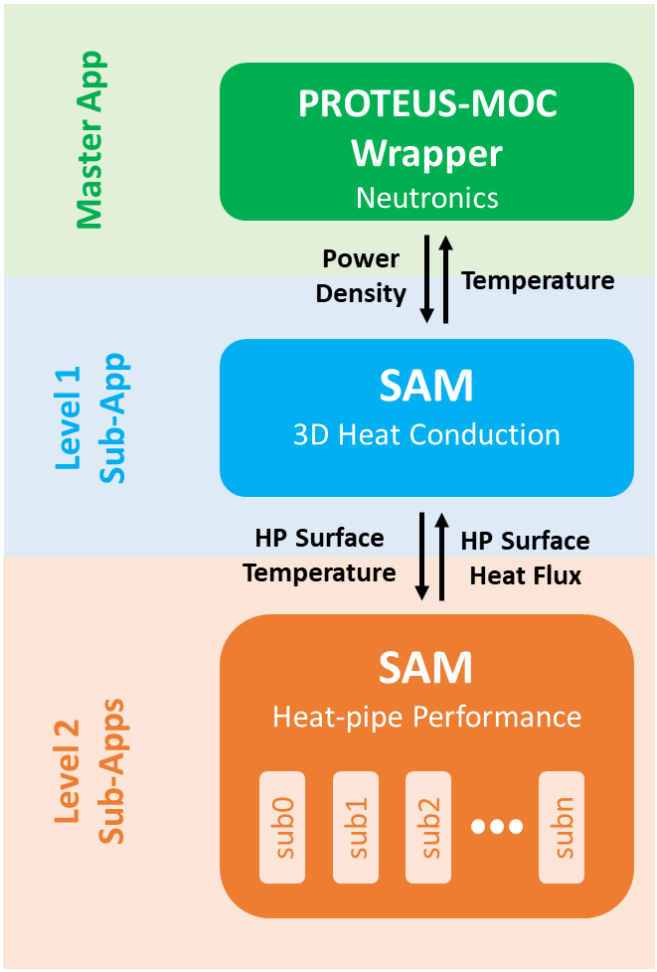


Figure 6.1. Coupling Scheme between PROTEUS-MOC and SAM.

The computational flow for the transient calculation is shown in Fig. 6.5. The coupled transient calculation is restarted from the steady state solutions. At each master time step, the PROTEUS-MOC is executed one step with the temperature from the previous time step. The 3D heat conduction calculation in SAM is performed with the transferred power from PROTEUS-MOC. Then heat flux at the heat pipe surface is transferred from the 3D heat conduction to the heat pipe sub-applications. At the end of the time step, the heat pipe sub-applications are executed

with one time step. Before the master application advances to the next step, the heat pipe surface temperatures are transferred to 3D heat conduction calculation and the core temperature is transferred from SAM to the PROTEUS-MOC wrapper.

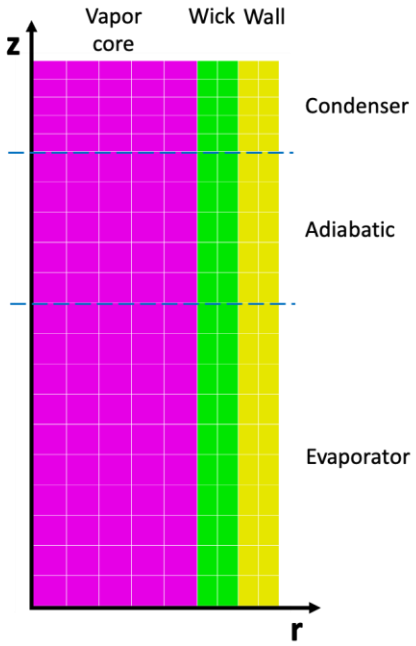


Figure 6.2. Schematic plot of 2D-RZ heat pipe model.

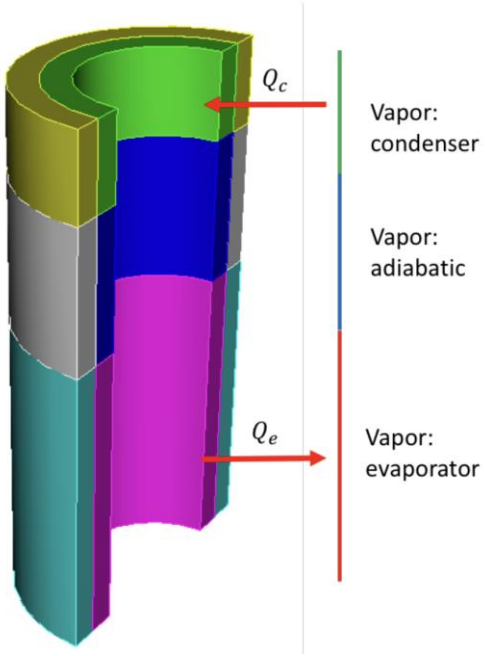


Figure 6.3. Schematic plot of 3D-1D heat pipe model [61].

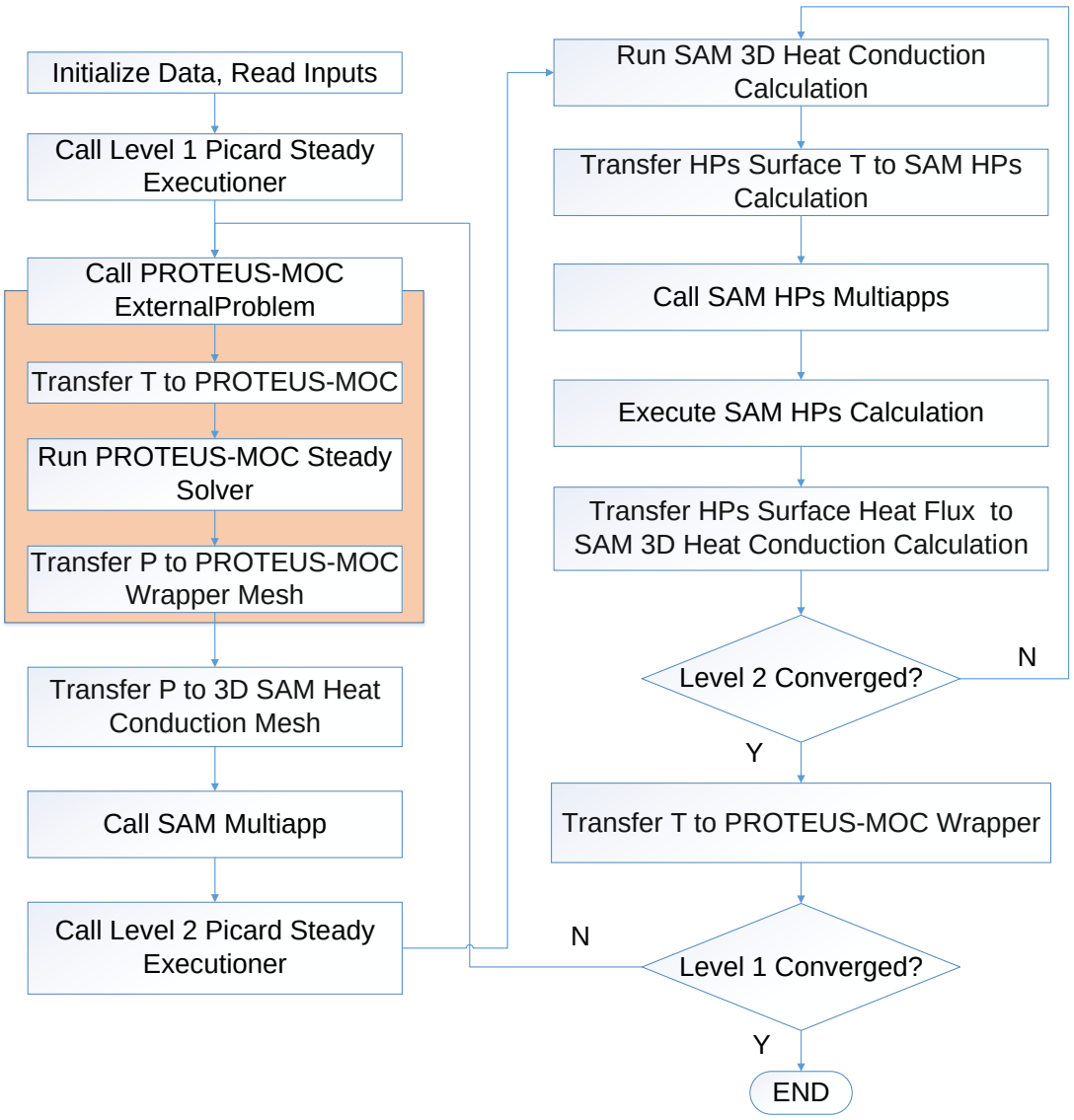


Figure 6.4. Coupling scheme of PROTEUS-MOC and SAM for steady-state calculations.

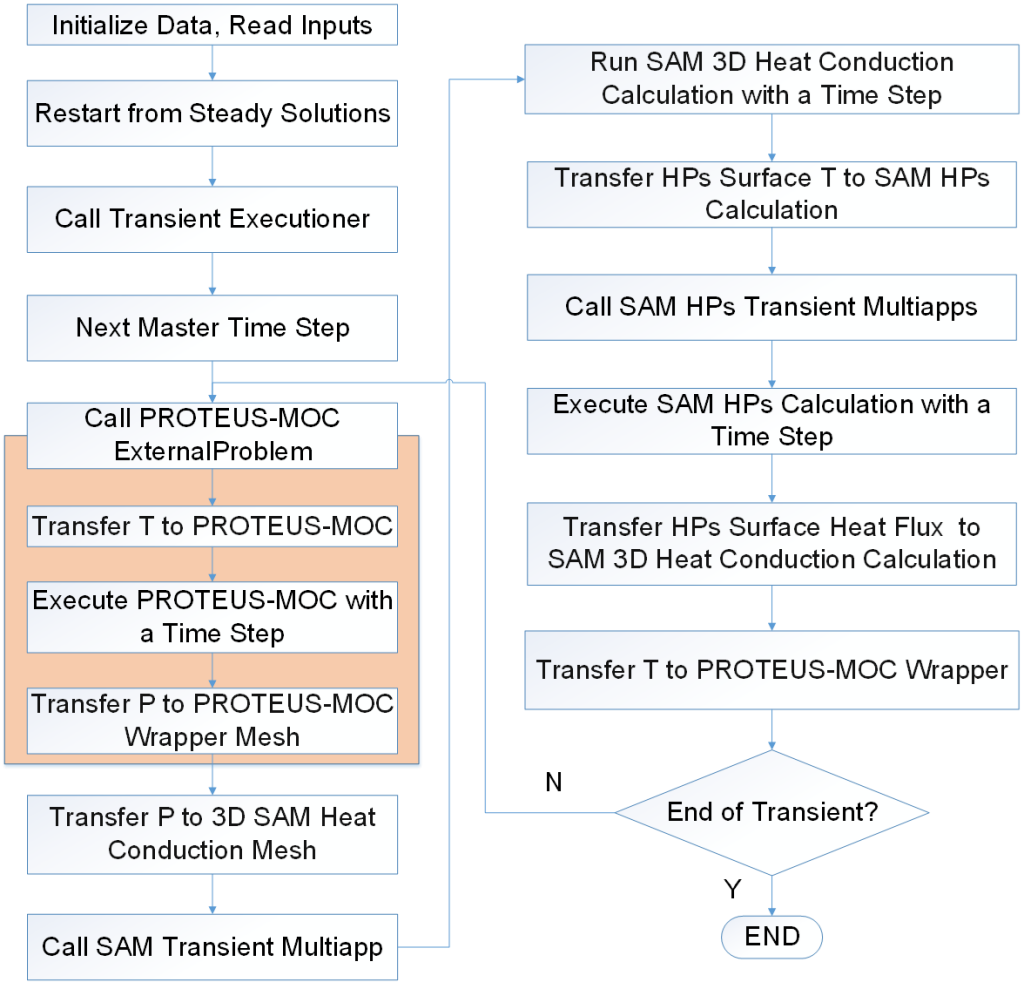


Figure 6.5. Coupling scheme of PROTEUS-MOC and SAM for transient calculations.

6.2 Analysis of the HP-MR Problem with Coupled PROTEUS-MOC and SAM

6.2.1 Description of the HP-MR Problem

The HP-MR concept is developed to address the modeling challenges in the micro-reactor industry [53]. It is a 2 MW thermal reactor with 19.95 at% enriched UCO-form TRISO fuel. The monolith material is graphite and the fluid in the heat pipe is potassium. To achieve a more compact core design, Yttrium-Hydride (YH_2) is selected as the solid moderator material. The YH_2 is surrounded by a layer of thin helium gaps and a stainless-steel envelope. The envelope of the

moderator pin is separated from the graphite monolith with another thin helium layer. There are 30 hexagonal fuel assemblies and 12 B_4C control drums in the core. The core is surrounded radially and axially by beryllium reflectors. The height of the core, upper reflector, and lower reflector are 160 cm, 20 cm, and 20 cm, respectively. In the core center, an emergency shutdown control rod can be inserted to provide additional safety control and it is fully withdrawn during normal operation. The heat pipe evaporator length, adiabatic section length, and condenser length are 180 cm, 30 cm, and 90 cm, respectively. The main characteristics of HP-MR are summarized in Table 6.1. The radial and axial configurations of the HP-MR are given in Fig. 6.6. The radial layout of the fuel assembly in HP-MR is shown in Fig. 6.7. In a fuel assembly, there are 63 fuel pins, 37 moderator pins, and 27 heat pipes.

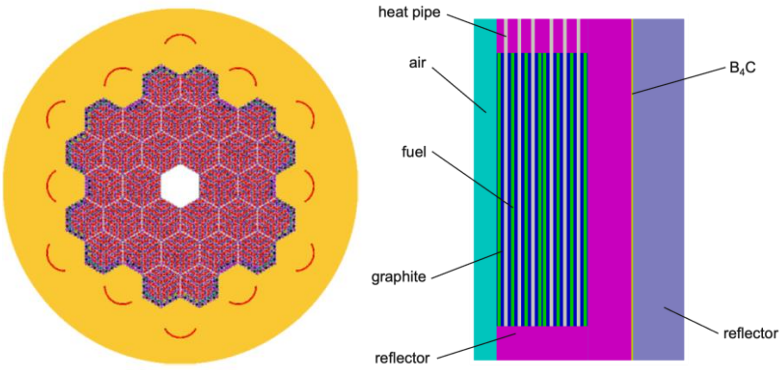


Figure 6.6. Radial (left) and axial (right) configurations of the HP-MR problem.

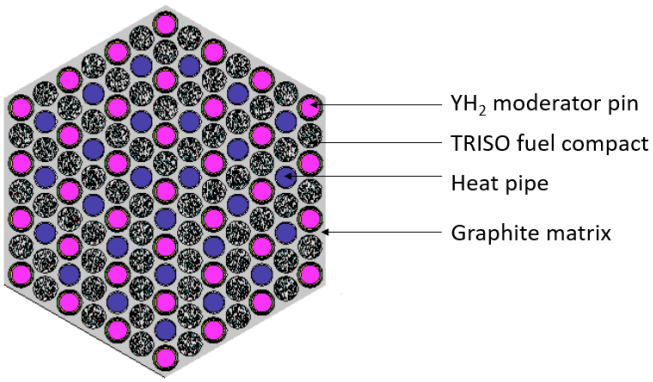


Figure 6.7. Radial layout of the fuel assembly of the HP-MR problem.

Table 6.1. The main characteristics of HP-MR

Material	Description	
Graphite matrix	1.806 g/cm^3, 0.3ppm B-10	
Fuel compact outer radius	1.0 cm	
TRISO fuel packing fraction	40%	
Heat pipe outer radius	1.07 cm	
Heat pipe description	Density	Radius
- K void	0.00011 g/cm^3	0.80 cm
- Wick: (70vol%K – 30vol%SS316)	2.753 g/cm^3	0.90 cm
- K layer	0.705 g/cm^3	0.97 cm
- SS316 envelope	7.67 g/cm^3	1.05 cm
- He Gap	0.00018 g/cm^3	1.07 cm
Moderator pin outer radius	0.920 cm	
Moderator pin description	Density	Radius
- YH_2 moderator	4.3 g/cm^3	0.825 cm
- Helium gap	0.00018 g/cm^3	0.875 cm
- SS316 envelope	7.9 g/cm^3	0.900 cm
- Helium gap	0.00018 g/cm^3	0.920 cm
Absorber inner radius	12 cm	
Absorber thickness	1 cm	
Absorber sector angle	120^o	
B-10 enrichment (at. %)	20%	

6.2.2 Analysis of the Unit-cell Problem of HP-MR

To demonstrate the capability of the coupled PROTEUS-MOC and SAM code system for micro-reactor simulation, a 3D unit-cell problem of HP-MR was analyzed with the coupled code system. The steady and transient results were compared with those calculated with the coupled Griffin, BISON, and Sockeye codes from the literature [53]. This unit-cell problem consists of one central heat pipe, three 1/3 fuel pins, and three moderator pins. The fuel pin power is set to be 1.8 kW. Figure 6.8 presents the radial and axial configurations of this unit-cell problem.

In the PROTEUS-MOC calculation, the region-dependent multigroup cross sections were generated with the Monte Carlo code Serpent [90] in an 11-group structure. In the Serpent model, individual TRISO particles were modeled by random sampling of these particles in the fuel compacts. A detailed description of the Serpent model was given in the reference [53]. To account for the reactivity feedback mechanism of the micro-reactor, the multigroup cross sections were modeled as a function of temperature and they were generated based on the isothermal Serpent model with temperatures of all the materials varied among 600 K, 700 K, 800 K, 1000 K, and 1200 K, respectively. The Serpent outputs were converted to ISOTXS format using the utility code GenISOTXS [91]. With another utility code GenISOPAR [92], different ISOTXS files for different temperatures were merged into one ISOPAR file, which can be used to evaluate temperature-dependent cross sections in PROTEUS-MOC.

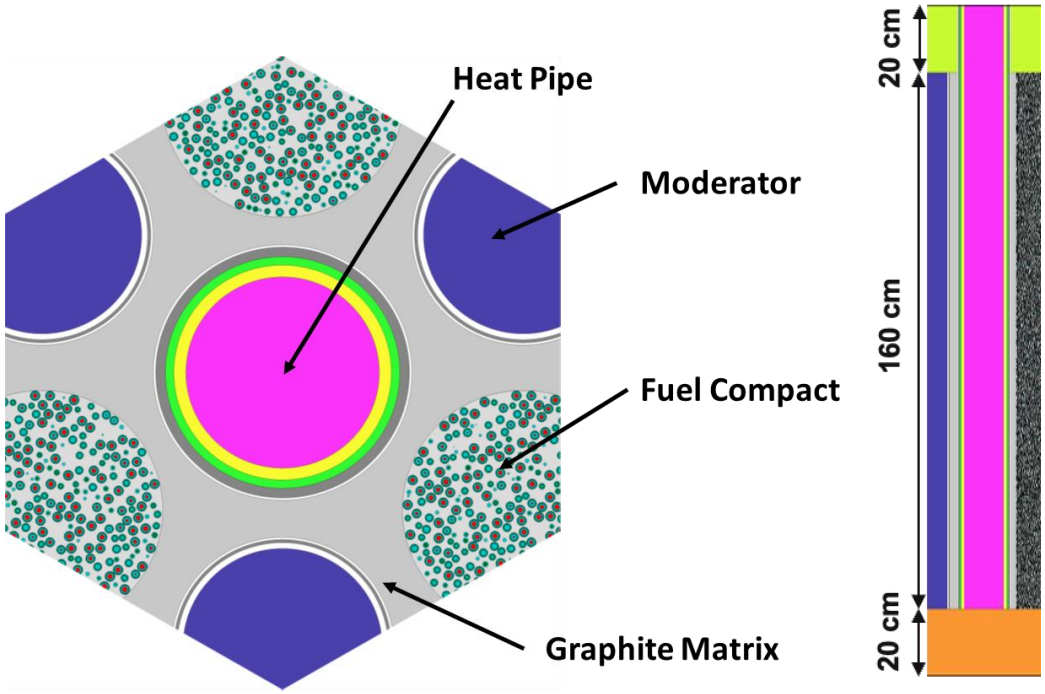


Figure 6.8. Radial (left) and axial (right) configurations of the unit-cell problem.

The computational models in PROTEUS-MOC and 3D heat conduction calculation of SAM are shown in Fig. 6.9. In each axial plane of PROTEUS-MOC model, average temperatures were calculated for each region, marked by different colors in Fig. 6.9, to evaluate the effective cross sections. In the PROTEUS-MOC model, the reflective boundary condition was given radially, while the vacuum boundary condition was applied to the top and bottom reflector surfaces. In the 3D heat conduction calculation of SAM, the adiabatic boundary condition was used in the radial boundary surfaces. On the top and bottom surface, a convective boundary condition with an ambient temperature of 800 K and a heat transfer coefficient of 100 W/m^2K was utilized. In the heat pipe condenser wall, the convective boundary condition was applied with an ambient temperature of 800 K and the heat transfer coefficient was set to 10^6 W/m^2K to approximate the fixed temperature boundary condition.

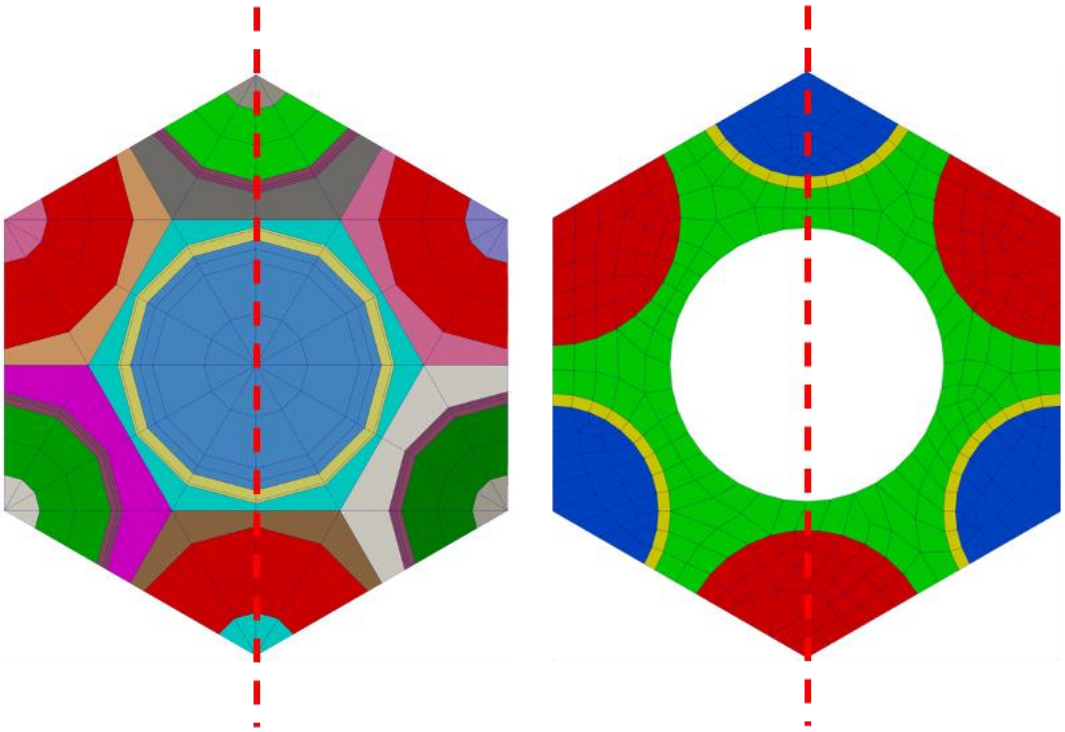


Figure 6.9. Mesh for PROTEUS-MOC (left) and 3D heat conduction calculation of SAM (right).

Table 6.2 shows the eigenvalues from PROTEUS-MOC isothermal calculations, Griffin isothermal calculations with transport solvers, and Griffin isothermal calculations with diffusion solvers and diffusion solvers with SPH factors, as well as reference solutions from Serpent. In the PROTEUS model, there are 216 elements in each plane and 40 axial planes. The MOC calculations in PROTEUS are performed with a ray space of 0.05 cm and the Legendre-Tchebychev product quadrature with 6 polar and 64 azimuthal angles (i.e., total 384 directions in 4π). In the Griffin model, there are 490 elements in each plane and 40 axial planes. The SN calculations of Griffin use the CFEM solver with the Gauss-Chebyshev quadrature and a total of 72 directions. For the Griffin calculations with the SPH factors, the SPH factors are generated for a total of 208 equivalence zones with 40 equivalent zones in the axial direction using the reference Serpent solutions. The SPH method procedure in Griffin is described in detail in Appendix 1 of the reference [53].

Table 6.2. Comparison of eigenvalues for unit-cell problem.

Temperature (K)	Serpent k-eff	PROTEUS-MOC		Griffin-SN		Griffin-Diffusion		Griffin-SPH	
		k-eff	Diff. (pcm)	k-eff	Diff. (pcm)	k-eff	Diff. (pcm)	k-eff	Diff (pcm)
600	0.98056 ± 0.00004	0.98086	30	0.98506	450	0.97603	-453	0.98056	0
700	0.97927 ± 0.00004	0.97943	16	0.98351	424	0.97306	-621	0.97927	0
800	0.97811 ± 0.00004	0.97821	10	0.98221	410	0.97052	-759	0.97811	0
1000	0.97560 ± 0.00004	0.97542	-18	0.97931	371	0.96560	-999	0.97560	0
1200	0.97260 ± 0.00004	0.97216	-43	0.97601	340	0.96068	-1192	0.97260	0

The solutions from PROTEUS-MOC agree with the eigenvalues from Serpent. The maximum difference for eigenvalues between the PROTEUS-MOC solution and Serpent solution is -43 pcm at 1200 K. As expected, the eigenvalues from Griffin diffusion calculations show

relatively large deviations from the Serpent results. The maximum eigenvalue difference between the Griffin diffusion solution and the Serpent solution is -1193 pcm in 1200 K. The Griffin transport solutions with S_n solver show better agreement than the diffusion solutions. The maximum difference between the Griffin transport solution and the Serpent solution is 450 pcm in 600 K. The Griffin transport solution can be further improved by utilizing higher S_n order. With the SPH factors applied in the Griffin diffusion calculations, the results from Griffin match the Serpent solutions in all five temperatures.

Table 6.3 lists the calculated temperature feedback coefficients from two adjacent temperature points. For example, the isothermal temperature feedback coefficients at 600 K are calculated with the eigenvalues of the isothermal calculations at 600 K and 700 K. The results show that the temperature feedback coefficients from Serpent, PROTEUS-MOC, Griffin transport and Griffin diffusion with SPH factors calculations are in good agreement. The maximum difference is -0.15 pcm/K between the temperature feedback coefficients from PROTEUS-MOC and Serpent and -0.25 pcm/K between Griffin transport and Serpent. While the temperature feedback coefficients from Griffin diffusion calculations are highly overestimated compared to the Serpent results. The temperature feedback coefficient at 600 K from Griffin diffusion calculation is 2.3 times more negative than that from Serpent calculations. With the SPH factors applied in the Griffin diffusion calculations, the temperature feedback coefficients match the Serpent results.

Figure 6.10 shows the axial power distributions for the unit-cell problem of isothermal calculations at 800 K. The axial power distribution from the PROTEUS-MOC and Griffin transport calculations agrees with the Serpent solution. The maximum relative difference of the power density between the PROTEUS-MOC and Serpent results is 4.70%, located near the bottom

reflector. The maximum relative power density difference between the Griffin transport agrees with the Serpent solution. The maximum relative difference of the power density between the PROTEUS-MOC and Serpent results is 4.70%, located near the bottom reflector. The maximum relative power density difference between the Griffin transport calculation and Serpent results is 8.32%. As expected, the axial power distribution of the Griffin diffusion solution is different from that of the Serpent solution. The diffusion solution overestimates the power in the lower ~1/3 of the core and underestimates the power in the upper ~2/3 of the core. With the SPH factors applied in the Griffin diffusion calculations, the axial power distribution matches the Serpent reference solution.

Table 6.3. Comparison of isothermal temperature feedback coefficients (pcm/K) for unit-cell problem.

Temperature (K)	Serpent	PROTEUS-MOC	Griffin-SN	Griffin-Diffusion	Griffin-SPH
600	-1.34 ± 0.06	-1.49	-1.60	-3.13	-1.34
700	-1.21 ± 0.06	-1.27	-1.35	-2.69	-1.21
800	-1.32 ± 0.03	-1.46	-1.51	-2.63	-1.32
1000	-1.58 ± 0.03	-1.72	-1.73	-2.65	-1.58

Table 6.4 compares the computational cost of Serpent, PROTEUS-MOC, and Griffin transport and diffusion calculations. The Griffin calculations were performed on the Argonne NSE division Linux workstation using 60 CPUs [53]. PROTEUS-MOC calculations were performed with 40 CPUs on the HPC Cluster of the University of Michigan, in which the Intel Xeon Gold 6154 CPUs with 3.0 GHz frequency were used. Although the difference in the computational time between PROTEUS-MOC and Griffin can be affected by different machines utilized, the PROTEUS-MOC transport calculations showed a significant reduction of the computational cost

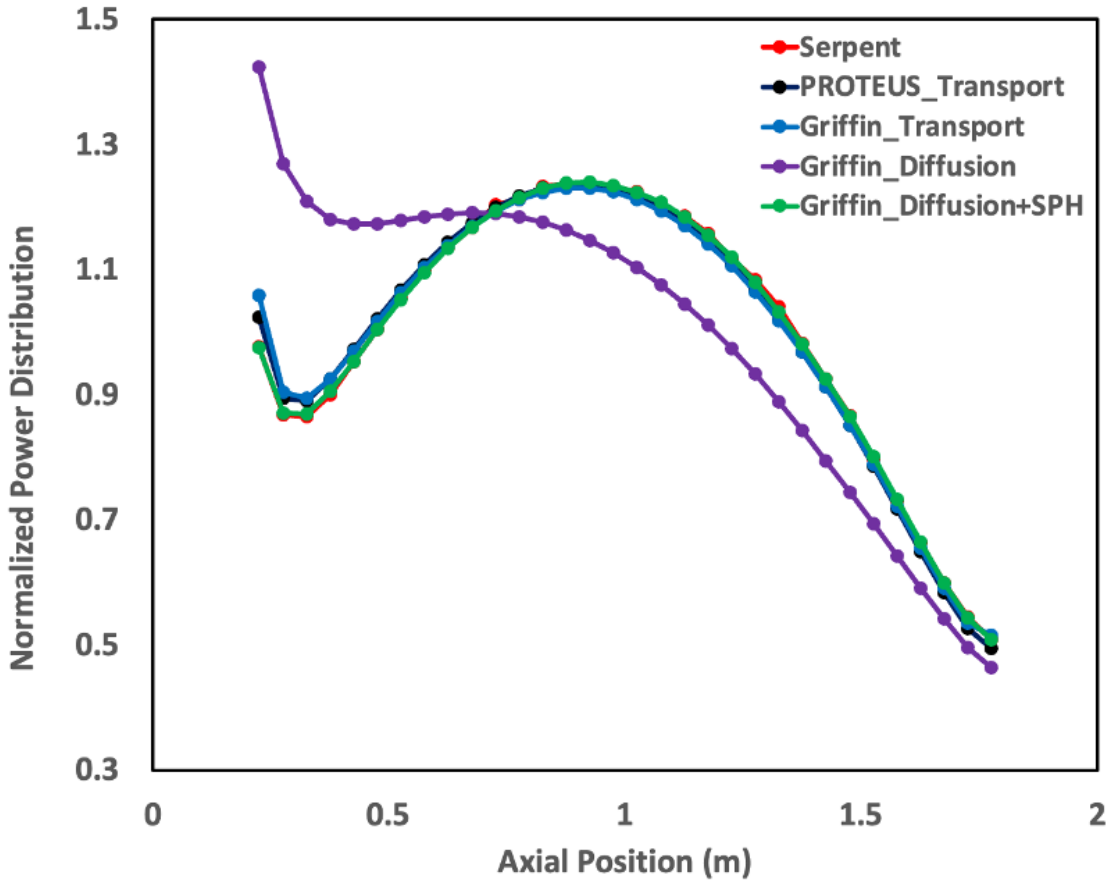


Figure 6.10. Axial power distributions for the unit-cell isothermal calculations at 800 K.

compared to Griffin transport and Serpent calculations. Even compared to the Griffin diffusion calculations, there was around 5-10 times reduction in computational cost. The computational cost reduction of PROTEUS-MOC mainly comes from two reasons. The first is that the mesh number required in the PROTEUS-MOC calculation is smaller than in the Griffin. The mesh number of PROTEUS-MOC is less than half of that in Griffin calculations. Another reason is that the uCMFD acceleration scheme in PROTEUS-MOC accelerates the transport calculations effectively. The long computer running time makes the Griffin S_N transport solver impractical to apply to the multiphysics simulations unless efficient acceleration schemes are developed for transport

calculation [53]. In contrast, the transport solver of PROTEUS-MOC is applicable in the multiphysics coupled simulation of micro-reactors.

Multiphysics analyses were performed for this unit-cell problem with the coupled PROTEUS-MOC and SAM code system. The results were compared with the solutions from the coupled Griffin/BISON/Sockeye calculations. The diffusion solver with SPH factors was utilized

Table 6.4. Computational cost (CPU-hour) for the isothermal calculations of unit-cell problem.

Temperature (K)	Serpent	PROTEUS-MOC	Griffin-SN	Griffin-Diffusion
600	348.02	0.31	116.84	2.81
700	314.20	0.23	116.64	2.78
800	331.70	0.29	119.61	2.94
1000	331.15	0.33	120.91	2.87
1200	346.67	0.24	118.56	2.82

in the Griffin calculations. The cross sections and SPH factors were tabulated as the functions of fuel and moderator temperatures in Griffin. However, the feedback model in PROTEUS-MOC was different, in which multigroup cross sections in each region were modeled as a function of the temperature in that region. For a consistent comparison, the thermos-physical properties of fuel and graphite block applied in SAM were obtained from the properties of the "GraphiteMatrixThermal" material in BISON. The mesh utilized in the 3D heat conduction calculations of SAM was the same as that in the BISON calculations. For the heat pipe calculations, the 2D-RZ model was utilized in SAM and Sockeye. In both models, the vapor core was modeled as a solid material with a large thermal conductivity of 1.3×10^{6} W/m·K. Table 6.5 compares the eigenvalue and average temperatures of the unit-cell problem from two different coupled calculations. The eigenvalue from the coupled PROTEUS-MOC and SAM calculation is 0.97698 and the coupled steady state calculations converge at the third Picard iteration between PROTEUS-MOC and SAM. The eigenvalue from the coupled Griffin/BISON/Sockeye calculation is 0.97750.

The power and temperature distributions along the Y-Z plane from two coupled calculations are given in Fig. 6.11 and Fig. 6.12, respectively. This Y-Z plane locates in the middle of the unit-cell and its position is shown as the red line in Fig. 6.9.The maximum power density of PROTEUS-MOC and Griffin solutions are 4.48E6 W/m^3 and 4.36×10^6 W/m^3, respectively. The difference in the maximum temperature between SAM and BISON solutions is 0.6 K. The maximum temperature of SAM is 857.1 K and that of BISON is 856.5 K.

Figure 6.13 compares the axial temperature distributions of fuel, moderator, and graphite from two coupled simulations. The results show that the average temperatures from SAM and BISON agree well. The maximum difference in average fuel temperature is 1.8 K. Figure 6.14 shows the axial temperature distributions at the wick-vapor interface for the coupled calculations of the unit-cell problem. The axial temperature distributions at the wick-vapor interface from SAM and Sockeye match with each other. In both results, the temperature decreases quadratically in the evaporator and condenser sections due to the heat source and sink out of the heat pipe wall. The temperature decreases linearly in the adiabatic region due to no heat gain or loss from the heat pipe wall of this region.

Table 6.5. Eigenvalues and average temperatures for the multiphysics calculations of unit-cell problem.

	Eigenvalue	Fuel Temp (K)	Mod Temp (K)	Graphite Temp (K)
PROTEUS-SAM	0.97698	845.9	842.1	842.3
Griffin-BISON-Sockeye	0.97750	845.4	842.1	842.3

The load following power transient for the unit-cell problem was analyzed with the coupled PROTEUS-MOC and SAM code system. This transient was simulated by reducing the convective heat transfer coefficient at the secondary side from 10^6 W/m^{2}K to 10^2 W/m^{2}K at the beginning of the transient. Figures 6.15 and 6.16 show the power and fuel temperature evolutions from the

coupled PROTEUS and SAM calculation as well as the coupled calculation based on the Griffin diffusion calculation with SPH factors, respectively. In the first 50 s, the power increases in the PROTEUS results. This is due to the reduced convective heat transfer coefficient at the secondary side makes the cooling capability of the heat pipe decrease, and the temperatures of the heat pipe and moderator increase, which leads to the power increase due to the positive feedback of the heat pipe and moderator. After 50 s, the power decreases because of the negative Doppler feedback of the fuel. The power shows oscillatory behaviors and it reaches asymptotic states eventually. The component-wise reactivities for this unit-cell problem are shown in Fig. 6.17. The power evolution trend from Griffin calculation is similar to the trend of the PROTEUS result except for the first 50 s. The power decrease in the first 50 s is due to the feedback of the heat pipe is not considered in the Griffin calculation. Thus the power evolution is dominated by the Doppler feedback of fuel. The computational cost for the coupled transient calculations of PROTEUS-MOC and SAM is 372.04 CPU-hours.

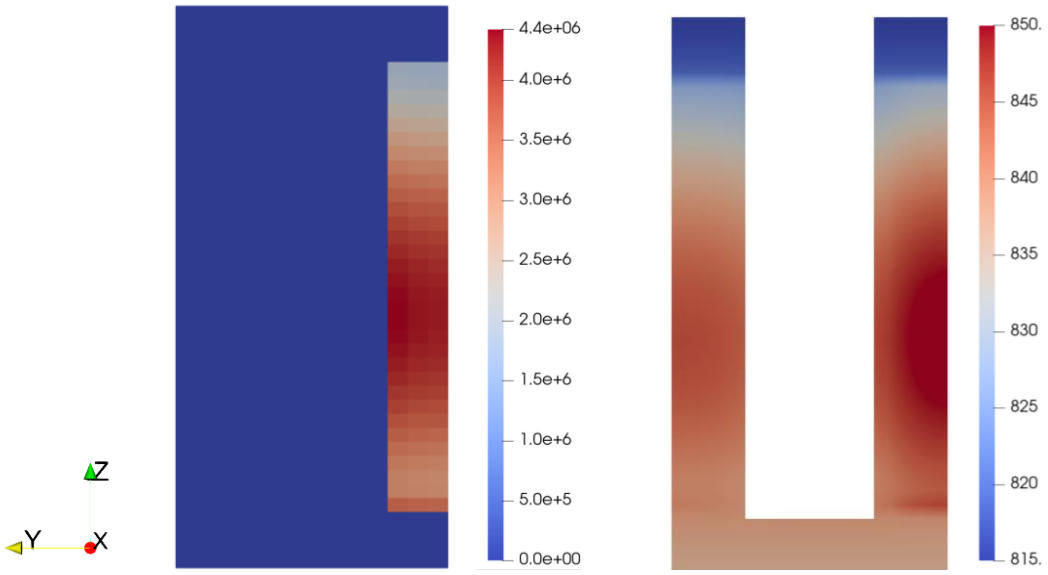


Figure 6.11. Power (W/m^3) and temperature (K) distributions of the unit-cell problem from the coupled PROTEUS-MOC and SAM calculation.

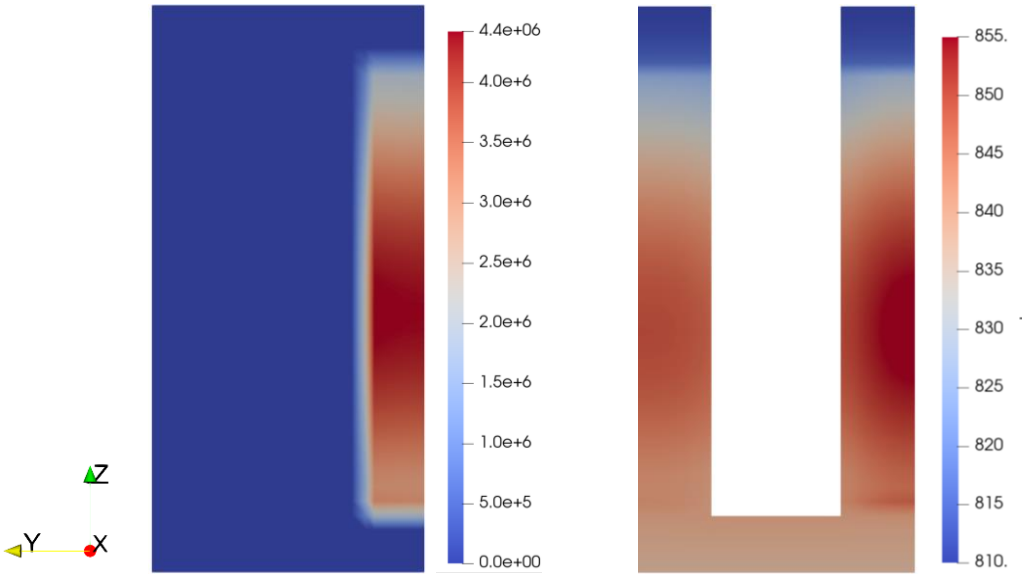


Figure 6.12. Power (W/m^3) and temperature (K) distributions of the unit-cell problem from the coupled Griffin/BISON/Sockeye calculation.

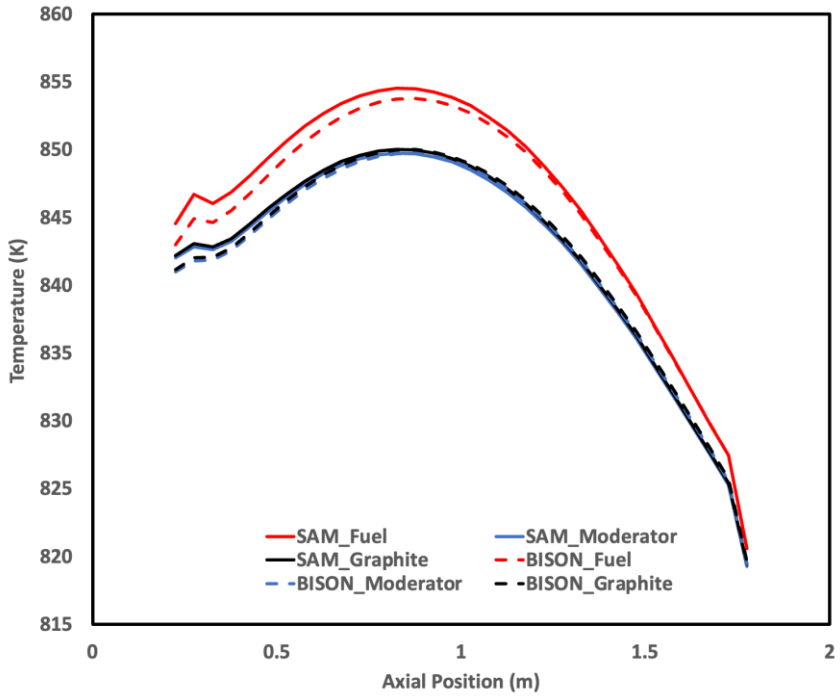


Figure 6.13. Axial temperature distributions from the coupled PROTEUS-MOC/SAM and Griffin/BISON/Sockeye calculations.

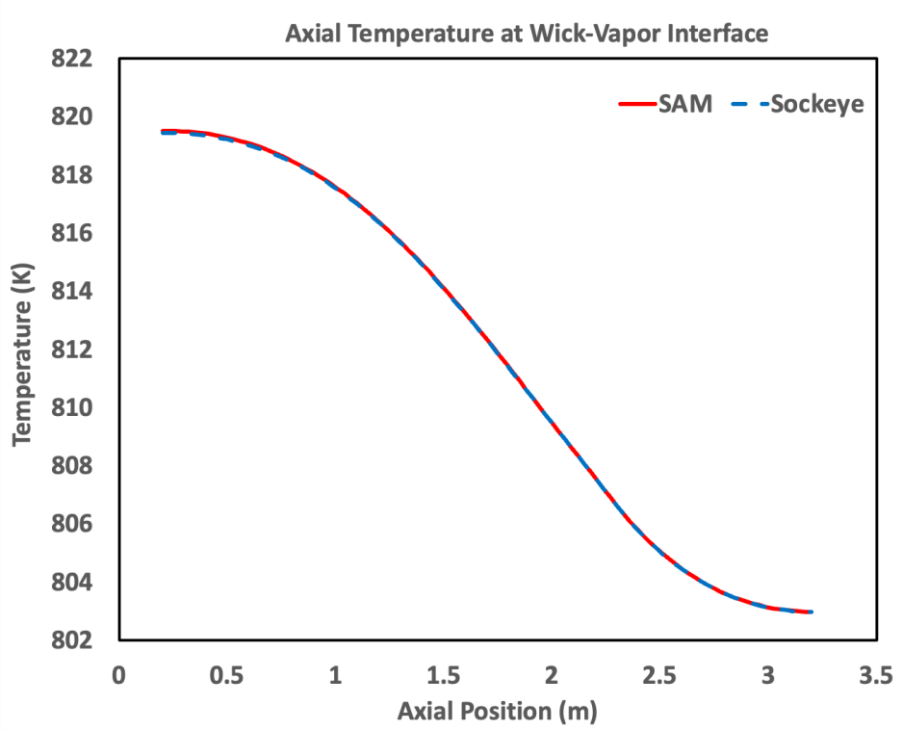


Figure 6.14. Axial temperature distribution at the wick-vapor interface for the coupled calculations of unit-cell problem.

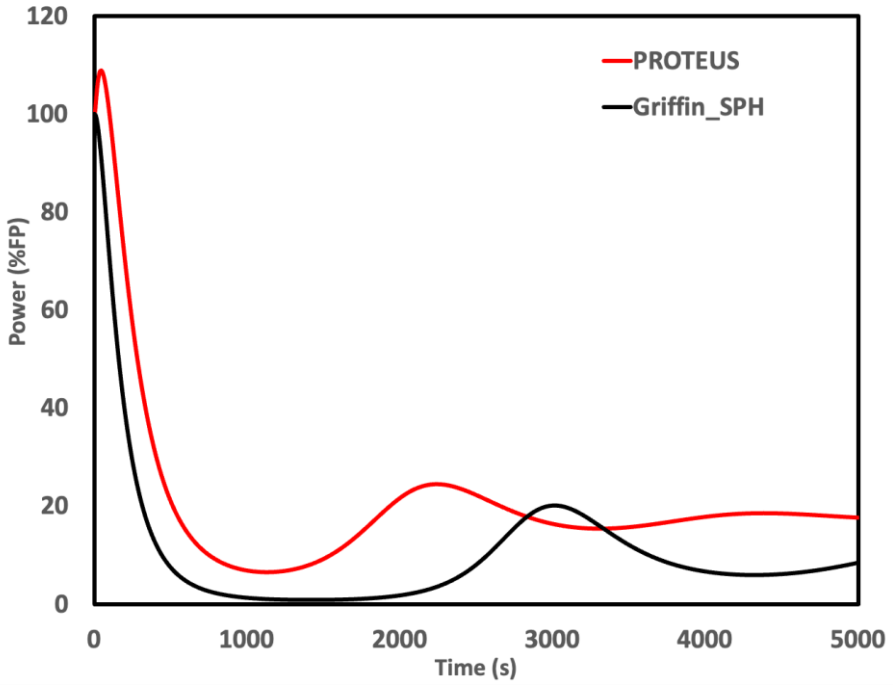


Figure 6.15. Power evolutions for the coupled calculations during the load following power transient.

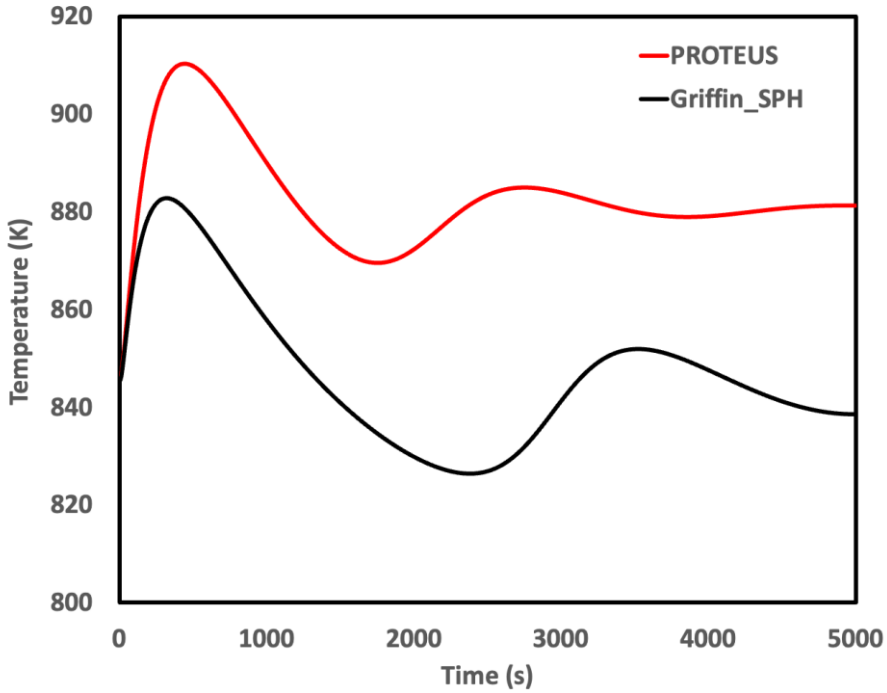


Figure 6.16. Average fuel pin temperature evolutions for the coupled calculations of the load following power transient.

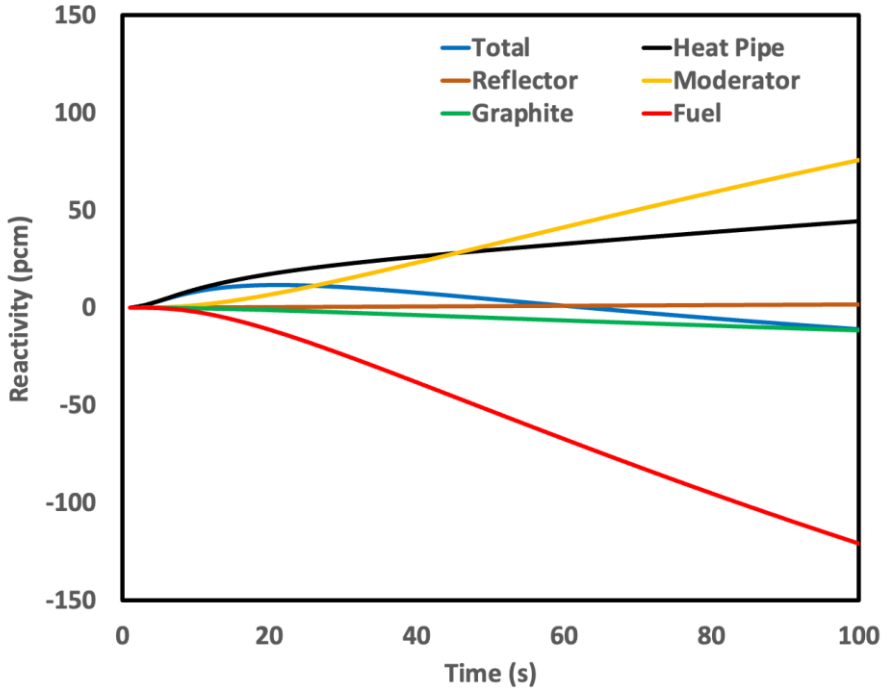


Figure 6.17. Component-wise reactivity evolutions of the coupled PROTEUS and SAM calculation during the load following power transient.

For a more consistent comparison with the coupled Griffin/BISON/Sockeye calculation, a coupled PROTEUS and SAM calculation was repeated without the thermal feedback of the heat pipe. In this calculation, the temperature profile of the heat pipe from the steady state result is utilized in PROTEUS to evaluate temperature-dependent cross sections at the heat pipe region. Figures 6.18 and 6.19 show the power and fuel temperature evolutions from the coupled PROTEUS and SAM calculation without thermal feedback of the heat pipe. In the first 1000 s, the power decreases due to the overall negative feedback, as shown in Fig. 6.20. Without the positive feedback of the heat pipe, the negative feedback from the fuel Doppler effect is larger than the positive feedback from the moderator and thus the overall feedback is negative at the beginning of the transient. The PROTEUS results agree with the Griffin results in the first 1000 s. After 1000 s, the results from PROTEUS and Griffin start to differ. But both of the results show oscillation behaviors. In the PROTEUS result, the total reactivity becomes positive after 1000 s, which leads to an increase in power. The increasing power makes the fuel average temperature increase after 1600 s, as shown in Fig. 6.19. The increased fuel temperature introduces negative feedback and the power decreases again after around 2000 s. The Griffin results show a slower transient compared to the PROTEUS results. The power increases after 1500 s and starts to drop again after about 3000s. The reasons are the different feedback models and solvers utilized in the two calculations. The Griffin uses the diffusion solver with the SPH factor, while PROTEUS uses the transport solver.

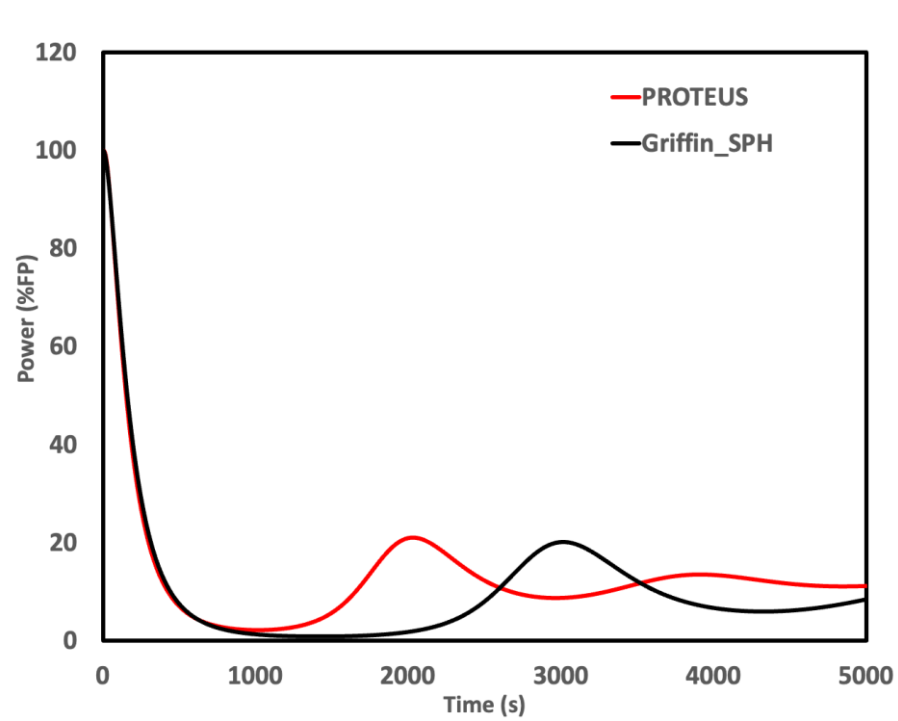


Figure 6.18. Power evolutions for the coupled calculations without heat pipe feedback during the load following power transient.

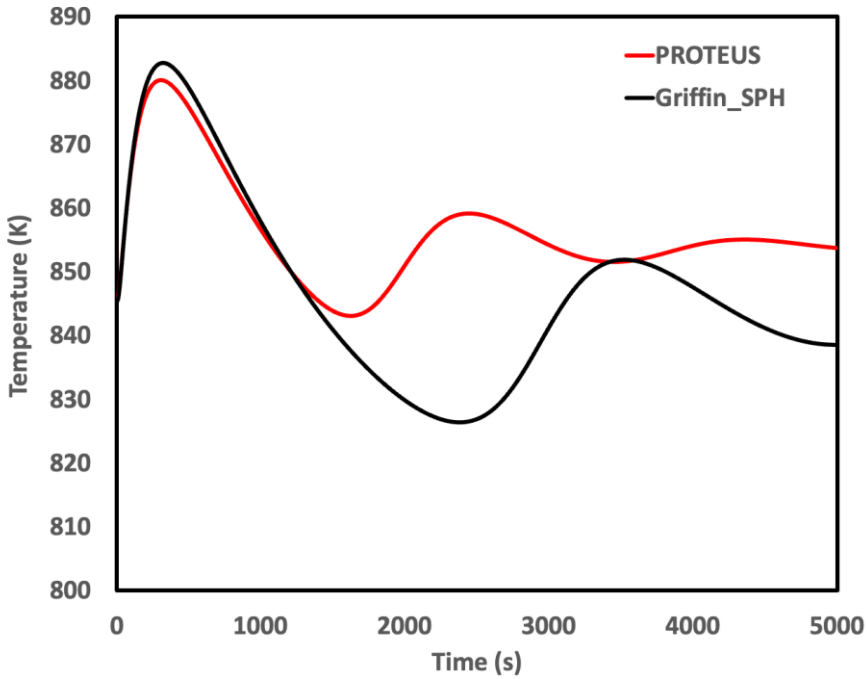


Figure 6.19. Average fuel pin temperature evolutions for the coupled calculations without heat pipe feedback during the load following power transient.

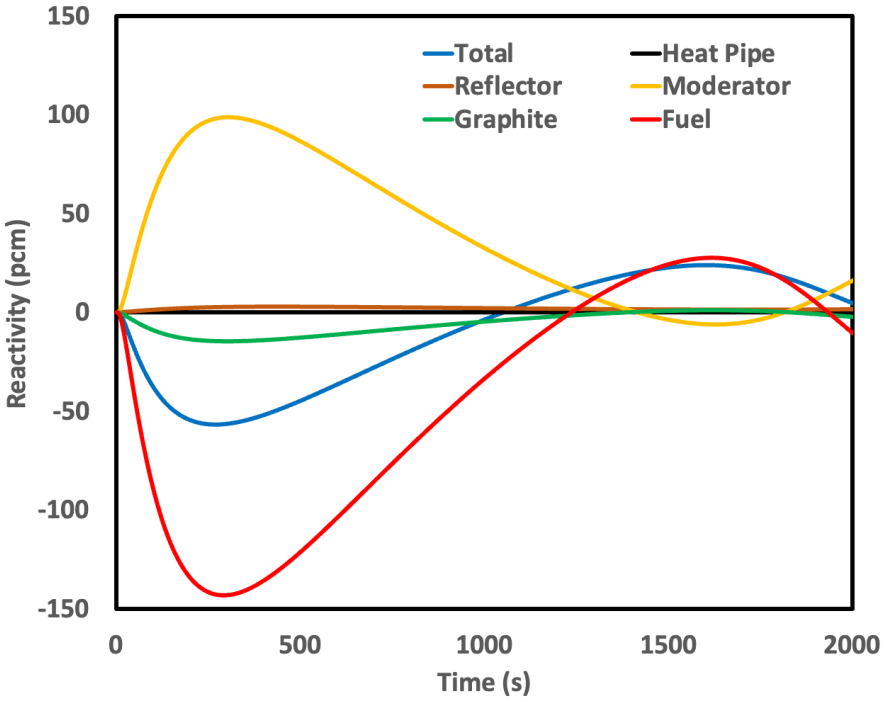
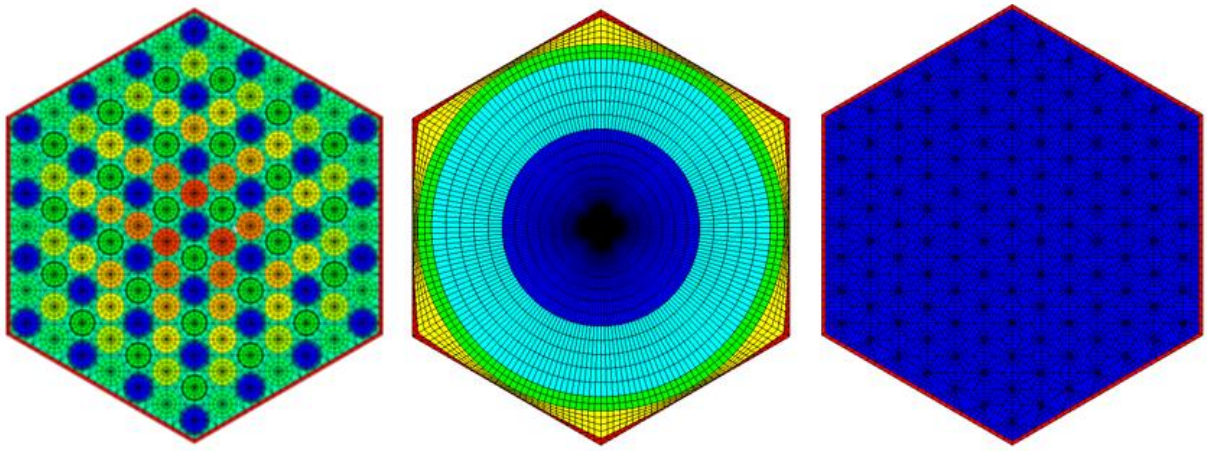


Figure 6.20. Component-wise reactivity evolutions of the coupled PROTEUS and SAM calculation without heat pipe feedback during the load following power transient.

6.2.3 Analysis of the One-sixth Core Problem of HP-MR

To reduce the computational cost, one sixth core model was developed for the HP-MR problem. In the PROTEUS-MOC calculations, the region-dependent multigroup cross sections were generated utilizing Serpent with ENDF/B-VII.0 cross section libraries in an 11-group structure. The multigroup cross sections were modeled as a function of temperature and they were generated based on the isothermal Serpent model with temperatures of all the materials varying among 600 K, 900 K, and 1200 K, respectively. The reactivity feedback effect was limited to the temperature feedback of fuel, moderator, graphite, reflector, and control drum in this calculation. The PROTEUS-MOC mesh was generated with the Argonne mesh toolkits [93]. First separate meshes for the fuel assembly, control drum, and reflector were developed, as shown in Fig. 6.21.

Then these meshes were merged, and the resulting mesh is presented in Fig. 6.22. The beryllium reflector was modeled as one ring of hexagonal assemblies in the HP-MR in [53] for simplification while the circular geometry of the reactor is modeled in this work. Ninety-six directions for the angular discretization and an anisotropic scattering order P_3 were utilized in PROTEUS-MOC.



(a) (b) (c)

Figure 6.21. The fuel (a), control drum (b), and reflector (c) mesh generated by mesh toolkit.

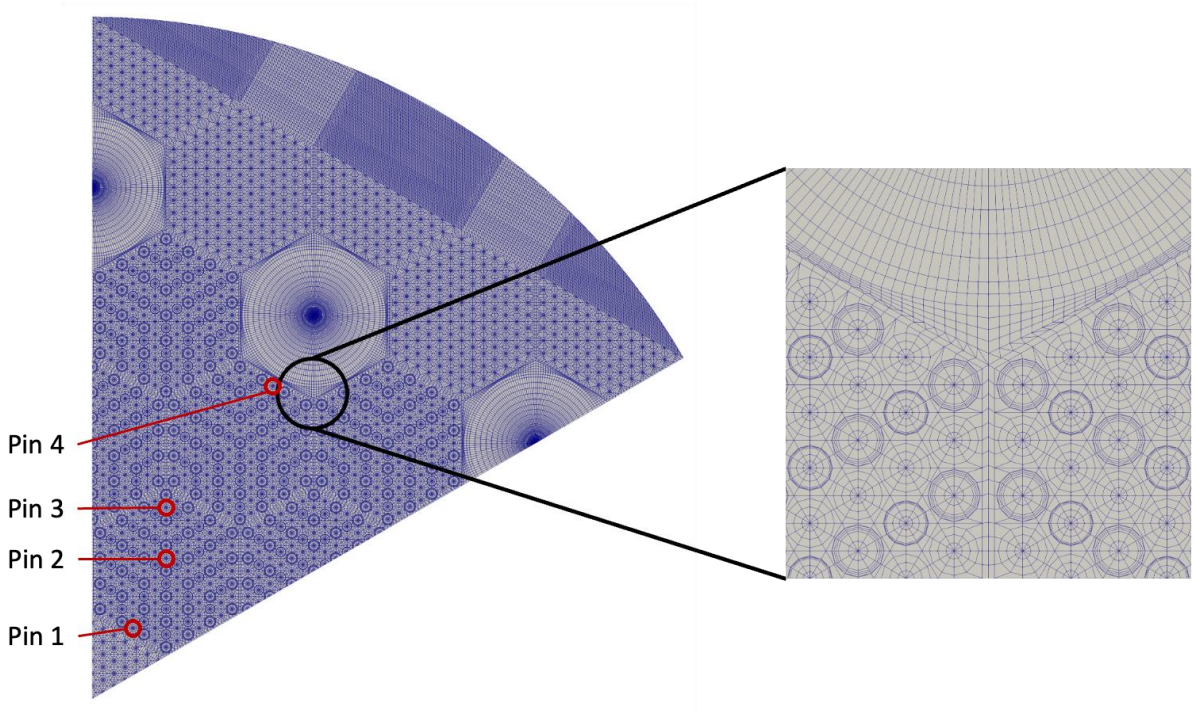


Figure 6.22. Generated mesh for 1/6 of the HP-MR problem in PROTEUS-MOC.

The mesh for 3D heat conduction calculation in SAM was modified from the mesh for BISON calculation in the one-sixth HP-MR model of the Virtual Test Bed (VTB) [94]. Figure 6.23 presents the meshes utilized in the 3D heat conduction calculation of SAM. In the reactor radial outer boundary, top and bottom surfaces of the reactor, the convective boundary condition was applied with the external ambient temperature of 800 K and a heat transfer coefficient of 100 W/m^2K. The 2D-RZ mesh was developed for the heat pipe calculations of SAM with the built-in functions in SAM. There are total 192 second-level SAM sub-applications for the separate simulation of the heat pipes. The convective heat transfer boundary condition was applied in heat pipe modeling at the condenser surface. The external ambient temperature was set to 800 K and the heat transfer coefficient was set to 10^6 W/m^2K at the steady state calculation.

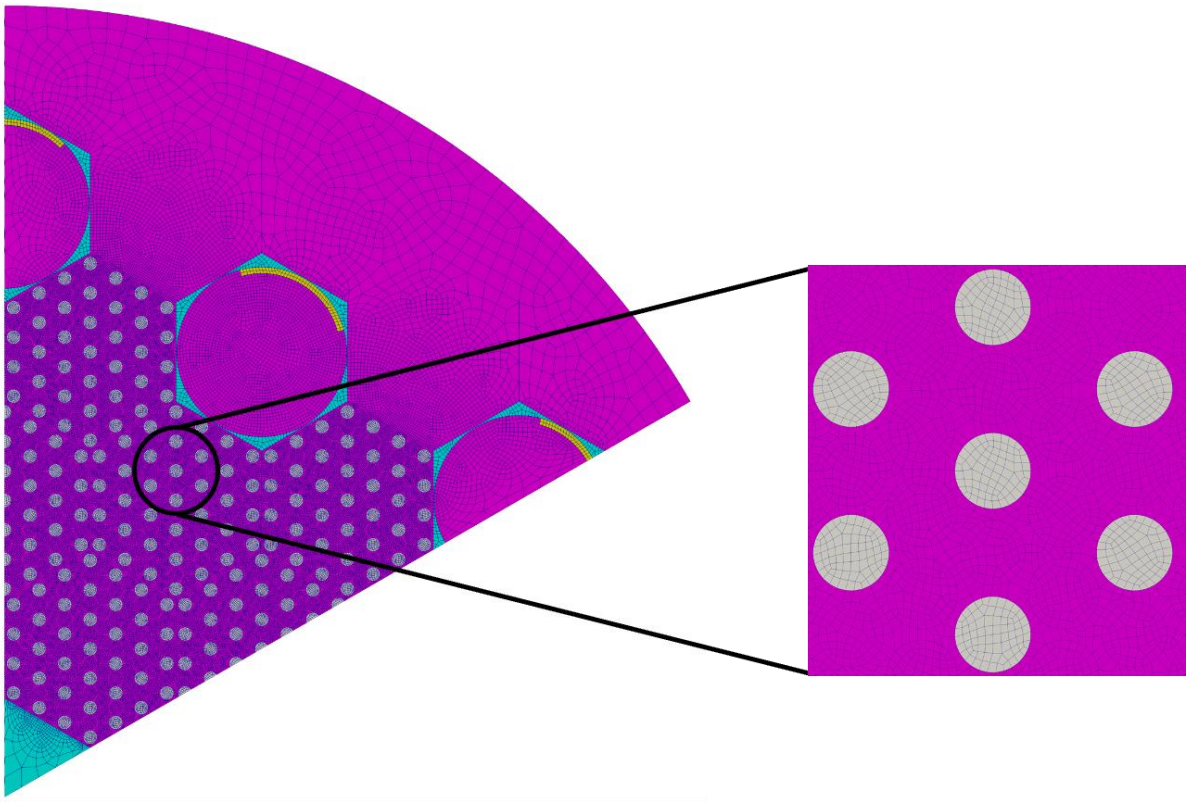


Figure 6.23. Generated mesh for 1/6 of the HP-MR problem in SAM.

First, the steady state calculations were performed for the HP-MR problem. To verify the PROTEUS-MOC model for the HP-MR problem, the isothermal calculation results from PROTEUS-MOC and Serpent are compared. Table 6.6 shows the multiplication factors from PROTEUS-MOC isothermal calculations and those from Serpent results. The effective multiplication factor of PROTEUS-MOC transport solutions for each temperature agrees well with the Serpent result. The maximum difference between PROTEUS-MOC transport calculations and Serpent results is 65 pcm at 600 K. The axial power distributions of four fuel pins at 900 K are compared in Fig. 6.24. The positions of these four pins are given in Fig. 6.22. From the Serpent results, pin 4 has the maximum pin power in the core. The power distributions of PROTEUS-MOC transport calculation generally match the Serpent solutions within 3σ uncertainties. The maximum relative difference of the power density between PROTEUS-MOC and Serpent results is 5.29%, located at the top of pin 2. The root mean square relative error (RMSRE) of the power density between PROTEUS-MOC and Serpent results in these four pins is 1.99%. The radial power distributions from PROTEUS isothermal calculations at 900 K at axial heights 0.25 m and 1.00 m are present in Fig. 6.25 and Fig. 6.26, respectively.

Table 6.6. Comparison of eigenvalues from Serpent and PROTEUS-MOC for HP-MR problem.

Temperature(K)	Serpent k-eff	PROTEUS-MOC	
		k-eff	Diff. (pcm)
600	1.09340 ± 0.00015	1.09405	65
900	1.08774 ± 0.00015	1.08834	60
1200	1.08120 ± 0.00015	1.08168	48

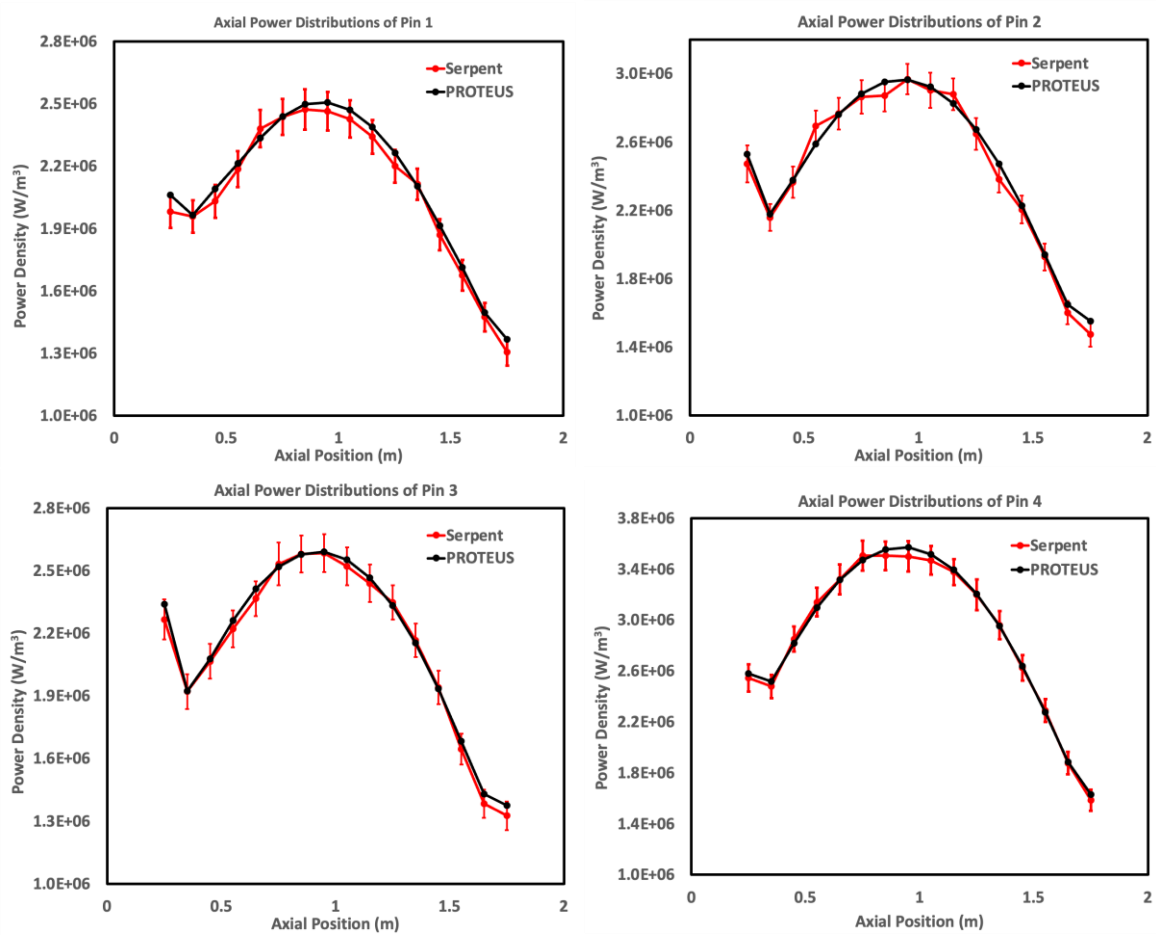


Figure 6.24. Axial distributions of power in different pins at 900 K.

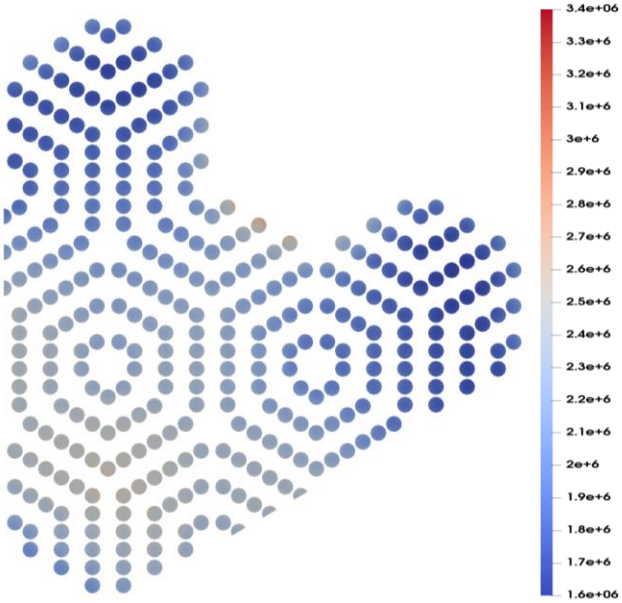


Figure 6.25. Radial distributions of power density (W/m^3) from PROTEUS isothermal calculation in the plane at 0.25 m.

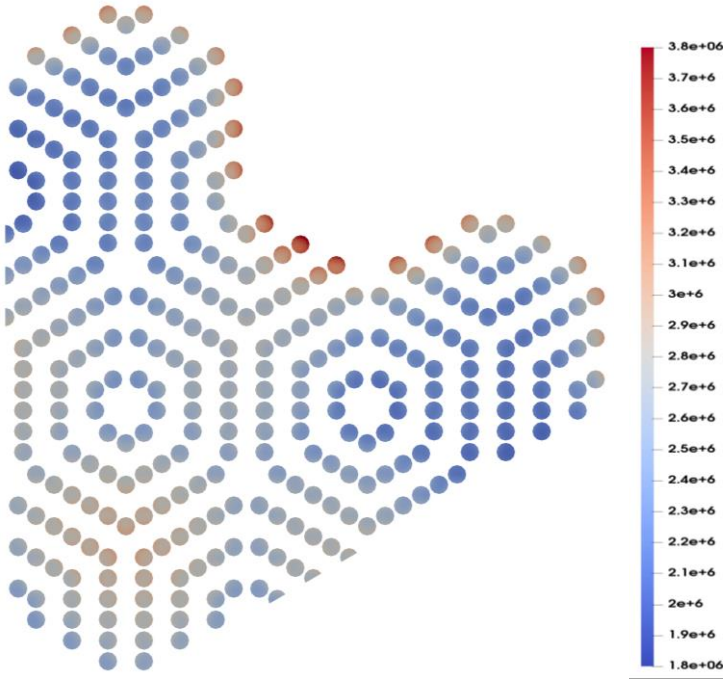


Figure 6.26. Radial distributions of power density (W/m^3) from coupled PROTEUS isothermal calculation in the plane at 1.00 m.

The effective multiplication factor from the coupled PROTEUS-MOC and SAM steady state calculation is 1.08920. Figures 6.27 and 6.28 show the converged temperature distributions in the reactor core. The maximum temperature from the coupled PROTEUS-MOC and SAM calculation is 853.9 K. Figure 6.29 presents the axial power distributions of four pins from the coupled calculations. The power distributions from the coupled calculation match with those from the PROTEUS-MOC isothermal calculations at 900 K. This shows that the thermal feedback at steady state has relatively small impact on the power shape.

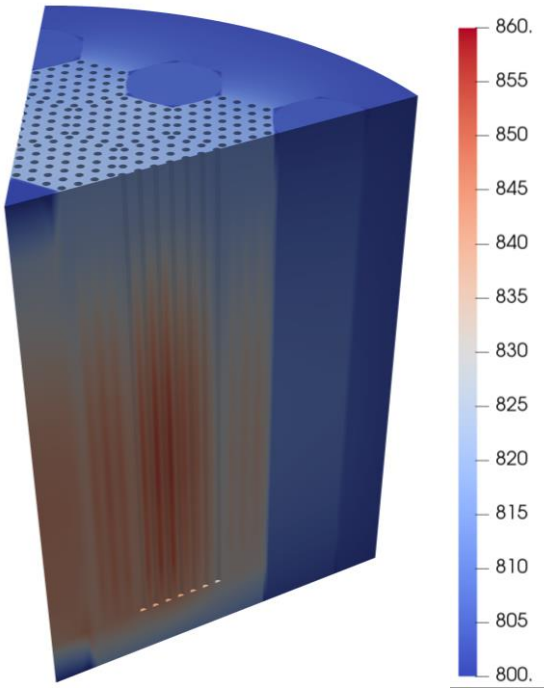


Figure 6.27. Temperature distribution from coupled calculations.

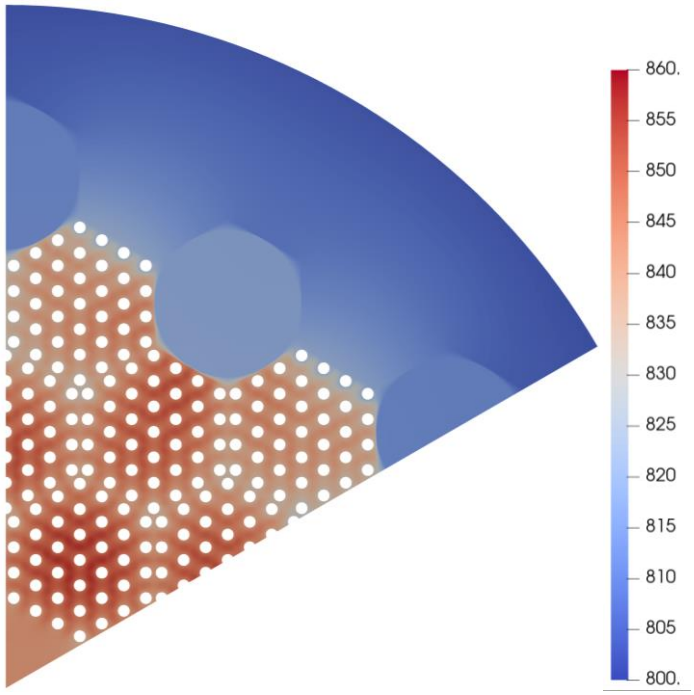


Figure 6.28. Temperature distribution at the middle plane from coupled calculations.

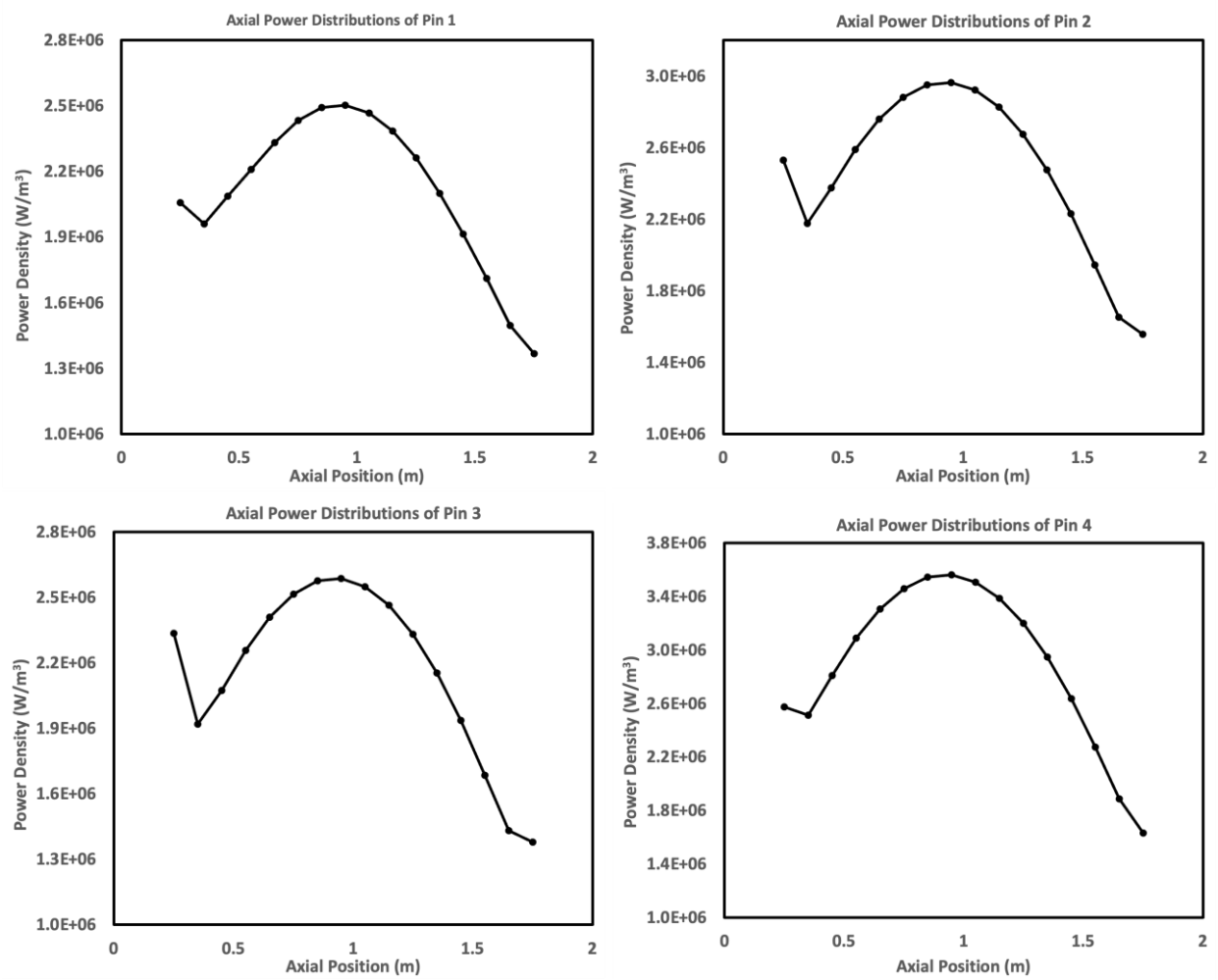


Figure 6.29. Axial distributions of power in different pins from coupled calculations.

The coupled calculation was performed for the load following power transient of the one-sixth HP-MR core problem with PROTEUS-MOC transport solver and SAM. First the coupled transient calculation was restarted from the coupled steady state calculation. At the beginning of the transient, the convective heat transfer coefficient at the condenser walls of the heat pipe was reduced from 10^6 W/m^{2}K to 10^2 W/m^{2}K. Figures 6.30, 6.31, and 6.32 give the calculation results of the coupled simulation for this transient. Figure 6.30 shows the power and fuel temperature evolutions from the coupled calculation. Because the convective heat transfer coefficient is significantly reduced at the heat pipe condenser wall, the core temperature increases at the

beginning of the transient, as shown in Fig. 6.30 and Fig. 6.32. The core fuel average temperature reaches a maximum value of 863.5 K at 344 s and the maximum fuel temperature increases to 880.5 K at 301 s. The increased temperature leads to a power decrease due to the negative fuel Doppler feedback. The power reaches a minimum value of 8.2% of the steady state power at 1062 s. The decreased power leads to the fuel temperature drops after it reaches the maximum value, which in turn causes the power increases after 1062 s due to the negative feedback.

The coupled calculations of the one-sixth HP-MR core problem were performed on the HPC Cluster of the University of Michigan. 240 CPUs were utilized in the coupled PROTEUS-MOC and SAM calculations. The coupled steady state calculations toke 1300 CPU-hours and the coupled transient calculation took 72228 CPU-hours, which was about 300 hours of computational time with 240 CPUs.

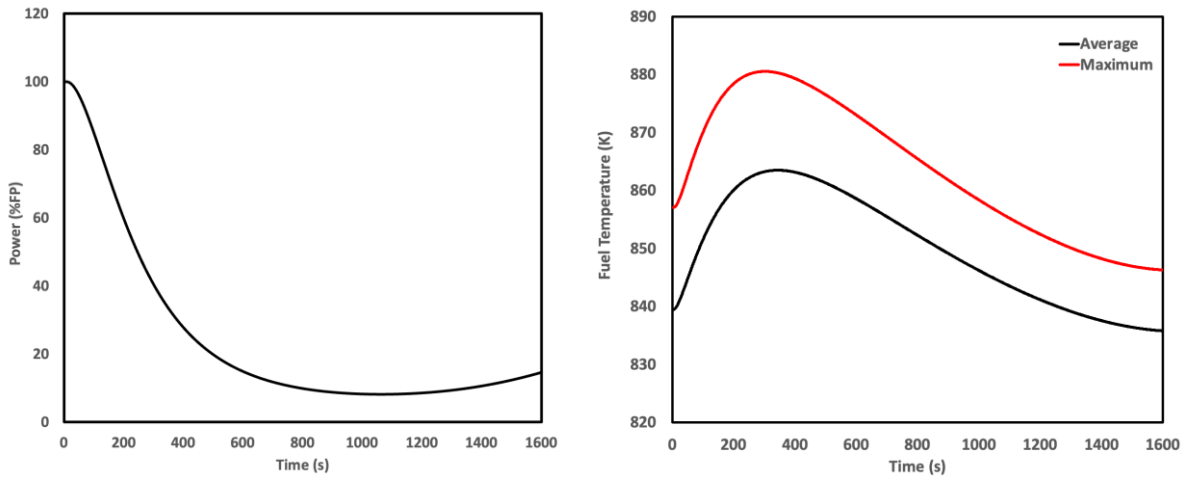


Figure 6.30. Power (left) and fuel temperature (right) evolutions for the coupled calculations of the load following power transient.

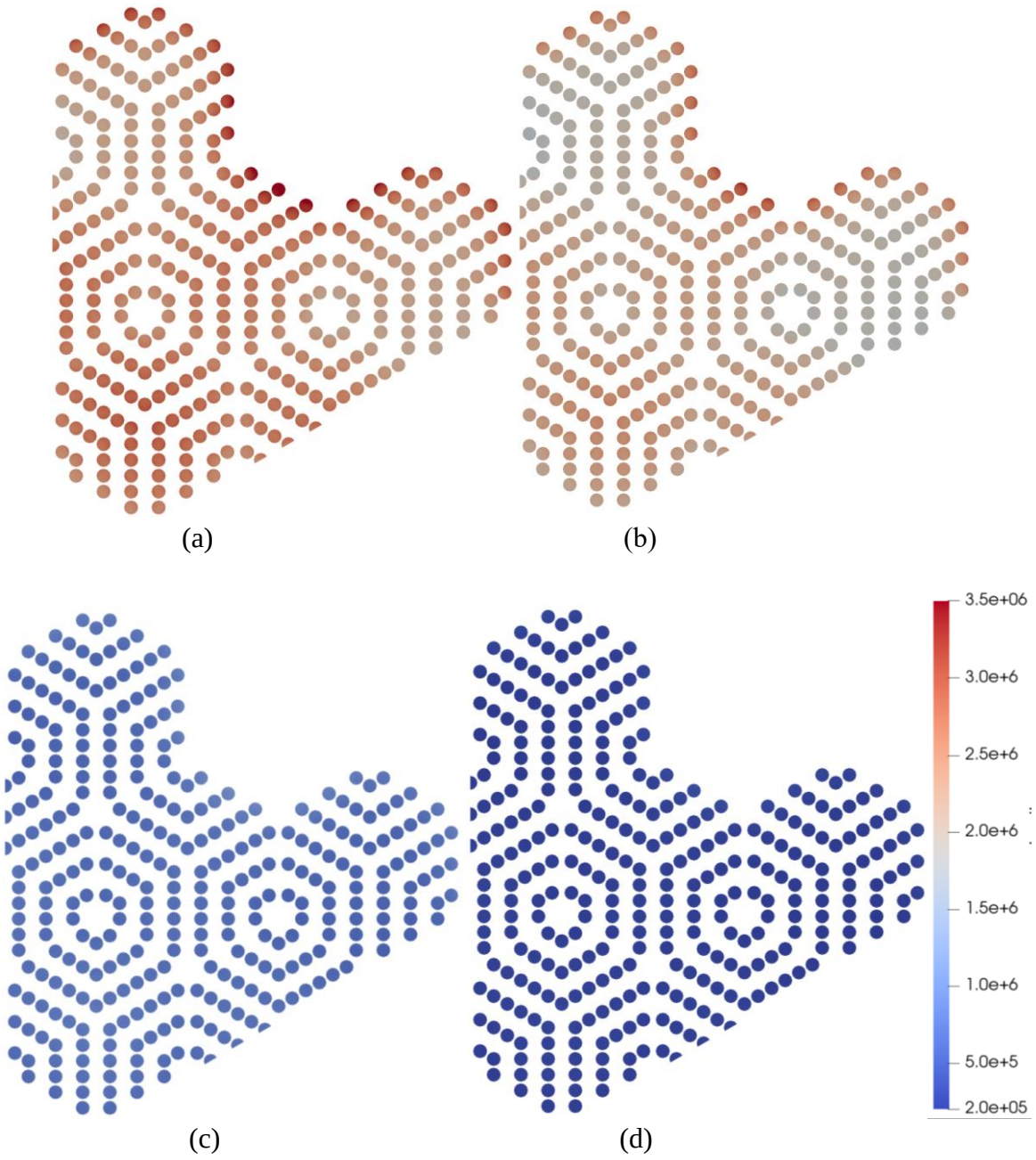


Figure 6.31. Power distributions of the middle plane at 0 s (a), 100 s (b), 400 s (c), and 800 s (d) for the coupled calculations of the load following power transient.

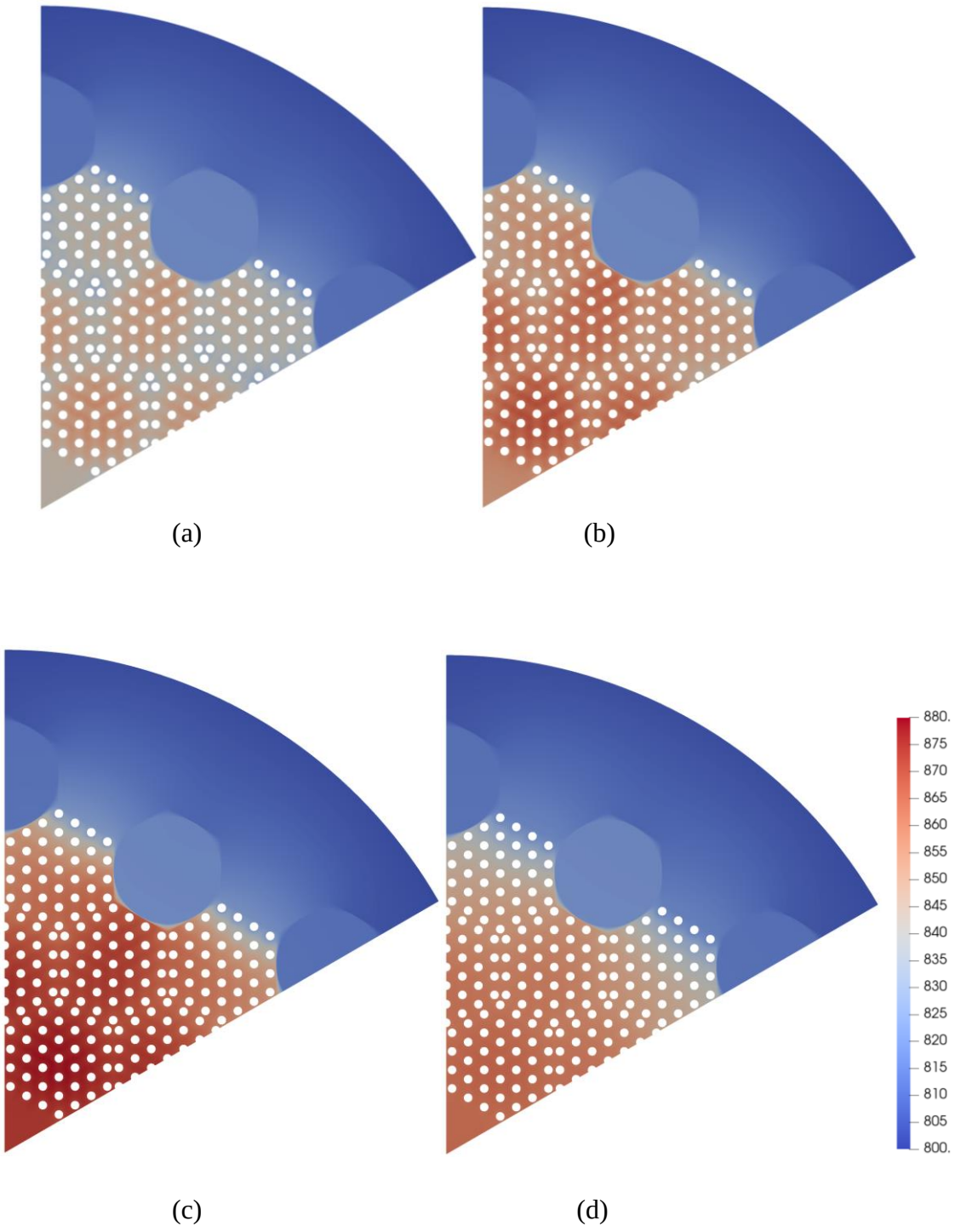


Figure 6.32. Temperature distributions of the middle plane at 0 s (a), 100 s (b), 400 s (c), and 800 s (d) for the coupled calculations of the load following power transient.

6.3 Summary

The coupled PROTEUS-MOC and SAM code system for micro-reactor applications was discussed in this chapter. A MOOSE wrapper of PROTEUS-MOC was developed for coupling with SAM under the MOOSE framework. In the coupled PROTEUS-MOC and SAM calculation, the PROTEUS wrapper serves as the master application to control the simulation process and 3D heat conduction of SAM is the first level sub-application. Inside the SAM calculation, each heat pipe in the core is modeled separately as the second level sub-applications in SAM.

To demonstrate the capabilities of the coupled PROTEUS-MOC and SAM for micro-reactor simulation, a unit-cell and one-sixth core problems of HP-MR were analyzed with the coupled code system. In the unit-cell problem, the eigenvalues from PROTEUS-MOC isothermal calculations matched with the Serpent results. The axial power shapes from PROTEUS-MOC were in good agreement with Serpent and Griffin calculations. Meanwhile, the computational time for PROTEUS-MOC was significantly reduced compared to Serpent and Griffin transport calculations. The load following power transient for the unit-cell problem was analyzed with the coupled PROTEUS-MOC and SAM code system. The results were compared with the solutions from coupled calculations based on the Griffin diffusion solver with SPH factors. The power evolution from the coupled PROTEUS-MOC and SAM calculation shows a different trend compared to the coupled Griffin calculation at the first 50 s, due to the feedback of the heat pipe is not considered in the Griffin calculation. To have a consistent comparison with the coupled Griffin calculation, a coupled PROTEUS and SAM calculation is performed for the same unit-cell problem without the thermal feedback of the heat pipe. The power evolution from the coupled PROTEUS-MOC and SAM calculation without thermal feedback of heat pipe shows better agreement with that of the coupled Griffin calculation.

In addition, the steady state and transient analyses were performed for the one-sixth core problem of HP-MR. The eigenvalues from PROTEUS-MOC isothermal calculations matched with the Serpent results. The load following power transient of the one-sixth core problem demonstrated the applicability of the coupled PROTEUS-MOC and SAM for simulations of the transients in micro-reactors. Compared to the existing codes, the developed coupled PROTEUS and SAM code system can be utilized for the transport-based multiphysics analysis of the micro-reactors with heterogeneous geometries. The MOC transport solver of PROTEUS is accelerated with the uCMFD and quasi-static methods, which makes it practical to be applied to the steady state and transient multiphysics simulations of micro-reactor.

Chapter 7 Summary and Future Work

The objective of this work is to develop a fast-running and accurate multiphysics simulation tool for the design and analyses of MSRs and a transport based multiphysics tool with transient simulation capability for micro-reactors. The coupled neutronics and thermal-hydraulics multiphysics analysis capabilities for MSRs and micro-reactors were developed using the neutronics code PROTEUS and the system analysis code SAM. The nodal solver of PROTEUS, named PROTEUS-NODAL, has the capability to model the drift of delayed neutron precursors in MSR. For accurate and efficient simulation of the steady-state and transient behaviors of MSRs, PROTEUS-NODAL was coupled with both 1-D and Multi-D SAM solvers. For the MSR with parallel-channel flows in moderator blocks, 1-D SAM is utilized and the MSR with the flow in the cylindrical tank is modeled with Multi-D SAM. The coupled PROTEUS-NODAL and SAM code system was verified using the MSFR benchmark problem and validated with available experimental data of the MSRE benchmark problem.

Meanwhile, the various micro-reactor designs and irregular geometries, make the conventional analysis tools based on the diffusion theory inadequate to simulate the micro-reactors. The MOC transport solver of PROTEUS, PROTEUS-MOC, utilizes the unstructured finite element based MOC method and it can handle 3-D heterogeneous problems with complicated geometries. Thus PROTEUS-MOC is coupled with SAM for micro-reactor simulations. A unit-cell and one-sixth core problems of HP-MR were analyzed with the coupled code system to demonstrate its applicability for simulations of micro-reactors.

7.1 Summary

The theoretical foundations of the coupled multiphysics calculations of MSR and micro-reactor were presented in Chapter 2. The systems of the nonlinear equations for the coupled neutronics and thermal-hydraulics calculations of MSR with flowing fuel were provided first. The coupled multigroup neutron diffusion equations, delayed neutron precursor equations, and mass, momentum, and energy conservation equations for single-phase flow were solved in the coupled calculations of MSR. To consider the flowing fuel in MSR, the fuel drift term is added to the delayed neutron precursor equations. The coupled multigroup neutron transport equations, delayed neutron precursors equation, and heat conduction equation were solved in the micro-reactor. Then the operator-splitting, Picard iteration, and JFNK methods for solving the coupled system of nonlinear equations were discussed. In both operator-splitting and Picard iteration methods, individual physics is solved with the already developed and optimized code, and these codes are coupled with certain data passing interfaces. In the Picard iteration scheme, different physics are solved iteratively within a time step in transient until all the physics are converged. While in the operator-splitting scheme, each physics is solved sequentially and only once in each time step. Different from the operator-splitting and Picard iteration method, all the physics are solved simultaneously by forming a large nonlinear algebraic system in the JFNK method.

The developed coupling schemes of PROTEUS-NODAL and SAM for MSR applications were provided in Chapter 3. PROTEUS-NODAL was coupled with both 1-D and Multi-D SAM solvers. An application of MOOSE named TreeFrog was developed as the wrapper for PROTEUS-NODAL to communicate with other MOOSE applications. Another master MOOSE application called TreeKangaroo was also developed to control the coupling calculation of TreeFrog and 1-D SAM. The Picard iteration is utilized in coupled steady-state calculations, and the operator-

splitting method is used in coupled transient calculations. In the coupling of PROTEUS-NODAL and Multi-D SAM, Multi-D SAM is served as the master application which controls the execution of TreeFrog and 1-D SAM.

The verification tests of the coupled PROTEUS-NODAL and SAM code system using the MSFR benchmark problem were shown in Chapter 4. First a brief introduction of the MSFR problem was given. Then for the steady state verification tests, the coupled calculation results of PROTEUS-NODAL and Multi-D SAM as well as the results of coupled PROTEUS-NODAL and 1-D SAM were compared with those of PROTEUS-NODAL and the commercial CFD software ANSYS CFX. The power distributions from those three calculations agreed well with each other. The velocity and temperature fields matched well between the Multi-D SAM and CFX solutions. However, the axial velocity field of 1-D SAM was different from that of CFX due to the neglected lateral flow. For the transient verification tests, the UTOP, ULOF, and ULOHS transient scenarios were analyzed with the coupled code system. The results were compared with solutions obtained from the PARCS-TRACE calculation and the coupled calculation of a diffusion theory based neutronics code and a CFD code performed at TUDelft. In general, the power evolutions of the coupled calculation of PROTEUS-NODAL and SAM agreed well with those solutions.

The coupled PROTEUS-NODAL and SAM code system was validated with the available experimental data of the MSRE benchmark problem in Chapter 5. The R-θ-Z model of PROTEUS-NODAL and the multiple parallel channel model of 1-D SAM were developed for MSRE. The protected pump transients at zero power were analyzed with the coupled code system of PROTEUS-NODAL and SAM. The predicted reactivity losses due to delayed neutron precursor drift in the core agreed well with the measured values during the transients. In addition, the analysis

results of the natural circulation test suggested that the coupled PROTEUS-NODAL and SAM code system is able to represent the thermal feedback properly.

In Chapter 6, the coupling schemes of PROTEUS-MOC and SAM for micro-reactor applications were discussed. First the MOOSE wrapper of PROTEUS-MOC for coupling with SAM under the MOOSE framework was presented. In the coupled PROTEUS-MOC and SAM calculation, the PROTEUS wrapper serves as the master application to control the simulation process and 3D heat conduction of SAM is the first level sub-application. Inside the SAM calculation, each heat pipe in the core is modeled separately as the second level sub-applications under the 3D heat conduction calculation in SAM. To demonstrate the capabilities of the coupled PROTEUS-MOC and SAM for micro-reactor simulation, a unit-cell and one-sixth core problems of HP-MR were analyzed with the coupled code system.

7.2 Conclusion

This thesis presents the coupled neutronics and thermal-hydraulics multiphysics analysis capabilities for advanced reactors, focusing on MSRs and micro-reactors, using the neutronics code PROTEUS and the system analysis code SAM. The capabilities for MSR simulations can be applied to both MSRs with the parallel-channel flow in moderator blocks and the flow in a cylindrical tank. Due to the utilization of the nodal solver in PROTEUS and the reduced order modeling of flows in SAM, the coupled PROTEUS and SAM code can be utilized to perform the steady and transient multiphysics analysis of MSR with reduced computational cost compared to the high-fidelity simulations based on FVM or FEM. The verification and validation tests of the coupled PROTEUS and SAM code system for MSR applications with MSFR and MSRE problems show that the coupled code system can be applied to perform the design and safety analysis of MSR efficiently and accurately.

The developed coupled PROTEUS and SAM code system can be utilized for the analysis of the micro-reactors with heterogeneous geometries. The MOC transport solver of PROTEUS is accelerated with the uCMFD and quasi-static methods, which makes it practical to be applied to the steady state and transient multiphysics simulations of micro-reactor. A unit-cell and one-sixth core problems of HP-MR were analyzed with the coupled code system. The analysis results of the unit-cell problem show that PROTEUS-MOC results match with Serpent and Griffin transport solutions while the computational time of PROTEUS-MOC is significantly reduced compared to Serpent and Griffin transport calculations. The steady state and transient analyses of the one-sixth core problem of HP-MR demonstrated the applicability of the coupled PROTEUS and SAM for simulations of micro-reactors.

7.3 Future Work

To determine the optimum time step size in transient calculations such that the computational accuracy and efficiency are both satisfied, an adaptive time step selection scheme based on the control theory was developed in PROTEUS-NODAL recently [95]. The PROTEUS-NODAL test results showed that the solutions with an adaptive time step selection scheme could maintain accuracy while reducing the computational time. Thus, it is suggested to implement the adaptive time step selection scheme in the coupled PROTEUS and SAM code system. For slow varying transients, such as the natural circulation test of MSRE, it is expected that the computational time with adaptive time step selection reduces significantly compared to that with a fixed time step size during the transient.

Another future work is adding the materials transport capability in the coupled PROTEUS-NODAL and SAM calculation for MSRs. One of the design and licensing challenges for MSRs is source term evaluation in the primary loop because of its impacts on the safety and economy of

the reactor systems. In the framework of probabilistic risk assessment (PRA), it is necessary to determine the amounts and species of radionuclides in the primary system according to their physical and chemical properties. In MSRs, transport and deposition of radionuclides in the primary loop should be considered in addition to their production by fission, corrosion, and activation. On-line reprocessing of fuel salt is also envisioned in MSRs, so removal of radionuclides during operation also needs to be included. With the materials transport capability, the coupled code system can be used to predict complex species production, transport, deposition, and evolution behavior in the circulating molten salts, which will allow a better understanding of species distribution and therefore lead to an optimized design of materials management system in MSRs.

The third potential future work is to consider the operation limits including the capillary limit, entrainment limit, boiling limit, viscous limit, and sonic limit in the heat pipe modeling. In the current heat pipe modeling approach, the vapor is modeled as a solid material and these limits are not considered. Without considering the operation limits, the cascading heat pipe failure transient simulation results could deviate from the true solutions. One heat pipe failure at the beginning of the transient could cause the consequent failures of its adjacent heat pipes after reaching their operation limits. In this case, the operation limits of the heat pipe need to be modeled to obtain an accurate solution. One way is to implement the analytic relations [96] for these limits in the SAM heat pipe models. Another way is coupling to Sockeye [46] for heat pipe calculations. In the Sockeye, heat pipe can be modeled as a 1-D, two-phase, high-fidelity flow. These limits are implicitly included by the physics inherent in the flow model [97].

Bibliography

[1] J. Buongiorno, et al., “Nuclear energy in a carbon-constrained world: Big challenges and big opportunities,” IEEE Power Energy Mag., 17 (2), 69-77, 2019.

[2] J. Serp, et al., “The Molten Salt Reactor (MSR) in Generation IV: Overview and Perspectives,” Prog. Nucl. Energy, 77, 308-319, 2014.

[3] “PROTEUS: Simulation Toolset for High-Fidelity Reactor Physics Analysis,” Nuclear Engineering Division, Argonne National Laboratory, https://www.ne.anl.gov/codes/proteus/.

[4] R. Hu, L. Zou, G. Hu, “SAM User’s Guide,” ANL/NSE-19/18, Argonne National Laboratory, 2019.

[5] E. Bettis, et al., “The Aircraft Reactor Experiment Design and Construction”, Nucl. Sci. Eng., 2, 804-825, 1957.

[6] P. Haubenreich, J. Engel, “Experience with the molten-salt reactor experiment,” Nucl. Appl. Technol., 8 (2), 118–136, 1970.

[7] R. Robertson, et al., “Conceptual Design Study of a Single-Fluid Molten Salt Breeder Reactor,” ORNL-4541, Oak Ridge National Laboratory, 1971.

[8] M. Brovchenko, et al., “Optimization of the Pre-conceptual Design of the MSFR: Evaluation and Viability of Liquid Fuel Fast Reactor System,” EVOL Project, Deliverable D2.2, 2013.

[9] D. LeBlanc, C. Rodenburg, “Molten Salt Reactors and Thorium Energy: Integral Molten Salt Reactor,” pp. 541-556, 2017.

[10] K. Kramer, “TerraPower’s molten chloride fast reactor technology,” ETEC Nuclear Suppliers Workshop, 2018.

[11] C. Fiorina, et al., “Modelling and analysis of the MSFR transient behavior,” Ann. Nucl. Energy, 64, 485-498, 2014.

[12] COMSOL, 2011. COMSOL Multiphysics® 4.2a User’s Guide. COMSOL Inc.

[13] B. Boer, et al., “Validation of the DALTON-THERMIX code system with transient analyses of the HTR-10 and application to the PBMR,” Nuclear Technology, 170, 306–321, 2010.

[14] S. J. De Zwaan, B. Boer, D. Lathouwers, “Static design of a liquid-salt-cooled pebble bed reactor,” Ann. Nucl. Energy, 34, 83–92, 2007.

[15] NRC, “TRACE V5.0 User Manual,” U. S. Nuclear Regulatory Commission, 2007.

[16] T. Downar, Y. Xu, V. Seker, “PARCS v3.0, U.S. NRC Core Neutronics Simulator,” Theory Manual, University of Michigan, 2010.

[17] E. Pettersen, “Coupled multi-physics simulations of the Molten Salt Fast Reactor using coarse-mesh thermal-hydraulics and spatial neutronics,” M.S. Thesis, University Paris-Saclay & Paul Scherrer Institute, 2016.

[18] M. Aufiero, et al., “Development of an OpenFOAM model for the Molten Salt Fast Reactor transient analysis,” Chem. Eng. Sci., 111, 390–401, 2014.

[19] OpenFOAM Documentation. https://cfd.direct/openfoam/documentation, 2020.

[20] T. Hu, et al., “Coupled neutronics and thermal hydraulics simulation of molten salt reactors based on OpenMC/TANSY,” Ann. Nucl. Energy, 109, 260-276, 2017.

[21] C. Fiorina, et al., “On the development of multi-physics tools for nuclear reactor analysis based on OpenFOAM®: state of the art, lessons learned and perspective,” Nucl. Eng. Des., 397, 111604, 2022.

[22] C. Fiorina, et al., “Development and verification of the neutron diffusion solver for the GeN-Foam multi-physics platform,” Ann. Nucl. Energy, 96, 212–222, 2016

[23] E. Cervi, S. Lorenzi, A. Cammi, L. Luzzi, “Development of a multiphysics model for the study of fuel compressibility effects in the Molten Salt Fast Reactor,” Chem. Eng. Sci., 193, 379–393, 2019.

[24] A. Lindsay, et al., “Introduction to Moltres: An application for simulation of Molten Salt Reactors,” Ann. Nucl. Energy, 114, 530-540, 2018.

[25] D. Gaston, et al., “MOOSE: A Parallel Computational Framework for Coupled Systems of Nonlinear Equations,” Nucl. Eng. Des., 239, 1768-1778, 2020.

[26] S. M. Park, A. Rykhlevskii, K. Huff, “Safety Analysis of Molten Salt Fast Reactor Fuel Composition using Moltres,” Proc. of Global 2019, Seattle, USA, September 22-26, 2019.

[27] A. M. Graham, Z. Taylor, B. Collins, et al., “Multiphysics Coupling Methods for Molten Salt Reactor Modeling and Simulation in VERA,” Nucl. Sci. Eng., 00, 1-22, 2021.

[28] R. Salko, et al., “CTF Theory Manual,” The North Carolina State University, 2017.

[29] B. Collins, et al., “Stability and accuracy of 3D neutron transport simulations using the 2D/1D method in MPACT,” J. Comput. Phys., 326, 612, 2016.

[30] B. Kochunas, et al., “VERA Core Simulator Methodology for PWR Cycle Depletion,” Nucl. Sci. Eng., 185, 1, 217, 2017.

[31] W. L. Moe, “Key Regulatory Issues in Nuclear Micro-Reactor Transport and Siting”, INL/EXT-19-55257-Rev. 000, Idaho National Laboratory, 2019.

[32] R. Testoni, A. Bersano, S. Segantin, “Review of nuclear micro-reactors: Status, potentialities and challenges,” Prog. Nucl. Energy, 138, 103822, 2021.

[33] https://inl.gov/trending-topic/micro-reactors/

[34] J. Ku, “Introduction to Heat Pipes,” Thermal and Fluid Analysis Workshop, 2015.

[35] G. Hu, R. Hu, J. M. Kelly, J. Ortensi, “Multi-physics Simulations of the Heat Pipe Micro Reactor,” ANL-NSE-19/25, Argonne National Laboratory, 2019.

[36] P. R. McClure, et al., “Kilopower Project: The KRUSTY Fission Power Experiment and Potential Missions,” Nucl. Technol., 206 (sup1), S1-S12, 2020.

[37] P. R. MaClure, et al., “Design of Megawatt Power Level Heat Pipe Reactors,” LA-UR-15-28840, Los Alamos National Laboratory, 2015.

[38] J. W. Sterbentz, et al., “Special Purpose Nuclear Reactor (5 MW) for Reliable Power at Remote Sites Assessment Report,” INL/EXT-16-40741, Idaho National Laboratory, 2017.

[39] Westinghouse Electric Company, “Westinghouse EVinci™ Micro Reactor,” 2018.

[40] C. H. Lee, Y. S. Jung, H. K. Cho, “Micro Reactor Simulation Using the PROTEUS Suite in FY19,” ANL/NSE-19/33, Argonne National Laboratory, 2019.

[41] A. M. Lafleche, M. A. Smith and C. H. Lee, “PROTEUS-MOC: A 3D Deterministic Solver Incorporating 2D Method of Characteristics,” Proc. Mathematics and Computation (M&C2013), Sun Valley, Idaho, May 5-9, 2013.

[42] ANSYS Inc., “ANSYS FLUENT Theory Guide,” 2017.

[43] G. A. McLennan, “ANL/HTP: A Computer Code for the Simulation of Heat Pipe Operation,” ANL-83-108, Argonne National Laboratory, 1983.

[44] C. Matthews, et al., “Coupled Multiphysics Simulations of Heat Pipe Micro-reactors Using DireWolf,” Nucl. Technol., 207(7), 1142-1162, 2021.

[45] C. H. Lee, et al., “Griffin Software Development Plan,” ANL/NSE-21/23, INL/EXT-21-63185, Argonne National Laboratory, Idaho National Laboratory, 2021.

[46] R. A. Berry, et al., “Sockeye Heat Pipe Code Theory Development: Based on the 7-Equation, Two-Phase Flow Model of RELAP-7,” Int. Topl. Mtg. Advances in Thermal Hydraulics (ATH’20), EDF Lab Paris-Saclay, France, 2020.

[47] J. D. Hales, et al., “BISON Theory Manual,” INL/EXT-13-29930, 2016.

[48] P. Romano, et al., “OpenMC: A State-of-the-art Monte Carlo Code for Research and Development,” Ann. Nucl. Energy, 82, 90-97, 2015.

[49] C. D. Cantwell, et al., “Nektar++: An open-source spectral/hp element framework,” Comput. Phys. Commun., 192, 205-219, 2015.

[50] R. Cimrman, et al., “Multiscale finite element calculations in Python using SfePy,” Adv. Comput. Math, 45, 1897-1921, 2019.

[51] W. Xiao, et al., “High-fidelity multi-physics coupling study on advanced heat pipe reactor,” Comput. Phys. Commun., 270, 108152, 2022.

[52] G. Yang, M. Jaradat, H. Park, W. Yang, "Verification and Validation Tests of Coupled PROTEUS-NODAL and SAM Code System for Molten Salt Reactor Simulation," UM/NRDSL-20/02, University of Michigan, 2020.

[53] N. Stauff, et al., "Detailed analyses of a TRISO-fueled micro-reactor," ANL/NEAMS-21/3, Argonne National Laboratory, 2021.

[54] C. H. Lee, Y. S. Jung, and M. A. Smith, "FY17 Status Report on NEAMS Neutronics Activities," ANL/NE-17/28, Argonne National Laboratory, 2017.

[55] Y. S. Jung, M. A. Smith, and C. H. Lee, "PROTEUS-NODAL User Manual," ANL/NE-18/4 (Rev. 1), Argonne National Laboratory, 2018.

[56] M. K. Jaradat, et al., "Molten Salt Reactor Transient Analysis Capability of PROTEUS-NODAL," Proc. of Global 2019, Seattle, USA, September 22-26, 2019.

[57] M. K. Jaradat, H. Park, W. Yang, C. Lee, "Development and Validation of PROTEUS-NODAL Transient Analyses Capabilities for Molten Salt Reactors," Ann. Nucl. Energy, 160, 108402, 2021.

[58] A. Hsieh, Y. S. Jung, C. H. Lee, and W. S. Yang, "Implementation of Coarse Mesh Finite Difference Acceleration Scheme for Irregular Geometry," Proc. of ANS M&C 2021, 1850-1858, 2021.

[59] A. Hsieh, G. Zhang, W. S. Yang, "Consistent Transport Transient Solvers of the High-Fidelity Transport Code PROTEUS-MOC," Nucl. Sci. Eng., 194(7), 508-540, 2020.

[60] R. Hu, "Three-dimensional flow model development for thermal mixing and stratification modeling in reactor system transients analyses," Nucl. Eng. Des., 345, 209-215, 2019.

[61] G. Hu, R. Hu, and L. Zou, "Development of Heat Pipe Reactor Modeling in SAM," ANL-NSE-19/9, Argonne National Laboratory, 2019.

[62] C. T. Kelly, "Iterative Methods for Linear and Nonlinear Equations," Society for Industrial and Applied Mathematics, 1995.

[63] D. A. Knoll, D. E. Keyes, "Jacobian-free Newton-Krylov methods: A survey of approach and applications," J. Comput. Phys., 193(2), 357-397, 2004.

[64] J. Wang, Q. Wang, M. Ding, "Review on neutronic/thermal-hydraulic coupling simulation methods for nuclear reactor analysis," Ann. Nucl. Energy, 137, 107-165, 2020.

[65] V. S. Mahadevan, "High resolution numerical methods for coupled non-linear multi-physics simulations with applications in reactor analysis," Ph.D. thesis, Texas A&M University, 2010.

[66] A. R. Toth, "A Theoretical Analysis of Anderson Acceleration and Its Application in Multiphysics Simulation for Light-Water Reactors," Ph.D. thesis, North Carolina State University, 2016.

[67] D. A. Knoll, H. Park, K. Smith, "Application of the Jacobian-free Newton-Krylov method to nonlinear acceleration of transport source iteration in slab geometry," Nucl. Sci. Eng., 167(2), 122-132, 2011.

[68] Y. Saad, “Iterative methods for sparse linear systems,” Society for Industrial and Applied Mathematics, 2003.

[69] R. Hu, “SAM Theory Manual,” ANL/NE-17/4 Rev. 1, Argonne National Laboratory, 2021.

[70] R. Martineau, D. Andrs, R. Carlsen, et al., “Multiphysics for nuclear energy applications using a cohesive computational framework,” Nucl. Eng. Des., 367, 110751, 2020.

[71] ANSYS Inc., “ANSYS CFX-Solver Theory,” 2017.

[72] V. Ignatiev, et al., “Progress in Development of MOSART Concept with Th Support,” Proc. of ICAPP 2012, Chicago, June 24-28, 2012.

[73] C. H. Lee, W. S. Yang, “MC^2-3 Multigroup Cross Section Generation Code for Fast Reactor Analysis,” Nucl. Sci. Eng. 187 (3), 268–290, 2017.

[74] M. Chadwick, et al., “ENDF/B-VII.0: next generation evaluated nuclear data library for nuclear science and technology,” Nucl. Data Sheets 107, 2931–3060, 2006.

[75] V. Ariu, “Heat Exchanger Analysis for Innovative Molten Salt Fast Reactor”, M.S. Thesis, ETH Zürich & Paul Scherrer Institute, 2014.

[76] R. H. Guymon, “MSRE Systems and Components Performance,” ORNL-TM-3039, Oak Ridge National Laboratory, 1973.

[77] B. Prince, et al., “Zero-Power Physics Experiments on the Molten-Salt Reactor Experiment,” ORNL-4233, Oak Ridge National Laboratory, 1968.

[78] R. Kedl, “Fluid Dynamic Studies of The Molten-Salt Reactor Experiment (MSRE) Core,” ORNL-TM-3229, Oak Ridge National Laboratory, 1970.

[79] M. Chadwick, et al., “ENDF/B-VII. 1: nuclear data for science and technology: cross sections, covariances, fission product yields and decay data,” Nucl. Data Sheets 112, 2887–2996, 2011.

[80] A. M. Leandro, F. Heidet, R. Hu, et al., “Thermal hydraulic model of the molten salt reactor experiment with the NEAMS system analysis module,” Ann. Nucl. Energy, 126, 59-67, 2019.

[81] F. P. Incropera, A. S. Lavine, T. L. Bergman, et al., “Fundamentals of heat and mass transfer,” Wiley, 2007.

[82] H. F. Poppendiek, L. D. Palmer, “Forced Convection Heat Transfer in Pipes with Volume Heat Sources within the Fluids,” ORNL-1395, Oak Ridge National Laboratory, 1952.

[83] B. Hanks, “Cubit Geometry and Mesh Generation Toolkit, Version 13.2,” Sandia National Laboratory, 2012.

[84] J. Engel and P. Haubenreich, “Temperatures in the MSRE Core During Steady-State Power Operation,” ORNL-TM-378, Oak Ridge National Laboratory, 1962.

[85] D. de Wet, M. S. Greenwood, “Status Report on the MSRE TRANSFORM Model for Thermal-Hydraulic Benchmarking,” ORNL-TM-2019/1359, Oak Ridge National Laboratory, 2019.

[86] T. Fei, T. Hua, B. Feng, F. Heidet, R. Hu, "MSRE Transient Benchmarks using SAM," Proc. of PHYSOR 2020, Cambridge, United Kingdom, March 29-April 2, 2020.

[87] M. Rosenthal et al., "Molten-salt reactor program semiannual progress report for period ending February 28, 1969," ORNL-4396, Oak Ridge National Laboratory, 1969.

[88] M. Delpech, et al., "Benchmark of dynamic simulation tools for molten salt reactors," Proc. of International Conference GLOBAL 2003, New Orleans, LA, USA, 2003.

[89] E. R. Shemon, C. W. Attaway, "User manual for EXODUS II mesh converter," ANL/NE-14/7, Argonne National Laboratory, 2014.

[90] J. Leppänen, et al., "The Serpent Monte Carlo Code: Status, Development and Applications in 2013," Ann. Nucl. Energy, 82, 142–150, 2015.

[91] C. H. Lee and Y. S. Jung, "Generation of the Cross Section Library for PROTEUS," ANL/NE-18/2, Argonne National Laboratory, 2018.

[92] C. H. Lee and Y. S. Jung, M. A. Smith, "FY17 Status Report on NEAMS Neutronics Activities," ANL/NE-17/28, Argonne National Laboratory, 2017.

[93] M. A. Smith, and E. R. Shemon, "User Manual for the PROTEUS Mesh Tools," ANL/NE-15/17 (Rev 2.0), Argonne National Laboratory, 2016.

[94] Virtual Test Bed repository, https://mooseframework.inl.gov/virtual_test_bed/.

[95] M. K. Jaradat, "Development of Neutronics Analysis Capabilities for Application to Flowing Fuel Molten Salt Fast Reactors," Ph.D. Thesis, University of Michigan, 2021.

[96] A. Faghri, "Heat Pipe Science and Technology," Global Digital Press, 1995.

[97] J. E. Hansel, et al., "Sockeye: A One-Dimensional, Two-Phase, Compressible Flow Heat Pipe Application," Nucl. Tech., 207(7), 1096-1117.